

Exploring the ultrafast excited-state dynamics of  
transition metal complexes with *ab-initio* multiple  
spawning

Dissertation

zur Erlangung des akademischen Grades  
Doctor rerum naturalium (Dr. rer. nat.)

vorgelegt dem Rat der  
Chemisch-Geowissenschaftlichen Fakultät  
der Friedrich-Schiller-Universität Jena

von

M.Sc. Julia Preiß

geboren am 24.10.1989 in Heilbad Heiligenstadt

Gutachter:

1. Prof. Dr. Benjamin Dietzek, Friedrich-Schiller-Universität Jena, Jena, Deutschland
2. Prof. Dr. Basile F. E. Curchod, Durham University, Durham, Großbritannien

Tag der Verteidigung: 16. Januar 2019

---

## Acknowledgments

First, I want to thank Prof. Dr. Benjamin Dietzek for giving me the opportunity to work in his inspiring group and for fruitful discussions that helped me gain a scientific perspective for my thesis and to be aware of the bigger picture of my research.

In addition, my thanks go to Dr. Martin Presselt, who was always available for discussions about the big and smaller scientific question that occurred during my thesis. Furthermore, I want to thank him for sensitizing me to the role politics play in science.

Moreover, I want to express my gratitude to Prof. Todd Martínez of the Stanford University. He gave me the opportunity to use and interface his software packages, TeraChem and FMS90. Furthermore, he enriched my work by his inspiring thoughts and made it possible for me to stay at the Stanford University, where I could work in a motivating and helpful group all of whom also earn my thanks. Here, special thanks go to Stefan Seritan and David Sanchez for being my office mates and their kind help with all cluster related questions.

I want to thank Prof. Dr. Basile Curchod for many discussions about the AIMS method, other technical details of the calculation and other things and for his patience and accurateness during his explanations. I was very lucky that in him I had someone I could always ask the theoretical questions I had.

Furthermore, my deep gratitude goes to Torsten Sachse, my dear college, office mate and very good friend. Our many discussions that consider all different aspects of the PhD program (too many to name all of them here) helped me solve all kinds of problems along the way. Special thanks to him for giving me the opportunity to use his programs, which really simplified my workaday life and of course the user support for it. And, last but not least for reading this thesis, even though he already had a job somewhere else.

Additionally, I want to thank Karin Kobow, Felix Herrmann-Westendorf, Max Hupfer, Saunak Das and Martin Kaufmann for helping me with measurements, the analysis of the experiments and also the chemical and synthesis related questions.

---

All of this would not have been possible without the great support of my parents, family and friends, who were always assisting me during my school and university years and encouraging me to take the opportunities this thesis provided. I especially want to thank Patrick, who gave me emotional support during all the PhD time.

---

## Abstract

In the last century, quantum chemistry evolved to be widely applied, *e.g.* in physical chemistry. In contrast to the nowadays routine calculation of steady-state spectra, the simulation of ultrafast photochemical processes is very demanding and up to now mostly limited to small and medium-sized organic molecules. Fueled by the ever-growing computational power available, the simulation of big transition metal complexes with various applications now comes into reach. However, with a high number of atoms and electronic states of interest, transition metal complexes pose special challenges to the quantum-chemical methods used to model ultrafast excited-state dynamics.

The aim of this thesis is to identify methods that can meet the challenges of simulating the excited-state dynamics of transition metal complexes. In order to achieve this goal, a method for the description of the nuclear dynamics is selected first based on a comparison of two very promising methods. This comparison is done for one example organic molecule, which is used to demonstrate the difficulties of a classical treatment of the nuclei to describe nuclear quantum effects. The use of a semiclassical treatment, namely with the *ab-initio* multiple spawning (AIMS) method, can give an improved description of nuclear quantum effects. These nuclear quantum effects are expected to be of even higher importance for transition metal complexes, because of their high density of electronic states compared to organic molecules.

Secondly, a method for the description of the electronic structure is identified, which gives a good compromise between accuracy and computational cost. Generally, a good balance between accuracy and computational cost can be reached with time-dependent density functional theory (TDDFT). However, it is known that TDDFT has problems to describe charge-transfer states and doubly excited states. It was shown for the example metal complex ironpentacarbonyl, that charge-transfer states can be described when choosing an appropriate density functional. The limitations of TDDFT to describe states with double excitation character have been quantified by a comparison to the electronic structure method CASPT2. As such states can occur particularly at higher bond length stretches, these limitations have to be kept in mind when using TDDFT for dynamics

---

calculations. Particularly low computational costs can be achieved when an efficient implementation of TDDFT on graphics cards is used, which can yield a speed-up of several orders of magnitude compared to CPU-implementations. As part of this thesis, the aforementioned TDDFT implementation was interfaced with AIMS, which enabled the calculation of the excited-state dynamics of big transition metal complexes.

With the selected methods, 500 fs of the dynamics of a transition metal complex with more than 100 atoms have been simulated, which is the biggest AIMS calculations of a transition metal complex ever conducted. A comparison of the experimental results with the simulation validates the calculated results and gives further insights into the photo-deactivation mechanism of this complex. Furthermore, the excited-state dynamics of an experimentally fairly unexplored transition metal complex are predicted to illustrate the potential of the combination of methods used in this thesis. Summarizing, it was shown that the combination of AIMS and TDDFT in its GPU implementation can be used to model the excited-state dynamics of big transition metal complexes. TDDFT has to be applied carefully, because of its limitations to describe doubly excited states.

---

## Contents

Abstract.....	III
1 Introduction .....	1
2 Quantum mechanical description of nuclear dynamics – Example of an organic molecule .....	4
2.1 How to solve the time-dependent Schrödinger equation accurately .....	4
2.2 Ways to approximate the nuclear dynamics – Trajectory-based methods.....	8
2.2.1 Surface Hopping.....	8
2.2.2 Multiple Spawning .....	11
2.3 Results: Comparison of FSSH and AIMS for one example organic molecule.....	13
3 Quantum mechanical description of the electronic structure – Example $\text{Fe}(\text{CO})_5$ ....	18
3.1 Accuracy and computational cost of electronic structure methods.....	18
3.2 Results for the photodissociation of $\text{Fe}(\text{CO})_5$ .....	21
3.2.1 Steady-state UV-vis absorption spectra .....	23
3.2.2 Dynamics calculations with TDDFT/AIMS.....	24
3.2.3 Comparison of TDDFT and CASPT2.....	30
4 Photodynamics of transition metal complexes – Example Nickel porphyrinoids.....	34
4.1 NiTMP .....	34
4.1.1 Steady-state UV-vis absorption spectra .....	35
4.1.2 Analysis of the singlet excited states at the critical points.....	37
4.1.3 Dynamics calculation .....	41
4.1.4 Comparison to experiments .....	45
4.2 NiDEPE .....	48
4.2.1 Steady-state UV-vis absorption spectra .....	48
4.2.2 Dynamics calculation .....	49
5 Conclusion.....	53

---

6	Zusammenfassung .....	58
7	Appendix .....	63
7.1	The Hartree-Fock approach .....	63
7.2	Configuration Interaction and the importance of correlation.....	64
7.3	MCSCF, CASSCF and beyond .....	65
7.4	Density functional theory.....	67
7.4.1	Ground state density functional theory .....	67
7.4.2	Time-dependent density functional theory.....	69
7.5	Population changes in Fe(CO) <sub>5</sub> .....	72
7.6	Algorithm for the E <sub>rel</sub> -analysis for all time steps during the dynamics.....	73
7.7	Fit formulae for dynamics of NiTMP .....	73
7.8	XANES calculation.....	74
8	Bibliography .....	75
	List of Figures .....	83
	List of Tables .....	88
	List of Abbreviations .....	88
	General Abrevitations .....	88
	Formula symbols .....	90



## 1 Introduction

In the last century, quantum mechanics arose as a new field in physics, whose importance was highlighted *e.g.* by the Nobel Prize in physics awarded to Erwin Schrödinger and Paul Dirac in 1933. Their findings laid the foundation of modern computational chemistry, which is nowadays of importance for many fields of research and widely applied for example in life sciences, *e.g.* to examine the structure-activity relationship of drugs(1, 2), in magnetism, *e.g.* to compute properties like magnetic anisotropy(3, 4), or in thermodynamics, *e.g.* to compute properties like enthalpy and entropy(5, 6). Another important field of application for quantum mechanics is spectroscopy, with a great variety of different types of spectra that have been modeled successfully with quantum chemistry: vibrational and absorption spectra(7, 8), fluorescence spectra(9), photoelectron spectra(10), X-ray absorption spectra(11, 12) and electronic circular dichroism spectra(13, 14). These theoretical results can be compared to the measurements and help to interpret the experimental findings.

Over time, experimental techniques evolved from steady-state measurements to transient measurements with ever improving time resolution, which enabled the characterization of ultrafast photochemical processes.(15) This development led to an increased interest to also investigate the ultrafast photochemical processes with quantum mechanical methods. However, in contrast to the simulation of steady-state spectroscopy, where the treatment of a single conformation of the nuclei is often sufficient to model a molecular spectrum, the simulation of photochemical processes is much more demanding. An accurate description of the excited-state dynamics after photoexcitation requires the simultaneous description of the movement of both electrons and nuclei. However, a fully quantum mechanical calculation of all degrees of freedom can only be done for very small systems with fewer than ten atoms.(16) A few tens of nuclear degrees of freedom can be modeled with the multi-configurational time-dependent Hartree (MCTDH) method(17), which reduces the dimensionality of the calculation *via* the use of a time-dependent nuclear basis set. The description of bigger molecules can become feasible when applying trajectory-based methods.(18) However, they employ on-the-fly electronic structure calculations(19-23), which are usually the

limiting step. Probably the most applied method is the trajectory surface hopping, introduced by Tully(24, 25). Within this method, the nuclear wave function is modeled by a swarm of classical trajectories. This method was often used in combination with very expensive electronic structure methods (ESM) and therefore only applied to small to medium-sized organic molecules.(26-29) Fueled by the exponential growth of computational power available, a few exploratory studies of bigger transition metal complexes using the less computationally demanding time-dependent density functional theory (TDDFT) have been possible.(30, 31)

Investigations of transition metal complexes are of high importance as they have versatile applications, *e.g.* in photocatalysis(32), dye sensitized solar cells (DSSC)(33, 34), DNA intercalation(35) and cancer theranostics(36). The interaction of organic and inorganic chemistry enables an extreme variety of possible target structures of metal complexes to be synthesized.(37, 38) Hence, efficient methods for the routine prediction of the molecular properties of such complexes can help preselect the most promising compounds to be synthesized. In order to determine whether a complex is suitable for the aforementioned applications, its photophysical properties are among the first that have to be investigated. Therefore, the aim of this thesis is the quantum mechanical investigation of the ultrafast excited-state dynamics after photoexcitation of transition metal complexes. However, these complexes pose several challenges to quantum mechanical methods: (i) Complexes of interest for such applications are usually very big with more than 100 atoms and therefore a huge number of degrees of freedom needs to be accounted for in the simulation. (ii) They have a high number and energetic density of electronic states that need to be calculated, which can lead to a high number of nonadiabatic events that have to be modeled. In order to meet these challenges, it is necessary to find a compromise between accuracy and computational cost for the description of both the nuclei and the electrons, each of which are discussed in a separate chapter.

Chapter 2 is concerned with the selection of a method to describe the nuclear degrees of freedom. In order to be able to make a well-founded choice on the method, the chapter starts with a brief introduction into the quantum mechanical foundation of molecular dynamics. The following section 2.2 gives an overview of selected methods to

describe the nuclear dynamics. Based on that knowledge, section 2.3 contains a comparison of the calculations performed with the well-established surface hopping method and the efficient multiple spawning algorithm. This comparison shows the working principles using the example of one selected organic molecule, namely *N*-phenyldihydrotetraacanthracene. Instead of a transition metal complex, an organic molecule is chosen here as such a molecule constitutes a well-established starting point, because the methods have been mostly applied to organic molecules.<sup>(18, 26-29, 39-42)</sup> Furthermore, the molecule investigated has a rather simple electronic structure with only two excited states of interest. Thus, the focus lies on the selection of a method to calculate the nuclear degrees of freedom. In that section, the differences between organic molecules and transition metal complexes are pointed out and particular care will be taken to ensure that the selected method can also be applied to the more complex cases treated later in this thesis.

In chapter 3, the description of the electronic structure is considered. The chapter starts with a discussion about the accuracy and computational cost of different ESMs, which are explained in more detail in the appendix, sections 7.1 to 7.4. A metal complex with only eleven atoms but a complicated electronic structure with 20 electronic states of interest is discussed in section 3.2. This exemplifies the challenges that complicated electronic structures, which often occur in transition metal complexes<sup>(43)</sup>, pose to different ESMs and how to meet them.

The methods that have been identified as suitable for the description of transition metal complexes are applied to a big metal complex with more than 100 atoms in chapter 4. The thereby determined deactivation mechanism is compared to experimental results in order to validate the methods and further elucidate the mechanism. Subsequently, the dynamics of a experimentally fairly unexplored metal complex are predicted, highlighting the potential of the methods for routine application to metal complexes. In summary, the selected methods are validated and their capabilities to detail the ultrafast reaction mechanism of transition metal complexes are shown.

## 2 Quantum mechanical description of nuclear dynamics – Example of an organic molecule

The initial reaction steps of photochemical reactions happen on a femtosecond to picosecond time scale, which makes a coupled quantum mechanical description of nuclei and electrons necessary.<sup>(16, 39, 44)</sup> Therefore, in the following section, first the general interactions between nuclei and electrons as well as the mechanisms that facilitate population transfer between electronic states, are introduced together with the nomenclature that is used in the following. Based on this elementary knowledge of the underlying quantum mechanics, the approximations used in this thesis to describe the excited-state dynamics and their limitations are explained in section 2.2. A comparison of the methods to describe the nuclear dynamics is then conducted for one example organic molecule in section 2.3.

### 2.1 How to solve the time-dependent Schrödinger equation accurately

In general, the dynamic behavior of a molecule can be described quantum mechanically by the time-dependent Schrödinger equation (TDSE)<sup>(39, 45)</sup>.

$$i\hbar \frac{\partial \Psi(\mathbf{r}, \mathbf{R}, t)}{\partial t} = \hat{H} \Psi(\mathbf{r}, \mathbf{R}, t) \quad (2.1.1)$$

Here  $\Psi(\mathbf{r}, \mathbf{R}, t)$  is the time-dependent molecular wave function, which depends on the electronic coordinates  $\mathbf{r}$ , the nuclear coordinates  $\mathbf{R}$  and time.  $\hat{H}$  is the molecular Hamiltonian that describes the kinetic energy  $T$  of all particles involved and the interactions between them:<sup>(44)</sup>

$$\begin{aligned} \hat{H} = & \underbrace{-\sum_{\alpha}^N \frac{1}{2M_{\alpha}} \nabla_{\alpha}^2}_{\hat{T}_{nuc}} - \underbrace{\sum_i^n \frac{1}{2} \nabla_i^2}_{\hat{T}_{el}} - \underbrace{\sum_{\alpha}^N \sum_i^n \frac{Z_{\alpha}}{|\mathbf{r}_i - \mathbf{R}_{\alpha}|}}_{\hat{V}_{nuc-el}} + \underbrace{\sum_{\alpha < \beta}^N \frac{Z_{\alpha} Z_{\beta}}{|\mathbf{R}_{\alpha} - \mathbf{R}_{\beta}|}}_{\hat{V}_{nuc-nuc}} + \underbrace{\sum_{i < j}^n \frac{1}{|\mathbf{r}_i - \mathbf{r}_j|}}_{\hat{V}_{el-el}}. \quad (2.1.2) \\ & = \hat{T}_{nuc} + \hat{H}_{el} \end{aligned}$$

Here  $M_{\alpha}$  and  $Z_{\alpha}$  are the mass and the charge of the  $\alpha^{th}$  nucleus, respectively.  $\mathbf{R}_{\alpha}$  and  $\mathbf{r}_i$  are the coordinates of the  $\alpha^{th}$  nucleus and  $i^{th}$  electron, respectively.  $N$  and  $n$  are the number of nuclei and electrons, respectively. Here,  $\hat{H}_{el}$  is introduced as the electronic

Hamiltonian. Note that for this and all following expressions in this work atomic units(46) are used, hence setting  $\hbar = m_e = e = \frac{1}{4\pi\epsilon_0} = 1$ . Furthermore, bold formula symbols are used for vectors and matrices.

The molecular wave function can be described by the following exact ansatz, introduced by Born and Huang(47, 48):

$$\Psi(\mathbf{r}, \mathbf{R}, t) = \sum_i^{\infty} \chi_i(\mathbf{R}, t) \phi_i(\mathbf{r}; \mathbf{R}) \quad (2.1.3)$$

This ansatz expands the molecular wave function into a linear combination of nuclear wave functions  $\chi_i(\mathbf{R}, t)$  and electronic wave functions  $\phi_i(\mathbf{r}; \mathbf{R})$ . The  $\phi_i(\mathbf{r}; \mathbf{R})$  are a complete set of eigenfunctions of the electronic Hamiltonian  $\hat{H}_{el}$ , which depend parametrically on the nuclear coordinates. The corresponding eigenvalues are called  $\epsilon_i$  in the following and have a parametric dependence on  $\mathbf{R}$  as well.

In order to gain a more detailed picture of how the nuclei and electrons interact, we let the molecular Hamiltonian act on one of these expanded basis functions:

$$\begin{aligned} \hat{H} \chi_i(\mathbf{R}, t) \phi_i(\mathbf{r}; \mathbf{R}) &= \left( \hat{H}_{el} + \hat{T}_{nuc} \right) \chi_i(\mathbf{R}, t) \phi_i(\mathbf{r}; \mathbf{R}) \\ &= \left( \epsilon_i(\mathbf{R}) - \sum_{\alpha} \frac{1}{2M_{\alpha}} \nabla_{\alpha}^2 \right) \chi_i(\mathbf{R}, t) \phi_i(\mathbf{r}; \mathbf{R}) \\ &= \epsilon_i(\mathbf{R}) \chi_i(\mathbf{R}, t) \phi_i(\mathbf{r}; \mathbf{R}) - \phi_i(\mathbf{r}; \mathbf{R}) \left( \sum_{\alpha} \frac{1}{2M_{\alpha}} \nabla_{\alpha}^2 \chi_i(\mathbf{R}, t) \right) \\ &\quad - \sum_{\alpha} \frac{1}{M_{\alpha}} (\nabla_{\alpha} \phi_i(\mathbf{r}; \mathbf{R})) \cdot (\nabla_{\alpha} \chi_i(\mathbf{R}, t)) \\ &\quad - \chi_i(\mathbf{R}, t) \left( \sum_{\alpha} \frac{1}{2M_{\alpha}} \nabla_{\alpha}^2 \phi_i(\mathbf{r}; \mathbf{R}) \right) \end{aligned} \quad (2.1.4)$$

This can be inserted into the TDSE, multiplied by the complex conjugate of the electronic wave function  $\phi_j^*(\mathbf{r}; \mathbf{R})$  and integrated over the electronic coordinates  $\mathbf{r}$ :

$$\begin{aligned}
 i \sum_i \frac{\partial \chi_i(\mathbf{R}, t)}{\partial t} \langle \phi_j(\mathbf{r}; \mathbf{R}) | \phi_i(\mathbf{r}; \mathbf{R}) \rangle &= \sum_i \left[ \varepsilon_i(\mathbf{R}) \chi_i(\mathbf{R}, t) \langle \phi_j(\mathbf{r}; \mathbf{R}) | \phi_i(\mathbf{r}; \mathbf{R}) \rangle \right] \\
 &\quad - \sum_i \left[ \langle \phi_j(\mathbf{r}; \mathbf{R}) | \phi_i(\mathbf{r}; \mathbf{R}) \rangle \sum_\alpha \frac{1}{2M_\alpha} \nabla_\alpha^2 \chi_i(\mathbf{R}, t) \right] \\
 &\quad - \sum_i \left[ \sum_\alpha \frac{1}{M_\alpha} \langle \phi_j(\mathbf{r}; \mathbf{R}) | \nabla_\alpha \phi_i(\mathbf{r}; \mathbf{R}) \rangle \cdot \nabla_\alpha \chi_i(\mathbf{R}, t) \right] \\
 &\quad - \sum_i \left[ \chi_i(\mathbf{R}, t) \sum_\alpha \frac{1}{2M_\alpha} \langle \phi_j(\mathbf{r}; \mathbf{R}) | \nabla_\alpha^2 \phi_i(\mathbf{r}; \mathbf{R}) \rangle \right]
 \end{aligned} \tag{2.1.5}$$

The overlap of the electronic wave functions vanishes for different electronic states because of the orthogonality of the basis  $\phi(\mathbf{r}; \mathbf{R})$ . Therefore, equation (2.1.5) simplifies to:(39)

$$\begin{aligned}
 i \frac{\partial \chi_j(\mathbf{R}, t)}{\partial t} &= \varepsilon_j(\mathbf{R}) \chi_j(\mathbf{R}, t) - \sum_\alpha \frac{1}{2M_\alpha} \nabla_\alpha^2 \chi_j(\mathbf{R}, t) \\
 &\quad - \sum_i [\mathbf{D}_{ij}(\mathbf{R}) \chi_i(\mathbf{R}, t)] - \sum_i [G_{ij}(\mathbf{R}) \chi_i(\mathbf{R}, t)]
 \end{aligned} \tag{2.1.6}$$

Here, the nonadiabatic coupling terms  $\mathbf{D}_{ij}(\mathbf{R})$  and  $G_{ij}(\mathbf{R})$ , which mediate coupling between the nuclear and electronic degrees of freedom, are introduced(16, 44, 49):

$$\begin{aligned}
 \mathbf{D}_{ij}(\mathbf{R}) &\equiv \sum_\alpha \frac{1}{M_\alpha} \langle \phi_j(\mathbf{r}; \mathbf{R}) | \nabla_\alpha \phi_i(\mathbf{r}; \mathbf{R}) \rangle \cdot \nabla_\alpha = \sum_\alpha \frac{1}{M_\alpha} d_{ij}^\alpha \cdot \nabla_\alpha \\
 G_{ij}(\mathbf{R}) &\equiv \sum_\alpha \frac{1}{M_\alpha} \langle \phi_j(\mathbf{r}; \mathbf{R}) | \nabla_\alpha^2 \phi_i(\mathbf{r}; \mathbf{R}) \rangle
 \end{aligned} \tag{2.1.7}$$

The matrix elements of the nuclear gradient operator  $d_{ij}^\alpha$  are called **nonadiabatic coupling matrix elements** (NACME). In cases where  $\mathbf{D}_{ij}(\mathbf{R})$  and  $G_{ij}(\mathbf{R})$  can be neglected, equation (2.1.6) becomes a Schrödinger-like equation for the nuclear wave functions in the potential of the electrons.(39) The  $\varepsilon_i(\mathbf{R})$  are therefore referred to as **potential energy surfaces** (PES). The neglect of  $\mathbf{D}_{ij}(\mathbf{R})$  and  $G_{ij}(\mathbf{R})$  is the adiabatic Born-Oppenheimer approximation(39), which gives a picture of nuclear dynamics occurring on discrete electronic states. Within this approximation, the electrons and nuclei can be modeled independently, therefore greatly simplifying the calculations. In

order to address the validity of this approximation, consider the following deduction to obtain another form of the NACME(50):

Take the nuclear derivative of the electronic Schrödinger equation multiplied by  $\langle \phi_j(\mathbf{r}; \mathbf{R}) |$ :

$$\begin{aligned} \langle \phi_j(\mathbf{r}; \mathbf{R}) | \nabla_\alpha \widehat{H}_{el} | \phi_i(\mathbf{r}; \mathbf{R}) \rangle + \langle \phi_j(\mathbf{r}; \mathbf{R}) | \widehat{H}_{el} | \nabla_\alpha \phi_i(\mathbf{r}; \mathbf{R}) \rangle = \\ \langle \phi_j(\mathbf{r}; \mathbf{R}) | \nabla_\alpha \varepsilon_i | \phi_i(\mathbf{r}; \mathbf{R}) \rangle + \langle \phi_j(\mathbf{r}; \mathbf{R}) | \varepsilon_i | \nabla_\alpha \phi_i(\mathbf{r}; \mathbf{R}) \rangle \end{aligned} \quad (2.1.8)$$

The first term of the right hand side evaluates to zero, as the derivative of the eigenvalue does not influence the integral. Therefore, this simplifies to:

$$\langle \phi_j(\mathbf{r}; \mathbf{R}) | \nabla_\alpha \widehat{H}_{el} | \phi_i(\mathbf{r}; \mathbf{R}) \rangle + \varepsilon_j \langle \phi_j(\mathbf{r}; \mathbf{R}) | \nabla_\alpha \phi_i(\mathbf{r}; \mathbf{R}) \rangle = \varepsilon_i \langle \phi_j(\mathbf{r}; \mathbf{R}) | \nabla_\alpha \phi_i(\mathbf{r}; \mathbf{R}) \rangle \quad (2.1.9)$$

This can be solved for  $\mathbf{d}_{ij}$ :

$$d_{ij}^\alpha = \langle \phi_j(\mathbf{r}; \mathbf{R}) | \nabla_\alpha \phi_i(\mathbf{r}; \mathbf{R}) \rangle = \frac{1}{\varepsilon_i - \varepsilon_j} \langle \phi_j(\mathbf{r}; \mathbf{R}) | \nabla_\alpha \widehat{H}_{el-el} | \phi_i(\mathbf{r}; \mathbf{R}) \rangle \quad (2.1.10)$$

In a similar manner,  $G_{ij}(\mathbf{R})$  is proportional to  $|\varepsilon_i(\mathbf{R}) - \varepsilon_j(\mathbf{R})|^{-2}$  and therefore typically neglected. The terms  $d_{ij}^\alpha$  cannot be neglected when two electronic states are close in energy and can mediate the population transfer between these states. In fact, when the energies of two states are identical,  $\varepsilon_i = \varepsilon_j$ , the NACME has a singularity and marks a conical intersection (CI). While the nonadiabatic coupling can be neglected for reactions in the electronic ground state, this is not the case for photochemistry. Here, several excited states are involved, which generally will couple. Especially transition metal complexes have a high density of electronic states(51), which increases the probability of nonadiabatic events. Thus, for the correct description of the excited-state dynamics of metal complexes, a coupled description of both nuclear and electronic degrees of freedom is required.

A fully quantum mechanical description can be achieved most accurately by direct numerical solution of the TDSE under inclusion of the nonadiabatic coupling terms. However, this requires accurate precalculation and parametrization of the PESs over the

entire range of nuclear conformations. As the computational cost of the precalculation of the PES scale exponentially with the number of degrees of freedom, current state-of-the-art computations are limited to molecules with a single-digit number of atoms.(16) The computational cost can be reduced by using time-dependent nuclear basis sets like it is done in the multi-configurational time-dependent Hartree (MCTDH) method(17). As the basis set can adapt during the dynamics, a much smaller number of basis functions is needed. However, the formal scaling is still exponential, so that even with approximate multilayer techniques only medium-sized molecules can be treated(52, 53). Thus, for the description of big transition metal complexes, more rigorous approximations need to be used, which can be introduced by semi-classical treatment of the nuclei, for example with trajectory-based methods. Two of these methods have been employed over the course of this thesis and are detailed in the following section.

## ***2.2 Ways to approximate the nuclear dynamics – Trajectory-based methods***

Trajectory-based methods are advantageous, as they do not show the unfavorable exponential scaling with the number of degrees of freedom like methods, which directly solve the TDSE. Because the electronic structure information is calculated on-the-fly, the number of electronic structure calculations is reduced. Therefore, one can include all degrees of freedom in the calculation, hence enabling calculations of bigger molecules. However, this can only be achieved by introducing certain approximations. Two very promising approaches and further approximations they require are detailed in the following two subsections in order to give a basic understanding of the limitations of these methods.

### **2.2.1 Surface Hopping**

The method dominating in literature for the calculation of nonadiabatic dynamics is probably Tully's surface hopping(24, 25). In this method, the nuclear wave function is simulated by a swarm of independent, classical trajectories along Born-Oppenheimer PESs. Nonadiabatic effects are taken into account by hops of trajectories between PESs.



For each trajectory  $\gamma$ , the molecular wave function is represented as a linear combination of electronic wave functions:(44)

$$\Psi^\gamma(\mathbf{r}, \mathbf{R}, t) = \sum_i^\infty C_i^\gamma(t) \phi_i^\gamma(\mathbf{r}; \mathbf{R}) \quad (2.2.1)$$

The absolute square of the complex coefficients  $|C_i^\gamma|^2$  gives the probability of finding trajectory  $\gamma$  on state  $i$ . These coefficients are of high importance for the modeling of the hopping process. Similar to equation (2.1.6), this ansatz can be inserted into the Schrödinger equation and under negligence of the second order couplings  $G_{ij}(\mathbf{R})$  and the use of the chain rule, one gets the coupled equations that are used to propagate the complex coefficients of the trajectories (44):

$$i \frac{dC_j^\gamma(t)}{dt} = \varepsilon_j(\mathbf{R}) C_j^\gamma(t) + \sum_i \left[ C_i^\gamma(t) \sum_\alpha \frac{1}{M_\alpha} d_{ij}^\alpha \cdot \dot{\mathbf{R}}_\alpha^\gamma \right] \quad (2.2.2)$$

Here, the  $\dot{\mathbf{R}}^\gamma$  are the nuclear velocities of trajectory  $\gamma$ . The **hopping probability** from state  $i$  to state  $j$  in the time interval  $[t, t + dt]$  is then calculated as follows:(44)

$$h_{ij}^\gamma(t, t + dt) = 2 \int_t^{t+dt} \frac{-\text{Re} \left[ C_j^\gamma(\tau) C_i^{\gamma*}(\tau) \sum_\alpha \frac{1}{M_\alpha} d_{ij}^\alpha \cdot \dot{\mathbf{R}}_\alpha^\gamma \right]}{C_i^\gamma(\tau) C_i^{\gamma*}(\tau)} d\tau \quad (2.2.3)$$

Within the fewest switches surface hopping (FSSH) algorithm, a hop occurs from state  $i$  to state  $j$  only when for a randomly generated number  $\zeta$  between 0 and 1 the following relation is fulfilled:(25, 54)

$$\sum_{k \leq j-1} h_{ik}^\gamma < \zeta < \sum_{k \leq j} h_{ik}^\gamma \quad (2.2.4)$$

The population of each state is then averaged over the whole swarm in order to obtain lifetimes by fitting an exponential decay to the time dependence of the population. This algorithm has been employed very successfully to calculate lifetimes and quantum yields(20), even though it is not derived from first principles and is therefore not guaranteed to converge to the right solution. Each trajectory only populates one state

per time step, which makes the evaluation of the averaged time evolution of properties like the population straightforward.

Despite the success in the application of FSSH to a number of systems, the uncoupled propagation of the individual trajectories can result in failures to describe some quantum mechanical effects. One of these effects that is of particular interest for this thesis is the **decoherence** of wave functions, which is explained in more detail using the one-dimensional example PES in Figure 1. When the system enters a coupling region at the coupling time  $t_{c1}$ , population is transferred from PES 1 to PES 2. With time evolving, the part of the wave function that is on PES 2 hits a barrier and is reflected, while the part of the wave function that is on PES 1 is accelerated downhill. At time  $t_{c2}$ , the part of the wave function that is on PES 2 reenters the coupling region and transfers population back to PES 1. However, within FSSH, population transfer is described exclusively by surface hops. The average of the populations of the swarm should then resemble the changes in the quantum mechanical amplitudes  $|C_i^\gamma|^2$ . In order to achieve this, the hopping probability depends on the product of the complex amplitudes  $C_j^\gamma(\tau)C_i^{\gamma*}(\tau)$ , which represents the overlap between wave functions on different PES. However, as in SH the trajectories are independent and dynamics of each trajectory are driven by only one PES, this product  $C_j^\gamma(\tau)C_i^{\gamma*}(\tau)$  always has to be calculated as if all wave functions were located at the position of the trajectory driving the dynamics. In the example described above, this is however not a good approximation, because the actual wave function overlap will be lower than the product  $C_j^\gamma(\tau)C_i^{\gamma*}(\tau)$  when the wave functions are spatially separated as in the example shown in Figure 1 b). Therefore, the hopping probability in Figure 1 f), which depends on the product  $C_j^\gamma(\tau)C_i^{\gamma*}(\tau)$  rather than the actual wave function overlap, is too high and can therefore lead to incorrect hops. Thus, the calculated lifetimes can be too short, as has been observed before.<sup>(18, 55, 56)</sup> Such effects are expected especially for transition metal complexes as they have complicated electronic structures. Therefore, extensions of SH to include decoherence are proposed.<sup>(18)</sup>

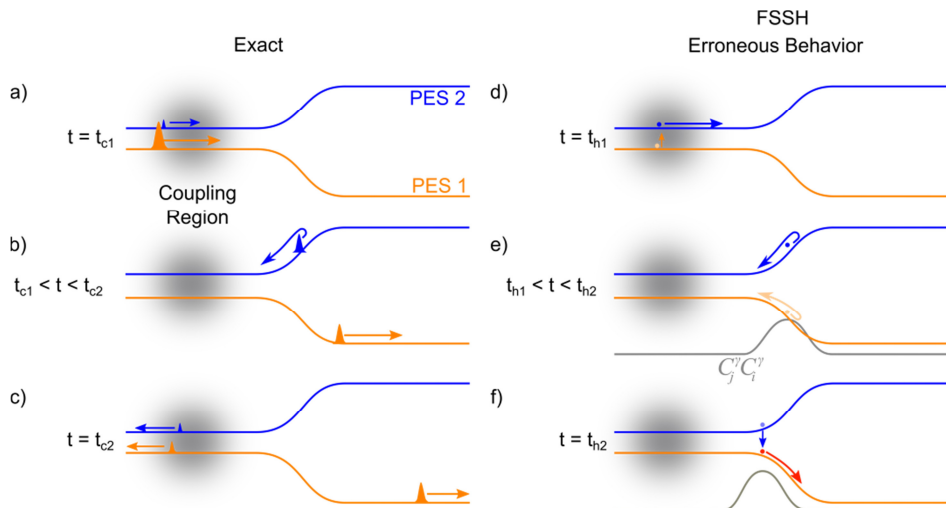


Figure 1: Exemplaric depiction of the decoherence problem. The first column shows the correct quantum mechanical behavior of the wave packet: a) at the first coupling time  $t_{c1}$ , population is transferred from wave packet 1 on PES 1 to wave packet 2 on PES 2. b) With time evolving, wave packet 2 hits a barrier and is reflected, while wave packet 1 is accelerated downhill on PES 1. c) The second population transfer occurs at  $t_{c2}$  when wave packet 2 revisits the coupling region. The second column depicts the errors that can occur in FSSH exemplarily for one trajectory of the swarm. (Opaque dots mark the electronic state, which drives the dynamics; translucent dots depict how other electronic states are taken into account.): d) at the first hopping time  $t_{h1}$ , a hop of trajectory 1 on PES 1 to PES 2 occurs. e) With time evolving, the trajectory hits a barrier and is reflected. The product of the complex coefficients  $C_j^i(\tau)C_i^j^*(\tau)$  (gray line), which influences the hopping probability does not decrease accordingly. f) Thus, the second hop can occur too early,  $t_{h2} < t_{c2}$ .

### 2.2.2 Multiple Spawning

One possibility to circumvent the decoherence problem that FSSH suffers from is the application of the full multiple spawning (FMS) algorithm, which is derived from first principles. This method is based on a formally exact ansatz for the nuclear wave function  $\chi_l(\mathbf{R}, t)$  evolving in an electronic state  $l$ . However, this ansatz is only exact when a complete basis is used. In practice, the basis set size is finite and adapted over time (39) in order to achieve the best compromise between accuracy and computational cost. Within FMS,  $\chi_l(\mathbf{R}, t)$  is described as a linear combination of 3N-dimensional Gaussian basis functions  $\Xi_j^l$  with frozen width  $\alpha$  called **trajectory basis functions** (TBFs).<sup>(57)</sup>

$$\chi_l(\mathbf{R}, t) = \sum_{j=1}^{N_l(t)} C_j^l(t) \Xi_j^l(\mathbf{R}; \bar{\mathbf{R}}_j^l(t), \bar{\mathbf{P}}_j^l(t), \bar{\gamma}_j^l(t), \alpha_j^l) \quad (2.2.5)$$

The positions  $\bar{\mathbf{R}}_j^I(t)$  and momenta  $\bar{\mathbf{P}}_j^I(t)$  of each Gaussian basis function follow classical trajectories, while the phase  $\bar{\gamma}_j^I$  is integrated semi-classically.(57) The complex amplitudes  $C_j^I$  carry information about the populations of the electronic state  $I$  and are propagated fully quantum mechanically, therefore enabling a sufficiently accurate description of nuclear quantum effects, like decoherence. The equations of motion for the amplitudes associated with electronic state  $I$  are obtained by inserting equation (2.2.5) into the time-dependent Schrödinger equation for nuclear wave functions:(57)

$$\frac{d}{dt}\mathbf{C}^I(t) = -i(\mathbf{S}_{II}^{-1}) \left[ \left[ \mathbf{H}_{II} - i\dot{\mathbf{S}}_{II} \right] \mathbf{C}^I + \sum_{J \neq I} \mathbf{H}_{IJ} \mathbf{C}^J \right] \quad (2.2.6)$$

Here,  $\mathbf{S}_{II}(t)$  and  $\dot{\mathbf{S}}_{II}(t)$  are the overlap matrix and it's time derivative, and the matrix elements of  $\hat{H}_{IJ}$  are defined as follows:(39)

$$\left( \hat{H}_{IJ} \right)_{kk'} = \langle \Xi_k^I | \hat{T}_{nuc} | \Xi_{k'}^J \rangle \delta_{IJ} + \langle \Xi_k^I | \varepsilon_I^{el} \delta_{IJ} | \Xi_{k'}^J \rangle - \langle \Xi_k^I | \sum_{\alpha=1}^{3N} \frac{1}{M_{\alpha}} d_{IJ}^{\alpha} \nabla_{\alpha} | \Xi_{k'}^J \rangle \quad (2.2.7)$$

Here, an approximation is introduced by neglecting the second order couplings  $G_{ij}(\mathbf{R})$ .

In order to use FMS in combination with on-the-fly electronic structure calculations, two more approximations need to be introduced. These are only listed here briefly and the interested reader is referred to the literature for a more detailed explanation of these approximations:(39, 57) 1) The *independent first generation approximation* (IFG) uncouples the initial TBFs, therefore considering them independent starting from  $t=0$ . This makes it possible to run the dynamics of the different initial TBFs in parallel. 2) The *saddle-point approximation* uses the spatial localization of the TBFs to simplify the calculation of the integrals in equation (2.2.7). If both of these approximations are used, the method is usually called **ab-initio multiple spawning** (AIMS).

The central and name-giving idea of multiple spawning is to adapt the nuclear basis set size during the simulation as needed.(57) This is done within the spawning algorithm that adds new TBFs to the simulation in regions of high nonadiabatic coupling, *e.g.* close to conical intersections. The initial positions and momenta are sampled *via* a Wigner

distribution around the ground state and called the **initial conditions**. The simulation starts with one TBF per initial condition, the parent TBF, which can then spawn new child TBFs, which leads to an increasing number of TBFs during the simulation. Especially for the high number of states that are of importance for the description of big transition metal complexes, this might lead to a fast increase in the number of TBFs. As the computational cost increases formally quadratic with the number of TBFs, another approximation is needed to reduce the number of TBFs during the dynamics if possible. This approximation is called **stochastic selection (SS)**.<sup>(58)</sup> Under the premises that the TBFs can be grouped into different uncoupled blocks, the SS algorithm stochastically chooses one block of TBFs to continue running the dynamics, while the other TBFs are terminated. The basic idea behind this, is similar to the SH approach. However, as only uncoupled blocks of TBFs are terminated, the nuclear quantum effects can still be described. The thus achieved reduction in TBFs makes the computation of systems with more than five excited states feasible.

### ***2.3 Results: Comparison of FSSH and AIMS for one example organic molecule***

The methods introduced in the preceding section have so far mostly been used to model organic molecules.<sup>(18, 26-29, 39-42)</sup> In comparison to transition metal complexes, organic molecules mostly possess simpler electronic structures.<sup>(43, 59)</sup> Hence, they can be used to highlight some of the challenges that are already known and that occur even for systems with a low number of excited states relevant to describe the dynamics. To the best of my knowledge, there have been only very few comparisons of surface hopping and multiple spawning methods.<sup>(60-64)</sup> Some of them focused on the FMS rather than the here-used AIMS, using model PES<sup>(60)</sup> or precalculated PES<sup>(61, 63)</sup>. Another study<sup>(62)</sup> showed a 25 % shorter  $S_1$  lifetime for FSSH than for AIMS, which is attributed to decoherence effects. However, decoherence effects are more likely to occur, when several excited states are involved, as the energy difference between excited states<sup>1</sup> is generally smaller than the  $S_0 - S_1$  energy difference. Therefore, in the

---

<sup>1</sup> The large stokes-shift between the experimental absorption and fluorescence spectra hinted to the involvement of two electronic transitions.

following a comparison of AIMS and FSSH is presented for an organic molecules with two excited states of interest for its dynamics<sup>2</sup>, *i.e.* *N*-phenyldihydrotriacanthracene (see inset Figure 2), called azaacene for brevity in the following. With this example calculation, the consequences of the decoherence problem for a rather simple case with two excited states can be illustrated. These effects are expected to be even more pronounced for molecules with more complicated PES, like transition metal complexes.

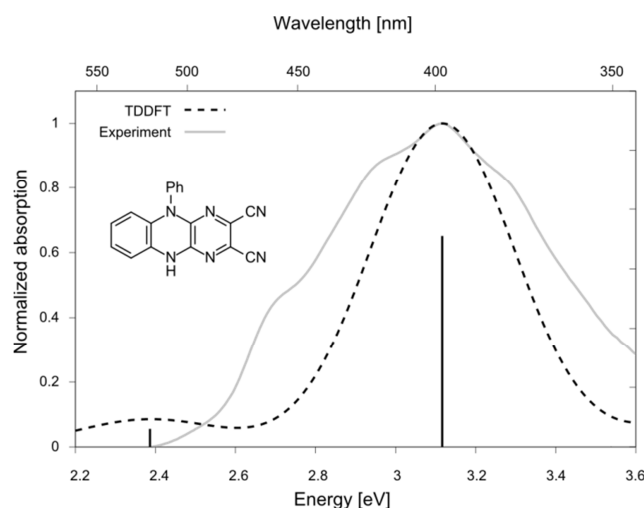


**Figure 2:** Calculated and experimental absorption spectra of the azaacene shown in the inset. The black dashed line represents the theoretical spectrum, calculated with B3LYP and Ahlrich's double zeta basis set(65) with polarization functions. The theoretical spectrum has been shifted by 0.42 eV and broadened by a Gaussian function with full width half maximum (FWHM) of 0.5 eV to better fit the experiment, as is customary. The experimental spectrum (gray line) was measured in toluene with a concentration of 32  $\mu\text{mol/l}$ .

Before the dynamics of a system can be calculated, it is necessary to obtain basic knowledge about the electronic states involved. Therefore, the experimental and calculated absorption spectra are investigated (shown in Figure 2). The azaacene features a broad absorption in the visible range. This absorption mostly consists of one electronic transition at about 3.1 eV broadened by vibrational progression. A second transition of very low intensity is present at 2.4 eV, according to the calculations. Thus, in the Franck-Condon region both excited states are separated significantly in energy by 0.7 eV. Experimental excitation at 3.1 eV will result in a transition from  $S_0$  to  $S_2$ . Therefore, in

<sup>2</sup> With the ESM chosen (TDDFT, see appendix 7.4) the transition between ground state and excited state cannot be described correctly. Therefore, a molecule was chosen so that the transition between  $S_2$  and  $S_1$  could be investigated.

the following the focus of the excited-state dynamics lies on the internal conversion from  $S_2$  to  $S_1$ .

The excitation into  $S_2$  is modeled by a projection of the ground state wave function onto the PES of  $S_2$ . FSSH and AIMS are calculated with the same ESM<sup>3</sup> for the underlying PES and using the same 20 initial conditions to maximize comparability. The resulting changes of the  $S_2$  population are shown in Figure 3. An exponential fit of the population changes of  $S_2$  yields the respective lifetime. For AIMS, it is about eight times higher than for FSSH. It is known that FSSH can yield too short lifetimes because of the decoherence problem. Evidence for the probable importance of decoherence is given by the number of nonadiabatic events during the dynamics, as represented by hops and spawns for FSSH and AIMS, respectively, listed in Table 1. In the simplest case, one nonadiabatic event is sufficient to transfer the population from one state to another. However, on average, there are three nonadiabatic events between  $S_2$  and  $S_1$  in the AIMS calculations and therefore the average number of TBFs that are simultaneously present in the dynamics rises up to 3 within 200 fs (see inset Figure 3). This leads to the conclusion that most likely more than one TBF is evolving in  $S_1$  at the same time. The decoherence between these wave functions cannot be described correctly with FSSH. This leads to a higher number of over 5 hops compared to about 3 spawns in AIMS and the low lifetime of about 40 fs.

**Table 1: Lifetimes  $\tau$  as obtained by a fit of the nonadiabatic dynamics results for AIMS and FSSH and the average number of nonadiabatic events, number of spawns and hops for AIMS and FSSH, respectively. The underlying TDDFT calculations were done with the same parameters as given in the caption of Figure 2.**

Method	AIMS	FSSH
$\tau$ [fs]	313	41
Average number of nonadiabatic events (between $S_1$ and $S_2$ )	2.95	5.45

Another significant difference between the methods is the improved smoothness of the curve for AIMS in comparison to the FSSH. This is due to the fact that in AIMS population does not have to hop like in FSSH but only parts of the population can be transferred

<sup>3</sup> B3LYP with Ahlrich's double zeta basis set with polarization functions was used as ESM. For AIMS (FSSH) the software TeraChem (Turbomole) was used to calculate the underlying PES. The NewtonX (FMS90) implementation of FSSH (AIMS) was used.

between TBFs, which is facilitated by the increasing number of TBFs. In this calculation, a total of 101 TBFs are present after 500 fs. Therefore, the spread of the population can be described in more detail with AIMS using the same number of initial conditions. However, the number of electronic structure calculations and therefore the computational cost for the calculation of one initial condition is higher for AIMS than for FSSH because of the growing number of TBFs and because the TBFs are coupled.

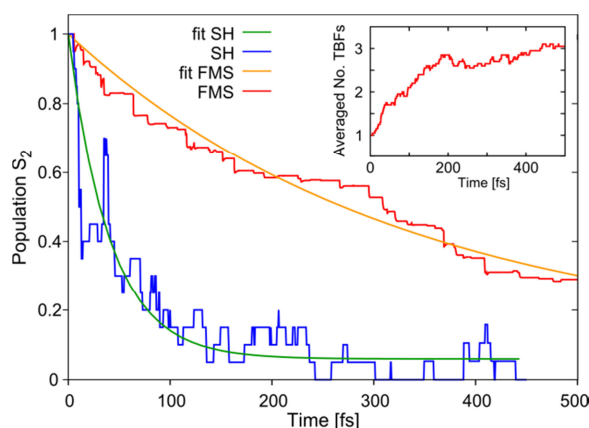


**Figure 3:** Population change according to AIMS and SH calculations for the azaacene in red and blue, respectively. The data is averaged over 20 initial conditions. AIMS data contains also contributions of  $S_3$  and  $S_4$ . Orange and green lines show the exponential fit of the population for AIMS and SH, respectively. Underlying TDDFT calculations were done with B3LYP and Ahlrichs double zeta basis set with polarization functions. Inset: Change of the number of TBFs for the AIMS dynamics averaged over all 20 initial conditions.

The computational cost per initial condition can be reduced by choosing a particularly efficient implementation of a desired ESM.<sup>4</sup> One very efficient implementation of ESMs based on graphical processing units is realized in the software TeraChem, which can yield speedups of over 400 times compared to CPU-implementations like GAMESS.<sup>(66)</sup> I put into practice the first interface of FMS90, the only implementation of AIMS, with TeraChem to work with transition metal complexes as part of this thesis. I used this combination for the calculations in the following chapters. However, based on my interface meanwhile remodeling has happened to facilitate easier addition of new ESMs to the interface.

In summary, AIMS has several advantages over FSSH. It was shown here for the first time for an organic molecule, that decoherence effects between excited states can be

<sup>4</sup> For details about the ESMs see the next chapter and the appendix



described better with AIMS than with FSSH because of the fully quantum mechanical treatment of the population transfer in AIMS. Furthermore, a lower number of initial conditions is necessary for convergence for AIMS than for FSSH. With the here-implemented interface to TeraChem also the simulations of each initial condition can be calculated faster than with FSSH in combination with CPU-implementations of the ESM, as *e.g.* the here-used program Turbomole. For the rest of this thesis, I therefore employed the combination of AIMS with TeraChem.

### 3 Quantum mechanical description of the electronic structure – Example Fe(CO)<sub>5</sub>

In the previous chapter, it was detailed that a high number of electronic structure calculations are necessary for the description of the ultrafast dynamics of a molecular system. Therefore, it is important to find a method of very high computational efficiency that enables such extensive computations. However, the accuracy of the underlying PES is also essential because trustworthy results can only be obtained when the calculated forces and nonadiabatic couplings at least qualitatively agree with the exact values. Thus, a balance between the conflicting requirements of accuracy and computational effort is even more important for nonadiabatic dynamics than for stationary quantum chemistry calculations.<sup>(57, 67)</sup> Additionally, during the simulation, not just the Franck-Condon region needs to be described with sufficient accuracy. Therefore, in the following subsection, the accuracy and computational effort of different methods are compared to each other to identify a suitable candidate for the description of the nonadiabatic dynamics of transition metal complexes. An overview over the most important criteria for the comparison can be found in Table 2. A more in-depth description of the computational methods mentioned here is given in sections 7.1 to 7.4 in the appendix. The method of choice is then used for the calculation of the dissociation dynamics of ironpentacarbonyl, detailed in section 3.2.

#### 3.1 Accuracy and computational cost of electronic structure methods

The most accurate description of the electronic wave function can be achieved with the **full CI** (full configuration interaction, see section 7.2 in the appendix) method.<sup>(68)</sup> However, this method is so expensive (see Table 2) that even for stationary calculations mostly only diatomic molecules can be handled.<sup>(69)</sup> Therefore, full CI is often approximated by truncating the number of excitations included in the simulation, e.g. as in **CISD** (configuration interaction singles and doubles), **CCSD** (coupled-cluster singles-and-doubles) or other higher order truncations (see section 7.2 in the appendix for more detailed information on these truncations).<sup>(68)</sup> However, such single-reference methods only describe dynamic correlation<sup>(70)</sup> and have problems describing conical

intersections correctly.<sup>(57)</sup> Therefore, they are not accurate enough to be used in excited-state dynamics calculations.<sup>(57)</sup>

An alternative method is **CASSCF** (complete active space self-consistent field, see also section 7.3 in the appendix), which employs full CI only for a hand-picked subset of orbitals.<sup>(68)</sup> CASSCF includes static correlation and has been successfully employed in the calculation of the nonadiabatic dynamics for a number of small to medium-sized organic molecules<sup>(26-28, 40)</sup> and very recent advances in the use of graphical processing units made calculations of provitamin D<sub>3</sub>, a molecule with over 50 atoms, possible.<sup>(41)</sup> However, CASSCF does not accurately describe the dynamic correlation.<sup>(70)</sup> This can be added *via* a perturbation-theory post-treatment, called **CASPT2** (complete active space perturbation theory second order).<sup>(68)</sup> But, as this calculation has to be done on top of the CASSCF calculation, it is even more expensive and therefore up to now limited to nonadiabatic dynamics simulations of small molecules ( $\lesssim$  35 atoms)<sup>(29, 42, 71)</sup>. A disadvantage for the application to transition metal complexes of both CASSCF and CASPT2 is the state-averaging procedure that has to be used to obtain the orbitals.<sup>(72)</sup> In case of transition metal complexes, a high number of states of often very different character can be important, which might result in orbitals that are not meaningful when averaged over. For calculations at the Franck-Condon point, symmetry constraints can be used to circumvent this problem and to lower the computational cost.<sup>(73)</sup> However, this cannot be used for dynamics simulations, as a great variety of mostly non-symmetric configurations is of importance for the dynamics. All in all, CASSCF and CASPT2 cannot be used for the calculation of big transition metal complexes because the high computational cost limits the calculations to molecules with approximately 50 atoms and the state-averaging limits the simulation to a low number of excited states.

The computational cost of CASSCF and CASPT2 can be lowered by excluding negligible configurations from the calculation.<sup>(74)</sup> This is done by a partitioning of the active space and restricting the occupation numbers of each part of the active space.<sup>(75)</sup> This approach called **GAS** (generalized active space) and its special case **RAS** (restricted active space) have been successfully used to model transition metal complexes (see section 7.3 in the appendix for details on GAS and RAS).<sup>(76, 77)</sup> However, these methods are also

based on a state-averaging procedure to obtain the orbitals.(78) Furthermore, in such calculations, orbitals of different subspaces can swap, which makes the active space unstable upon geometry changes.(79) Because of these instabilities of the active space and the necessity to use state-averaging to obtain the orbitals, GAS techniques are not the method of choice for modeling the excited-state dynamics of transition metal complexes.

**Table 2: Comparison of the accuracy and computational cost of different ESMs.**

	Accuracy				Computational	
	Static correlation	Dynamic correlation	State-averaging	Conical inter-sections	Doubly excited states	cost (Formal scaling*)
Full CI	Yes	Yes	No	Yes	Yes	Factorial (68)
CISD	No	Yes	No	No	Yes	Sixth order (80)
CCSD	No	Yes	No	No	Yes	Sixth order (80)
CASSCF	Yes	No	Yes	Yes	Yes	Exponential (81)
CASPT2	Yes	Yes	Yes	Yes	Yes	Exponential (81)
RASSCF	Yes	No	Yes	Yes	Yes	Exponential (81)
RASPT2	Yes	Yes	Yes	Yes	Yes	Exponential (81)
TDDFT	Depends on the functional		No	Not to S <sub>0</sub>	No	Third order (80)

\* For active space methods, the formal scaling is a function of the size of the active space; for all other methods, the formal scaling depends on the number of basis functions.

**TDDFT** (time-dependent density functional theory, see section 7.4 in the appendix)(82) can be used as an alternative electronic structure method. This method is based on the electronic density rather than the full  $n$ -electron wave function.(83) In order to take advantage of the density being a function of only three variables, *i.e.* the three Cartesian coordinates, the Kohn-Sham formalism is introduced(84): Within this formalism, the density of the full system is constructed from the wave function of noninteracting electrons rather than from the full wave function of the interacting electrons. Instead, the interactions between electrons are included solely *via* the potential of the noninteracting system.(83) Thus, giving it very low computational costs and making it

computationally feasible to use for the simulation of the dynamics of big molecules.<sup>(85)</sup> However, the accuracy of the calculation depends on the density functional that is used to approximate the potential of the noninteracting system (see section 7.4 in the appendix for a more detailed explanation).<sup>(77, 83)</sup> A number of different functionals has been proposed, some of which have been shown to accurately model the excited states of transition metal complexes in the Franck-Condon region.<sup>(7, 86, 87)</sup> Moreover, TDDFT has been used before for an exploratory investigation of the dynamics of a big transition metal complex.<sup>(31)</sup> Furthermore, within this method, an arbitrary number of states can be calculated as no averaging procedure is needed, thus avoiding possible inaccuracies caused by such an averaging procedure. However, because the excited states are calculated on top of the ground state calculation and therefore treated on a different footing, conical intersections between the ground state and the excited states cannot be described accurately within TDDFT.<sup>(88)</sup> This is usually no disadvantage for the investigation of transition metal complexes, as the ultrafast photochemical processes of interest involve often only the excited states, meaning that no transitions to the ground state need to be simulated. However, the approximation of the unknown exchange-correlation functional and other approximations within this method lead to deficiencies with the description of doubly excited states and charge-transfer states.<sup>(83)</sup> Therefore, in the following section, the accuracy of TDDFT for the description of transition metal complexes is investigated *via* a comparison to experiments and the very accurate method CASPT2. In this comparison, only a low number of states is included to avoid inaccuracies in the CASPT2 calculations, which might arise from state-averaging.

### **3.2 Results for the photodissociation of Fe(CO)<sub>5</sub>**

One transition metal complex with a particularly difficult-to-describe electronic structure but a low number of atoms is ironpentacarbonyl (see Figure 4 a)).<sup>(89)</sup> This complex has a particularly high number of dark states in the UV and vis spectral ranges.<sup>(89)</sup> Furthermore, the investigated mechanism, a photodissociation, suggests the involvement of states with double excitation character, which are known to be difficult to describe within TDDFT.<sup>(83)</sup> Therefore, it is particularly suitable to exemplify how TDDFT can be used to describe a complicated electronic structure and how the limits of

TDDFT can be identified with a comparison to more accurate CASPT2 calculations. Fe(CO)<sub>5</sub> was above all chosen for the investigation as the photodissociation of its carbonyl ligands was studied intensely in different experiments.<sup>(90-92)</sup> Photoexcitation of ironpentacarbonyl at different energies, *i.e.* 3.53, 5.00 and 6.42 eV, gives rise to different concentrations of the fragments Fe(CO)<sub>x</sub>, x=4, 3, 2, 1<sup>(90)</sup>. From this wavelength dependence of the number of dissociated carbonyls, it is concluded that the carbonyl ligands are dissociating sequentially and that even the excitation in the very low energy tail of the absorption spectrum leads to the dissociation of the first carbonyl ligand.<sup>(90)</sup> Transient femtosecond pump-probe photoionization mass spectra pumped at 4.66 eV confirm the sequential dissociation of the carbonyl ligands of Fe(CO)<sub>5</sub>.<sup>(91)</sup> These experimental results were analyzed with the aid of previously published CASSCF calculations.<sup>(93-96)</sup> The very fast dissociation in combination with the theoretical results led to the conclusion that, after the initial excitation, all equatorial carbon-iron bonds are elongated, before the first carbonyl dissociates within less than 100 fs after excitation.<sup>(91)</sup> The study of Ihee *et al.*<sup>(92)</sup> gives further hints for the dissociation of an equatorial carbonyl. In this study<sup>(92)</sup>, ultrafast electron diffraction was measured with a time resolution in the picosecond range. These experiments can be used to directly determine the transient molecular structure of the photoexcited Fe(CO)<sub>4</sub>.<sup>(92)</sup> For these measurements, the complex is excited by two-photon absorption at the energy of 4 eV, followed by a probing electron pulse to record the diffraction pattern.<sup>(92)</sup> This was used to determine that Fe(CO)<sub>4</sub> is formed in a singlet rather than triplet structure.<sup>(92)</sup> As the structure of the singlet Fe(CO)<sub>4</sub> resembles very closely the structure of Fe(CO)<sub>5</sub> with one equatorial carbonyl ligand removed, this hints to dissociation of an equatorial carbonyl from Fe(CO)<sub>5</sub>.

In order to calculate the dynamics for a comparison to the experimental results, the UV-vis absorptions spectra are investigated to choose a density functional and to obtain basic knowledge about the excited states of Fe(CO)<sub>5</sub>, as detailed in the following subsection. This lays the foundation to identify which states are pumped by the different excitation wavelengths that have been used experimentally. Here, special focus lies on the 4.66 eV excitation used by Trushin *et al.*<sup>(91)</sup> who detailed the femtosecond dynamics of ironpentacarbonyl. The ultrafast dynamics are then presented in subsection

3.2.2. Based on some example trajectories, the quality of the underlying PES as calculated with TDDFT is evaluated *via* a comparison to the CASPT2 PES in subsection 3.2.3.

### 3.2.1 Steady-state UV-vis absorption spectra

The experimental(97, 98) and calculated UV-vis absorption spectra of Fe(CO)<sub>5</sub> are shown in Figure 4. The absorption maximum lies at 6.3 eV with a pronounced low energy shoulder at around 5.1 eV that slowly tails off. All calculated spectra show three peaks, representing the main absorption, the low energy shoulder and its tail. However, B3LYP, PBE0 and  $\omega$ PBEh overestimate the intensity of the low-energy shoulder and tail. In contrast to this, PBE underestimates them. Better intensity ratios can be obtained with  $\omega$ PBE and CAMB3LYP.  $\omega$ PBE results in slightly higher energy and lower intensity for the electronic transition describing the tail, which is in better accordance with the experiment. Therefore, all further calculations are obtained using  $\omega$ PBE. The stick-spectrum for  $\omega$ PBE, shown in Figure 4, illustrates the high number and density of electronic states and transitions to these states.

The experimental 4.66 eV excitation of the shoulder was attributed to transitions to the states  $S_8$  to  $S_{10}$  obtained from previous CASSCF calculations(96) constraining the complex to  $C_{2v}$  symmetry, which are shown in blue in Figure 4 b). These transitions are of metal-to-ligand charge-transfer (MLCT) character. Corresponding transitions in the  $\omega$ PBE calculations are transitions to states  $S_{16}$  to  $S_{19}$  as the TDDFT calculations show more symmetry-forbidden and therefore optically dark transitions than the CASSCF results. This could be due to the fact that in the literature the spectrum was modeled via four individual CASSCF calculations(96) - one for each symmetry class. These were each yielding four excited states. Therefore, in this calculation not necessarily the 16 states<sup>5</sup> with the lowest energy are obtained. Another contribution can be the occurrence of low-lying states in TDDFT, which would have higher energy in CASSCF. Furthermore, in the TDDFT calculation, also states without the given symmetry constraint can be obtained.

---

<sup>5</sup> Furthermore, in reference 96. O. Rubner, V. Engel, M. R. Hachey, C. Daniel, A CASSCF/MR-CCI study of the excited states of Fe(CO)<sub>5</sub>. *Chem. Phys. Lett.* **302**, 489-494 (1999). only 14 of the 16 excited states calculated are listed.

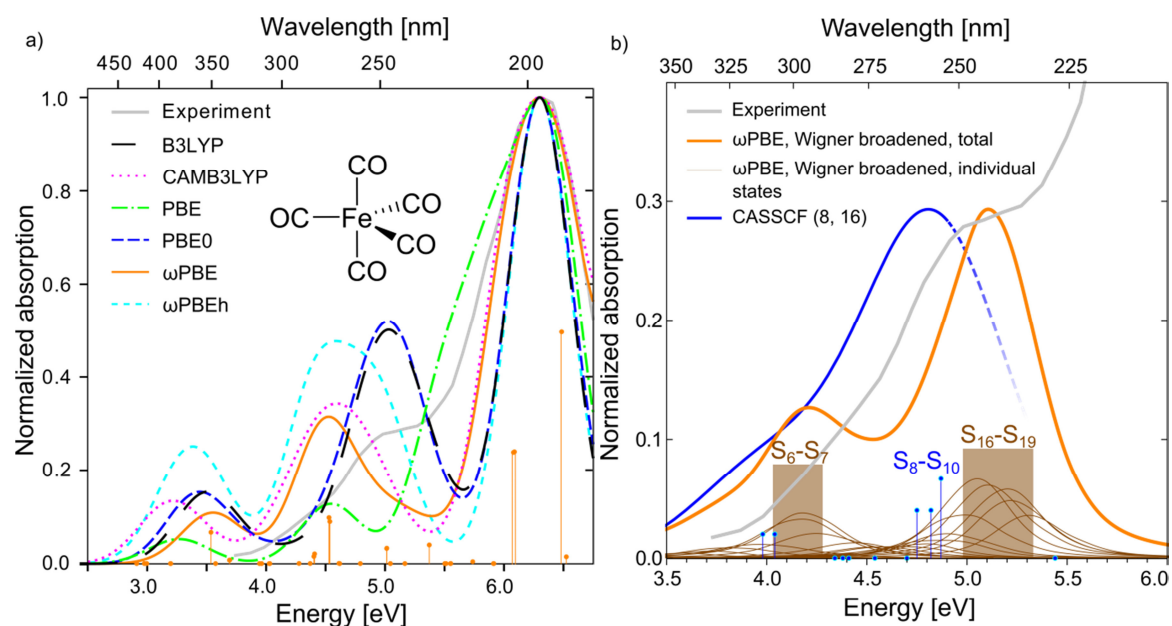


**Figure 4:** a) Normalized absorption spectra of Fe(CO)<sub>5</sub> calculated with different TDDFT functionals and experimental spectrum(97, 98) in gray. All calculation were computed using effective core potentials(99) and the associated basis set lanl2dz(100, 101) The stick spectra were broadened with a Gaussian function with a FWHM of 0.7 eV and their maxima were shifted to 6.3 eV to maximally overlap with the main experimental absorption peak. The stick spectrum for ωPBE is shown exemplarily. All spectra were calculated based on a geometry optimized with B3LYP. Inset shows the molecular structure of Fe(CO)<sub>5</sub>. b) Enlargement of the low-energy shoulder around 5.1 eV. The blue line shows literature CASSCF(96) calculations broadened with a Gaussian function with a FWHM of 0.7 eV. The orange line shows the ωPBE results for the first 20 excited singlet states, which are obtained based on 150 configurations sampled from a Wigner distribution. The contributions of each of the individual states are shown as thin brown lines. Individual sticks for each configuration were broadened by 0.25 eV before summation and shifted by 0.5 eV. The light brown rectangles mark the energy regions from which the initial conditions are selected.

A two-photon excitation with a photon energy of 2 eV, which was used by Ihee *et al.*(92) corresponds to transitions to S<sub>6</sub> and S<sub>7</sub> in ωPBE calculations. These states are of metal-centered (MC) character. The energy difference and intensity ratio between the transitions to the aforementioned MC and MLCT states is very similar for TDDFT and CASSCF. This emphasizes that with the right choice of density functional charge-transfer states can be described correctly. In the following subsection, excitations into both the low-energy MC and the high-energy MLCT bands are simulated and compared to the experimental results.

### 3.2.2 Dynamics calculations with TDDFT/AIMS

The experimental excitation of the MC and MLCT bands discussed in the last subsection are modeled by a projection of the ground-state wave function onto the respective



excited-state PES. Therefore, conformations are sampled from a Wigner distribution (for corresponding spectra see Figure 4 b)), which will be used as initial conditions. For each conformation, the population is initialized into the excited state with the highest oscillator strength in the respective energy region<sup>6</sup>, which is marked by brown rectangles in Figure 4 b). As transitions from excited states to the ground state cannot be described with TDDFT(88), the dynamics calculations were terminated before such transitions were to occur, *i.e.* when the energy difference between  $S_1$  and  $S_0$  is small enough to allow for nonadiabatic coupling between both states.

For a comparison with the experiment, a measure for the bond breaking has to be defined. This can be achieved using a dissociation bond length as a measure, as has been done in the literature.(30) Following this procedure(30), a normal distribution was fitted to all Fe-C bond lengths reached during the dynamics – dissociating as well as non-dissociating ones. All bond lengths within a range of  $2\sigma$  from the maximum of the normal distribution, *i.e.* 1.9 Å, can be considered as bound, whereas longer bond lengths are considered dissociated.(30) This yields a dissociating bond length of 2.3 Å.

#### *Dynamics after excitation of the low energy tail at around 4 eV*

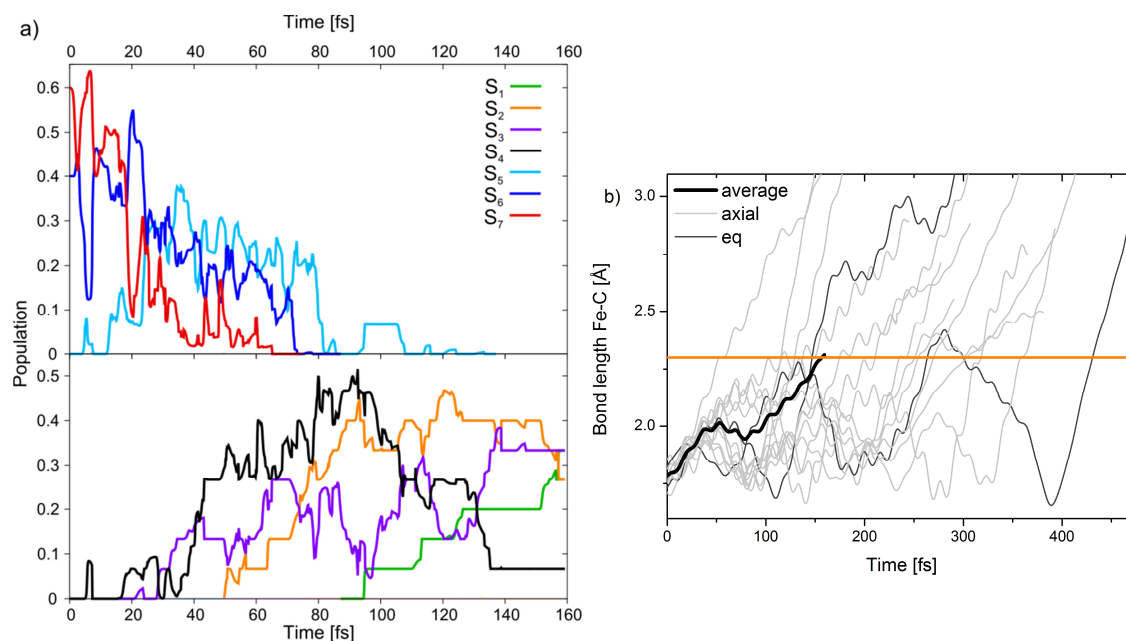
For modeling the two-photon excitation at 4 eV, five different initial conditions were used and for each of them, three calculations with different random numbers for the stochastic selection algorithm were conducted. This results in a total of 15 individual calculations, which are called “runs” for the rest of this thesis. The population for each initial condition was initially either put into state  $S_6$  or  $S_7$ , depending on the oscillator strength, as mentioned in the beginning of this subsection.

Figure 5 a) shows the population changes of the lowest seven singlet states averaged over all 15 SSAIMS runs. The population of the initially excited states  $S_6$  and  $S_7$  decays within 80 fs to 0. Within 140 fs, more than 90 % of the population is transferred to states  $S_1$ ,  $S_2$  and  $S_3$ . The dissociation starts only when one of these three states is populated. The average of the bond lengths between all dissociating carbonyl ligands and Fe increases within 150 fs from 1.8 Å to 2.3 Å. In 85 % of the runs, dissociation of an axial carbonyl was observed. The dissociation of an axial carbonyl might be favored because

---

<sup>6</sup> A slight distortion of the molecule can cause changes in the oscillator strength.

the seven lowest lying excited states are of MC character, with a partially populated  $d_{z^2}$  orbital, which points to the axial ligands. Thus, the electron density along the bonds to the axial carbonyls increase and therefore, the respective bond lengths are elongated.



**Figure 5:** a) Population change of the seven energetically lowest singlet excited states during the AIMS-dynamics averaged over all trajectory basis functions. b) Time evolution of the dissociating Fe-C bond length during the dynamics including seven excited states for all 15 SSAIMS runs and their average (thick black line). Light gray and dark gray lines are the SSAIMS runs, which ended in the dissociation of an axial and an equatorial carbonyl, respectively. The orange line marks the dissociation bond-length of 2.3 Å. The average (thick black line) reaches the dissociating bond-length at 157 fs.

The dissociation of an axial carbonyl seems to be in contrast to the experimental findings, which probed the structure of the  $\text{Fe}(\text{CO})_4$  10 ps after photoexcitation to be similar to an  $\text{Fe}(\text{CO})_5$  missing one equatorial ligand.<sup>(92)</sup> However, the dissociation happens on the timescale of 100 femtoseconds, leaving several picoseconds for structural reorganization. Already during the longest simulation that resulted in the dissociation of an axial carbonyl<sup>7</sup>, significant reorganization occurred (see Figure 6 for a comparison of the start and end geometry), leading to bond angles close to those of the  $\text{Fe}(\text{CO})_4$  singlet ground state. However, for the simulation of the full reorganization longer simulation times would be needed. All of the afore-mentioned structures are shown in Figure 6.

<sup>7</sup> Simulation time for that trajectory was 390 fs.

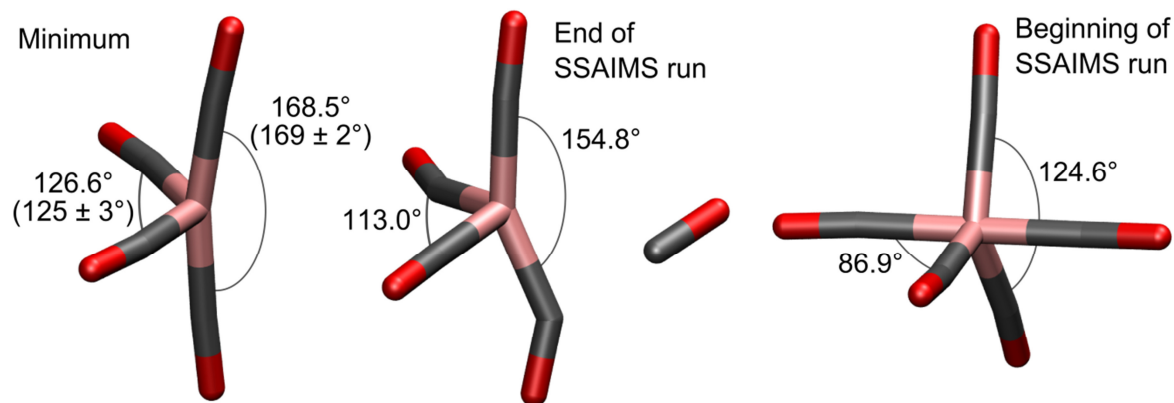
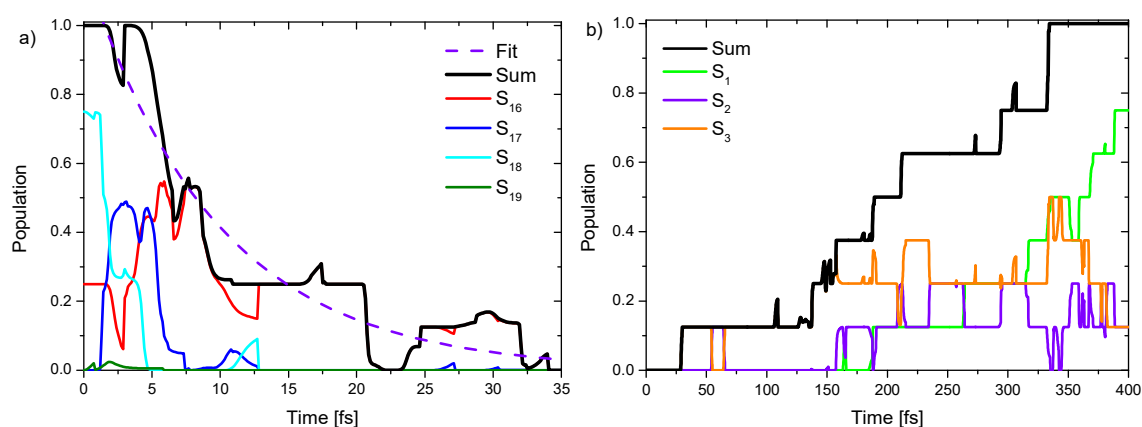


Figure 6: Left: Optimized  $S_0$ -structure of  $\text{Fe}(\text{CO})_4$  as calculated with  $\omega\text{PBE}/\text{lanl2dz}$ ,  $\omega=0.35 \text{ a.u.}^{-1}$ . Experimental values(92) are given in parenthesis, which agree perfectly with the shown computed structures. Middle:  $\text{Fe}(\text{CO})_5$  structure at the end of one SSAIMS/TDDFT run (after 392 fs) with the bond angles corresponding to the  $\text{Fe}(\text{CO})_4$  structure. Right:  $\text{Fe}(\text{CO})_5$  structure at the beginning of one SSAIMS/TDDFT run with the bond angles corresponding to the  $\text{Fe}(\text{CO})_4$  structure.

#### *Dynamics after excitation at the shoulder at around 5 eV*

The experimental excitation at 4.66 eV(91) and 5.00 eV(90) was simulated by projection of the ground-state wave function onto the PES of  $S_{16}$  to  $S_{19}$ , which are of MLCT character. Four initial conditions were chosen and calculated, each with two different random number seeds for the stochastic selection algorithm, resulting in a total of eight runs. Similar to the dynamics calculations detailed before, the dissociation happens only when one of the three energetically lowest singlet states is populated. In contrast to the results discussed before, five out of eight runs show equatorial dissociation, following a mechanism similar to the one deduced from transient femtosecond pump-probe photoionization mass spectra.(91) In the beginning of the dynamics, the Fe-C bonds of two or three equatorial ligands stretch. This is due to the increased electron density in the equatorial plane of the initially excited MLCT states compared to the ground state. As shown in Figure 7 a), the population of these states decays very fast within 35 fs to zero. An exponential fit of the population decay yields a lifetime of 10 fs. This is in the same order of magnitude as the experimentally derived 21 fs for this process(91). It has to be noted that the calculated time constant of 10 fs has a high error because of the

low number of runs<sup>8</sup>. To increase the statistical significance of the calculation, more runs would be needed.



**Figure 7:** Population changes of singlet excited states a)  $S_{16}$  to  $S_{19}$  during the first 35 fs and b)  $S_1$  to  $S_3$  during the first 400 fs of the SSAIMS-dynamics averaged over all TBFs. The sum of the populations of the states, which are shown, is also given. For a), the sum was fitted with an exponential function:  $y=e^{-(t-t_0)/\tau}$ . Fit parameters are:  $t_0=1.5$  fs,  $\tau=9.6$  fs.

The depopulation of the bright MLCT state is followed by internal conversion *via* twelve intermediate states, *i.e.*  $S_4$  to  $S_{15}$ , to the states  $S_1$ ,  $S_2$  and  $S_3$  (see Figure 22 to Figure 24 in the appendix for details on population changes of  $S_4$  to  $S_{15}$ ). It has been proposed in reference (91) that the Fe-C bond lengths stretch and shorten while going to the lower lying states. This is also observed in the calculated dynamics, as can be seen in Figure 8.

The population transfer to the low-energy states, *i.e.*  $S_1$ ,  $S_2$  and  $S_3$ , starts 28 fs after excitation and all population has been transferred to these three states after 335 fs, see Figure 7 b). From the experimental results in combination with calculations(91), it was concluded that the dissociation happens with a time constant below 100 fs. However, the fastest dissociation seen in the SSAIMS runs happened after 180 fs (see Figure 8). In the time before dissociation, Fe(CO)<sub>5</sub> undergoes on average two vibrations of the Fe-C stretching mode (period of about 100 fs(102)). The dissociation mechanism derived experimentally also involves this stretching and shorting of the Fe-C bond length before dissociation.(91) However, it is unlikely that these expansions and contractions occur on a time scale shorter than the actual period of one Fe-C stretch vibration. Analogous to

<sup>8</sup> Each of the four curves whose sum is fitted exponentially (population of the singlet states  $S_{16}$  to  $S_{19}$ ) has an absolute error of up to 0.19, based on the averaging over the SSAIMS runs. The error of the exponential fit was  $\pm 0.07$  fs.

these results, a longer lifetime for internal conversion was obtained with TDDFT compared to the experimental findings for the similar compound Cr(CO)<sub>6</sub>.(30) However, it was shown that this is not a deficiency of TDDFT as similar time constants to the TDDFT results were obtained with CASSCF.(30) Furthermore, the PES for the accurate multi-reference configuration interaction (MRCI) is estimated to give lifetimes even longer than TDDFT.(30) Therefore, it was hypothesized that the experimental analysis leads to an underestimation of the internal conversion time.(30) After all, for Fe(CO)<sub>5</sub> the assignment of the experimental lifetimes to specific processes is based on stationary calculations and leaves room for interpretation.

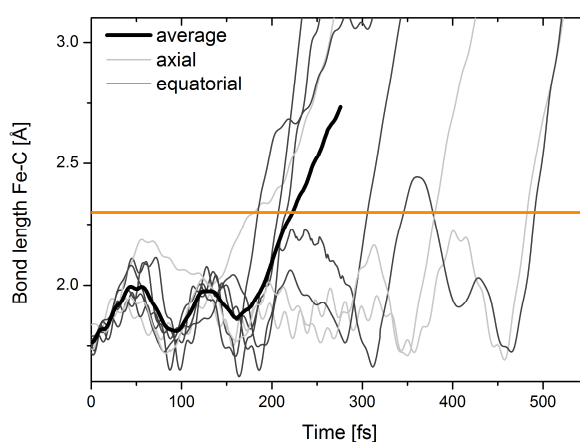


**Figure 8:** Time evolution of the dissociating Fe-C bond lengths during the dynamics including 20 excited states for all eight SSAIMS runs and their average (thick black line). Light gray and dark gray lines are the SSAIMS runs, which ended in the dissociation of an axial and an equatorial carbonyl ligand, respectively. The orange line marks the dissociation bond length of 2.3 Å. The average (thick black line) reaches the dissociating bond-length at 223 fs.

In summary, the calculated dynamics are in agreement with most of the experimental results. No contradiction to the experiments of Ihee *et al.*(92) concerning axial or equatorial dissociation was found. Furthermore, a mechanism similar to the one detailed in reference (91) was found with rather good agreement of the first time constant in the order of ten femtoseconds. However, there are differences between the here-calculated time constant of the following process, *i.e.* an internal conversion, and the one assigned based on experiment and stationary point calculations(91). Therefore, in the following, the quality of the TDDFT results should be investigated further by comparison to CASPT2 calculations in order to check for deficiencies to describe double excitation character.

### 3.2.3 Comparison of TDDFT and CASPT2

The comparison between TDDFT and CASPT2 is done for scans of the PES interpolated in internal coordinates between the start and end points of two SSAIMS/TDDFT runs; one showing axial dissociation and the other equatorial dissociation. As has been detailed in the last section, the CASPT2 orbitals are based on a state-averaging procedure. Therefore, inaccuracies can rise, when averaging over many states with different character. To avoid such inaccuracies, in the following, eight states<sup>9</sup> are included in the CASPT2 calculations, as the TDDFT calculation in the Franck-Condon region shows that the seven lowest excited states are of similar character. Also the literature CASSCF calculations show seven low lying excited states with the same character(96).

#### *Comparison for PES along axial dissociation*

For both CASPT2 and TDDFT, the ground-state potential increases with increasing bond length of one coordinative bond to one axial carbonyl, see Figure 9. This is the expected behavior, as the calculations start in the Franck-Condon region, where the ground-state energy is minimal. CASPT2 has a shallow dip before it also starts rising. This indicates a higher equilibrium bond length for this method than for TDDFT, which occurs as the underlying PES are based on the TDDFT dynamics. It has to be noted that, for the TDDFT calculations at bond lengths above 2.7 Å, the ground state and the first excited state are so close in energy that one should not trust the results anymore because both states are calculated on different footing, as has been mentioned in section 3.1.

Three groups of excited states can be distinguished in the CASPT2 calculated PES. The low energy states  $S_1$  to  $S_4$  are quickly decreasing in energy close to the Franck-Condon region and then reach a plateau at a bond length longer than 2.4 Å (see orange marked states in Figure 9). In the TDDFT calculated PES, a corresponding group of states with lower slope at short bond lengths can be found.

The second group of states, highlighted in blue for both TDDFT and CASPT2, contains the low-energy states with oscillator strength greater than 0, marked as intense by the filled circles in Figure 9. This group of states has a shallow minimum before rising in energy.

---

<sup>9</sup> Seven excited states and the ground state

Because of the increased energy, these states are not among the lowest eight states and are therefore not calculated anymore for CASPT2 for long bond lengths. Instead, in the CASPT2 calculations, a third group of states arises, which is marked in purple. These states decrease in energies and show significant double excitation character. In the TDDFT calculations, double excitation character cannot be described. Therefore, the purple group cannot be found in the TDDFT calculations.

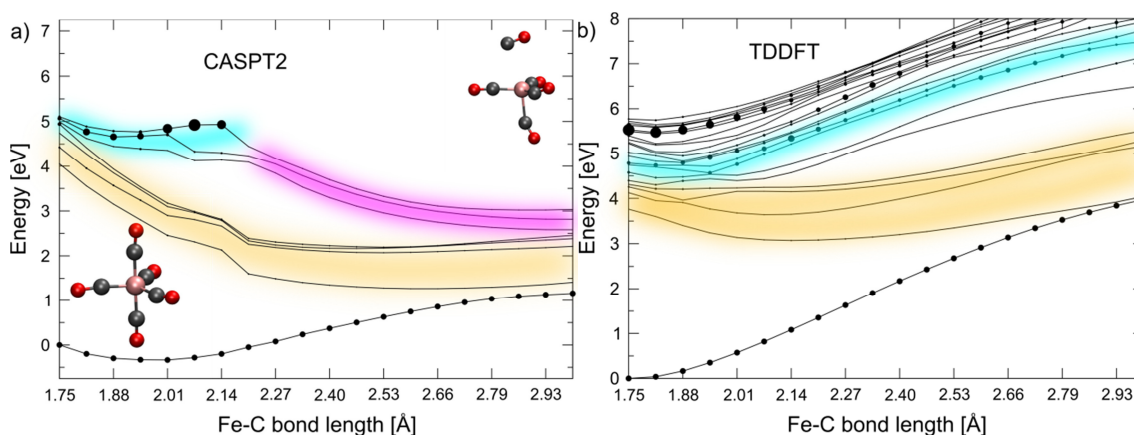


**Figure 9:** Comparison of the PES of the excited states of Fe(CO)<sub>5</sub> for a) CASPT2 and b) TDDFT for interpolated geometries between the start and end geometries of one SSAIMS/TDDFT run. The interpolation was done in internal coordinates and for a run that ended in the dissociation of an axial carbonyl, as visualized by the insets in a), which show the start and end geometry of PES. On the x-axis, the change in the coordinative bond length of the Fe to the dissociating carbonyl ligand is marked even though the other internal coordinates are also changing. CASPT2 calculations included eight states. For the TDDFT calculation, the twenty lowest lying excited singlet states and the ground state are shown. The radius of the filled circles along the curves scales with the oscillator strength of the respective excited state. For the ground state, filled circles have been added to highlight the raster of computations along the PES. TDDFT curves were calculated with TeraChem. CASPT2 curves were calculated with Molcas version 8.0. Groups of states with similar behavior are highlighted with colored background. MC states with decreasing and increasing energy are shown in orange and blue, respectively. Double excited states are highlighted in purple.

#### *Comparison for PES along equatorial dissociation*

For the dissociation of an equatorial carbonyl, basically similar PES are obtained and similar groups are found in comparison to the axial dissociation. For both CASPT2 and TDDFT, the group of low energy states, highlighted in orange, has a slower decrease in energy with increasing bond length, but does not reach a plateau. The higher energy states, highlighted in blue, are not increasing as much in energy as during the axial dissociation.

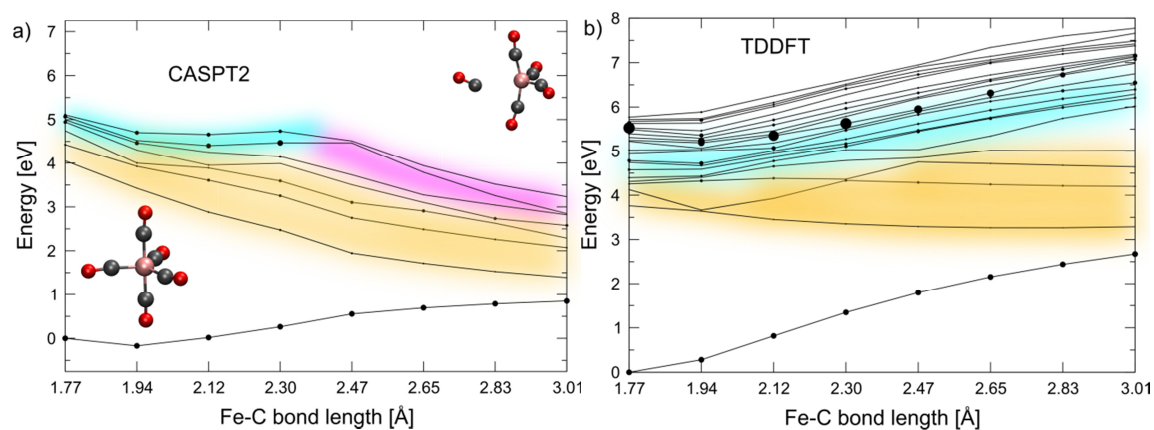


**Figure 10:** Comparison of the PES of the excited states of Fe(CO)<sub>5</sub> for a) CASPT2 and b) TDDFT for interpolated geometries between the start and end geometries of one SSAIMS/TDDFT run. The interpolation was done in internal coordinates and for a run that ended in the dissociation of an equatorial carbonyl ligand, as visualized by the insets in a), which show the start and end geometry of PES. On the x-axis, the change in the coordinative bond length of the Fe to the dissociating carbonyl ligand is marked even though the other internal coordinates are also changing. CASPT2 calculations included eight states. For the TDDFT calculation, the twenty lowest lying excited singlet states and the ground state are shown. The radius of the filled circles along the curves scales with the oscillator strength of the respective state. For the ground state, filled circles have been added to highlight the raster of computations along the PES. TDDFT curves were calculated with TeraChem. CASPT2 curves were calculated with Molcas version 8.0. Groups of states with similar behavior are highlighted with colored background. MC states with decreasing and increasing energy are shown in orange and blue, respectively. Double excited states are highlighted in purple.

### *Implication for the dynamics*

The most significant difference between CASPT2 and TDDFT is the occurrence of the states highlighted in purple. Population of these states could potentially also lead to dissociation, which was seen only for the orange states in the TDDFT dynamics simulations. This raises the question whether the observation that dissociation happens only in states  $S_1$  to  $S_3$  does hold true. The states with double excitation character are only low enough in energy to be populated by other states close to or after dissociation. However, the Fe-C bond lengths are only stretched thus far, when the population is already transferred to the states  $S_1$  to  $S_3$  and therefore the doubly excited states are not expected to be populated. However, this still has to be kept in mind during the analysis of the dynamics and therefore the TDDFT results should not be fully trusted for bond lengths much longer than the dissociation bond length.



Another difference between TDDFT and CASPT2 that could lead to misinterpretations when relying only on TDDFT results is the lower slope of the orange group especially for short bond lengths. The high slope of CASPT2 could lead to faster dissociation and therefore yield shorter time constants compared to TDDFT. However, in the SSAIMS/TDDFT runs, most of the time before dissociation is spent for internal conversion. Once the dissociation started, the carbonyl is ejected very fast in less than 50 fs for most of the calculations. Therefore, the influence on the total time constants is probably lower than the 50 fs ejection time.

All in all, general agreement between the TDDFT results and the experiment as well as the CASPT2 calculations was obtained for Fe(CO)<sub>5</sub>. The limits of TDDFT are revealed by the comparison to the CASPT2 PES. Even though the differences obtained for longer bond lengths probably do not influence the main characteristics of the calculated dynamics, the results for bond lengths longer than the dissociating bond length should be viewed critically. Thereby, it was shown, how TDDFT can be used to describe the dynamics of a transition metal complex with very complicated electronic structure and what limitations need to be taken into account during the evaluation. Based on the knowledge about TDDFT and despite its limits, the method is used in the following chapter for calculations of bigger transition metal complexes.

## 4 Photodynamics of transition metal complexes – Example Nickel porphyrinoids

In the previous chapters, SSAIMS/TDDFT was identified as a promising method for the simulation of the excited-state dynamics of transition metal complexes. Therefore, in this chapter, this combination of methods is applied to model the dynamics of big transition metal complexes in order to show the potential of the methods.

Among the transition metal complexes the metalloporphyrinoids are one prototype class of compounds, as they have versatile applications, such as photocatalysis(103), DSSCs(33), sensing(104) and two photon absorption(105, 106). Here, the focus lies on nickel porphyrinoids in particular as they show interesting and versatile photophysical properties(107), such as energy and charge transfer, internal conversion and intersystem crossing(108, 109). Furthermore, the short nickel nitrogen bond length has a strong influence on the nuclear conformation, which can impact the excited state deactivation processes.(110)

Two different nickelporphyrinoids have been investigated within this thesis: the first complex, nickel-tetramesityl-porphyrin (NiTMP), was chosen as it has been studied intensively by experimentalists(12, 108, 109, 111-114) and can therefore be used to evaluate the quality of the calculations (see section 4.1). The second complex nickel-methyl-3-devinyl-pyropheophorbide-a (NiDEPE) was selected, as it is experimentally fairly unexplored(115) and can be used to make predictions of the dynamics (see section 4.2).

### 4.1 NiTMP

Different experimental studies have detailed the excited-state deactivation of NiTMP as follows(12, 108, 109, 111-114): If the complex is excited in the Q-band, *i.e.* pumping a ligand-centered (LC) singlet excited state, this state has a very short lifetime close to the experimental time resolution in the range of a few hundred femtoseconds and is depopulated into an intermediate state with a lifetime in the order of magnitude of 1 ps. The intermediate state populates a metal-centered state, which has a longer lifetime of

a few hundred picoseconds.(12, 108, 109, 111-114) However, the character of the intermediate state is still under debate, and should be identified in this thesis.

To detail the excited-state dynamics of NiTMP, this chapter starts with a discussion of the absorption spectra of NiTMP to elucidate the excited states at the Franck-Condon point, which are of interest for the dynamics. A critical point analysis of NiTMP is then used to identify possible reaction intermediates and the influence of conformational changes on the population of the intermediates is discussed. Detailed insights are obtained by the calculated dynamics of NiTMP using SSAIMS and by a comparison of the results with experimental studies.

#### 4.1.1 Steady-state UV-vis absorption spectra

The absorption spectra of NiTMP (displayed in Figure 11) show two distinct peaks, which are typical for tetrapyrrole macrocycles. Both of these transitions are of  $\pi$ - $\pi^*$  character and can be explained by Goutermans four orbital model.(116-118) According to this model, there are only four orbitals involved in both transitions, the Gouterman orbitals, which are depicted in Figure 11 for NiTMP. The two unoccupied Gouterman orbitals are degenerate. The high energy peak, called Soret-band, lies at around 3 eV and involves transitions from HOMO-1 to both LUMOs. The low energy band between 2 and 2.5 eV is called Q-band and is composed of two degenerate transitions from HOMO to LUMO and LUMO+1.

The calculated absorptions peaks are higher in energy than the experimental ones, which is typical for TDDFT.(119) The intensity of the Q-band is underestimated by the TDDFT results, as this transition is symmetry-forbidden and only gains intensity *via* vibrational broadening.(116, 120)

In addition to the bands visible in the absorption spectra, there are transitions to five more states, which are of interest for the deactivation mechanism of NiTMP. These transitions are optically dark and energetically located within a range of 0.4 eV around the excitation energy of the Q-band at 2.3 eV. These states comprise two ligand-to-metal charge-transfer states (LMCT<sub>1</sub> and LMCT<sub>2</sub>) and three metal-centered states (MC<sub>1</sub>, MC<sub>2</sub> and MC<sub>3</sub>). Two of the MC states are degenerate (MC<sub>2</sub> and MC<sub>3</sub>). Such MC and LMCT

states have been reported before for nickel porphyrins with other substitution patterns.(121, 122) The transition energies to the seven lowest energy states and their character as quantified by charge difference densities(7, 123) are detailed in Table 3 and Figure 12.

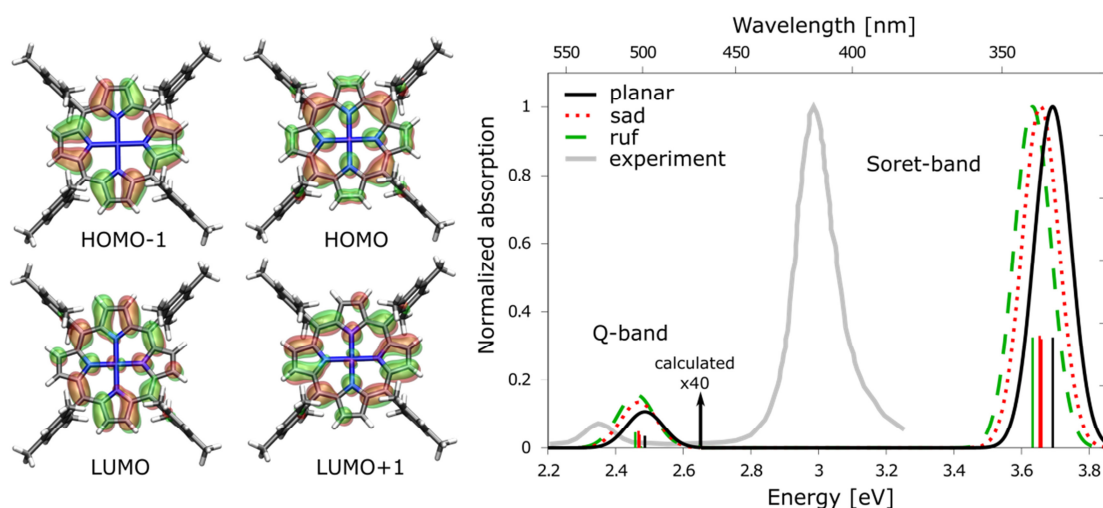


Figure 11: Left: HOMO-1, HOMO, LUMO and LUMO+1 of NiTMP calculated with  $\omega$ PBE,  $\omega=0.2 \text{ a}_B^{-1}$  plotted with an isovalue of  $0.02 \text{ electrons}/\text{\AA}^3$ . These orbitals correspond to the Gouterman orbitals. Right: Experimental(124) and calculated absorption spectra of NiTMP for different conformers. Q-band region of calculated spectra is enlarged by a factor of 40. All calculations were computed using ECPs(99) and the associated basis set lan12dz(100, 101) and the  $\omega$ PBE density functional employing an  $\omega$  of  $0.2 \text{ a}_B^{-1}$ .

Table 3: Electronic excitations for the planar NiTMP conformer.

State	Vertical absorption energy [eV]	Oscillator strength
LMCT <sub>1</sub> ( $\pi$ - $d_{x^2-y^2}$ )	2.14	0.0000
MC <sub>1</sub> ( $d_{z^2}$ - $d_{x^2-y^2}$ )	2.18	0.0000
MC <sub>2</sub> ( $d_{\pi}$ - $d_{x^2-y^2}$ )	2.32	0.0000
MC <sub>3</sub> ( $d_{\pi}$ - $d_{x^2-y^2}$ )	2.32	0.0000
LMCT <sub>2</sub> ( $\pi$ - $d_{x^2-y^2}$ )	2.43	0.0000
LC <sub>1</sub> ( $\pi$ - $\pi^*$ )	2.49	0.0039
LC <sub>2</sub> ( $\pi$ - $\pi^*$ )	2.49	0.0038

The absorption spectra of nickel porphyrins are in general influenced by the distortion of the porphyrin macrocycle.(125) As for NiTMP a number of different conformations can be present at room temperature(124), it is important to investigate the influence of these conformers on the spectra of NiTMP. Figure 11 shows only slightly varying absorption spectra, which are more red shifted for more out-of-plane distorted conformers

of NiTMP. This trend has also been found previously from experimental spectra of differently distorted porphyrins.(125)

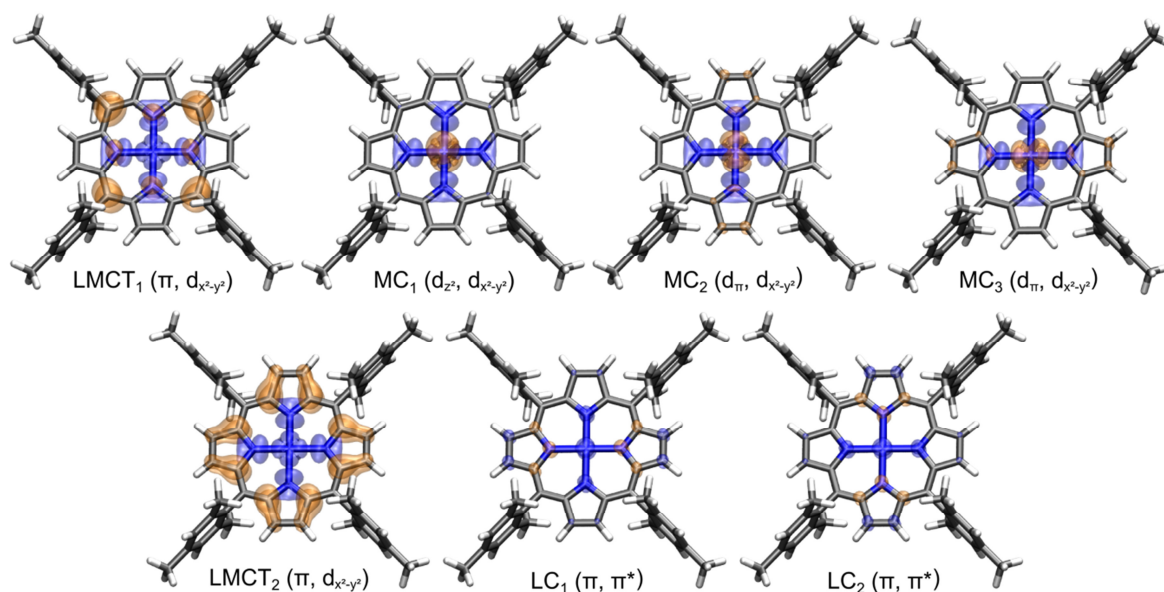


Figure 12: Charge difference densities of NiTMP transitions. Orange and blue regions mark electron depletion and accumulation, respectively. Isovalue:  $2.0 \cdot 10^{-5}$  electrons/ $\text{\AA}^3$ .

#### 4.1.2 Analysis of the singlet excited states at the critical points

Possible deactivation mechanisms after photoexcitation to the LC states are indicated by analysis of critical points. Figure 13 shows the energies for the seven lowest-energy states for specific critical points along the PES, *i.e.* energetic minima conformers for the different states and minimum-energy conical intersections (MECI). The optical excitation from the ground state into the LC state is marked by vertical arrows pointing to the energy of the LC state at the respective energetic minima conformers of the ground state. Starting from these states potential pathways are marked by the thick dot-dashed lines, which connect the energies of the states between different critical points. Critical points of interest for a pathway starting from the planar and ruffled conformer are indicated by a red and a blue background in Figure 13, respectively, whereas critical points that might be relevant for both pathways are highlighted with purple background.

In case of the *planar conformer* (see Figure 13, bottom middle), the LC-population can be transferred to the LMCT<sub>2</sub> state *via* the “MECI LC<sub>1</sub>/LMCT<sub>2</sub>” shown in Figure 13, which features a very similar geometry as the ground state and the LC state energetic minima. (Information about the characteristic bond lengths and angles of the critical point geometries can be found in Table

4.) However, the energetically most favorable geometry of the LMCT<sub>2</sub> state has significantly longer Ni-N bond lengths than the before mentioned states. This can lead to a temporary trapping of the population in this state, rendering it a candidate for an intermediate state debated in experimental research papers.<sup>(111, 112)</sup> Furthermore, the geometric optimization of the LMCT<sub>2</sub> state yields a strong shift to lower energies, thus resulting in a LMCT<sub>2</sub> state that is energetically even lower than the MC<sub>2</sub> and MC<sub>3</sub> states (see “Min LMCT<sub>2</sub>” in Figure 13). This switch in energetic order might imply that the MC<sub>2,3</sub> states are of only minor importance for the dynamics. However, a MECI to the MC<sub>1</sub> state (“MECI LMCT<sub>2</sub>/MC<sub>1</sub>” in Figure 13) can be found with similar excitation energy as “Min LMCT<sub>2</sub>”, which generally enables population transfer to the MC<sub>1</sub> state, which has the character of the long-lived state seen in the experiments.<sup>(12, 108, 109, 111-114)</sup>

**Table 4: Optimized geometric parameters (Å and deg) for the three ground state conformers, the excited states of interest and minimum energy conical intersections (MECI).**

State	Min GS sad	Min GS planar	Min planar LC <sub>1</sub>	MECI LC <sub>1</sub> /LMCT <sub>2</sub>	Min LMCT <sub>2</sub>
Ni-N <sub>p</sub> [Å]	1.95	1.96	1.97	1.97	2.01
N <sub>p</sub> -C <sub>α</sub> [Å]	1.40	1.40	1.40	1.41	1.39
C <sub>α</sub> -C <sub>β</sub> [Å]	1.45	1.45	1.45	1.45	1.48
C <sub>α</sub> -C <sub>m</sub> [Å]	1.40	1.39	1.40	1.40	1.41
C <sub>m</sub> -C <sub>TM</sub> [Å]	1.50	1.50	1.50	1.50	1.50
∠C <sub>α</sub> -N <sub>p</sub> -C <sub>α</sub> [deg]	104.6	104.3	104.3	104.1	105.5
∠C <sub>α</sub> -C <sub>m</sub> -C <sub>α</sub> [deg]	120.8	121.1	121.5	121.4	123.0

State	MECI LMCT <sub>2</sub> /MC <sub>1</sub>	Min GS ruf	Min ruf LC <sub>1</sub>	Min MC <sub>2</sub>
Ni-N <sub>p</sub> [Å]	2.01	1.94	1.95	2.02
N <sub>p</sub> -C <sub>α</sub> [Å]	1.39	1.40	1.40	1.40
C <sub>α</sub> -C <sub>β</sub> [Å]	1.49	1.45	1.45	1.46
C <sub>α</sub> -C <sub>m</sub> [Å]	1.41	1.40	1.40	1.40
C <sub>m</sub> -C <sub>TM</sub> [Å]	1.50	1.50	1.50	1.51
∠C <sub>α</sub> -N <sub>p</sub> -C <sub>α</sub> [deg]	105.5	105.1	105.1	105.9
∠C <sub>α</sub> -C <sub>m</sub> -C <sub>α</sub> [deg]	122.7	120.6	120.8	123.2

State	MECI MC <sub>2</sub> /MC <sub>1</sub>	Min MC <sub>1</sub>	MECI MC <sub>1</sub> /LMCT <sub>1</sub>	Min LMCT <sub>1</sub>
Ni-N <sub>p</sub> [Å]	2.01	2.03	2.02	2.03
N <sub>p</sub> -C <sub>α</sub> [Å]	1.41	1.40	1.40	1.39
C <sub>α</sub> -C <sub>β</sub> [Å]	1.45	1.46	1.46	1.46
C <sub>α</sub> -C <sub>m</sub> [Å]	1.40	1.41	1.40	1.41
C <sub>m</sub> -C <sub>TM</sub> [Å]	1.50	1.51	1.50	1.50
∠C <sub>α</sub> -N <sub>p</sub> -C <sub>α</sub> [deg]	105.5	106.1	106.9	105.3
∠C <sub>α</sub> -C <sub>m</sub> -C <sub>α</sub> [deg]	122.5	123.3	122.3	124.6

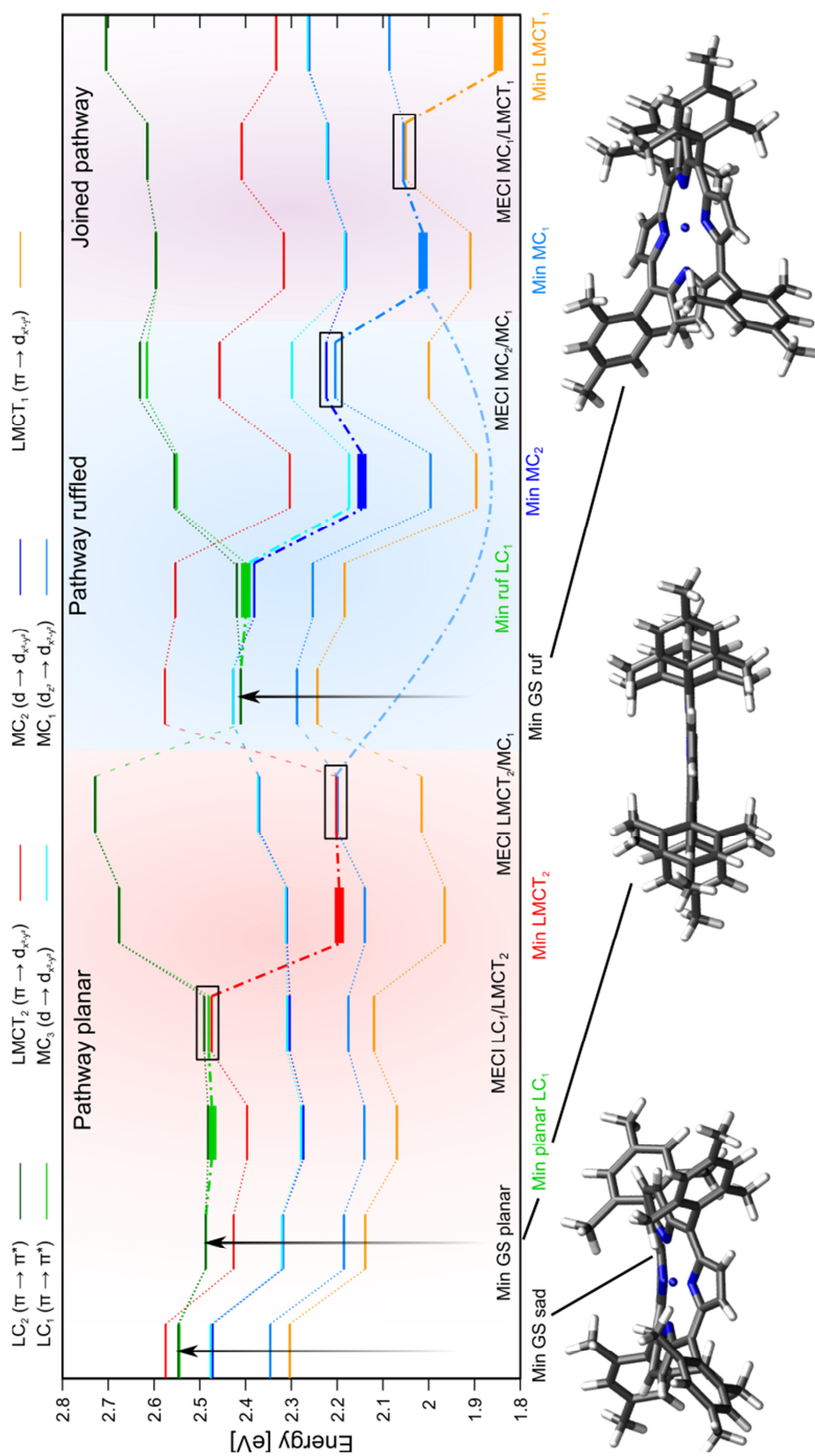


Figure 13: Electronic energies (reference is the ground state of the planar conformer) of the seven lowest lying excited singlet states at the critical points of the potential energy surface (PES) of NITMP. Dotted lines connect the energies of the states between different critical points. The ground state conformers are marked with arrows symbolizing the excitation into the LC states. Energetic minima (Min) of the excited states are highlighted by a broadened line for the respective state, whereas minimum energy conical intersections (MECI) are enclosed in black rectangles. Thick dot-dashed lines mark possible pathways. Dashed lines mark a break in the PES due to a new conformer. Critical points of interest for a pathway starting from the planar (ruffled) [both] conformer[s] have a red (blue) [purple] background.

Whereas the above discussed critical point path starting at the planar conformation might eventually hint to the LMCT<sub>2</sub> state being the intermediate state debated in experimental research papers(111, 112), this state is much higher in energy than the experimentally pumped LC states in case of the *ruffled conformer* (see Figure 13 bottom right) at its ground state geometry. Therefore, the LMCT<sub>2</sub> state is not expected to be involved in the deactivation mechanism of LC-excited ruffled conformers at all. Furthermore, the energetic order of the LC, MC<sub>2</sub> and MC<sub>3</sub> states are inversed at the ground state geometry of this ruffled conformer (“Min GS ruf” in Figure 13) in comparison to all other critical points, but they are still very close in energy. Because of this low energy difference, even at “Min ruf LC<sub>1</sub>”, rapid population transfer might happen from the LC<sub>1,2</sub> states to the MC<sub>2,3</sub> states. In contrast, fast depopulation of the MC<sub>2,3</sub> states into the MC<sub>1</sub> state has a low probability as these states have a large energetic difference of about 150 meV for almost all critical points. Therefore, the MC<sub>2,3</sub> states can be considered as intermediates, which is in accordance with experimental research papers.(108, 109) Nevertheless, a MECI between the MC<sub>2,3</sub> states and the MC<sub>1</sub> state was found (“MECI MC<sub>2</sub>/MC<sub>1</sub>” in Figure 13), which generally enables direct population transfer to the MC<sub>1</sub> state, which was identified as the long lived state by various experiments.(12, 108, 109, 111-114)

Finally, the critical point analysis highlights that two energetically fundamentally different LMCT states need to be considered when discussing the involvement of transient LMCT states before populating MC states as discussed by Shelby *et al.*(12) Whether the energetically higher LMCT<sub>2</sub> state needs to be actually considered depends on the conformer that is actually probed: For planar and saddled conformers this state is energetically close to the experimentally pumped LC states, while it is energetically separated considerably in case of the ruffled conformer. The second, energetically lower, LMCT<sub>1</sub> state is always expected to be involved in the excited-state dynamics, because it is the excited state of lowest energy at all investigated critical points. However, therefore, the LMCT<sub>1</sub> state might not be assigned to the intermediate between LC and MC excited states. Hence, in the following, the role of the LMCT<sub>2</sub> state is investigated. From the critical point picture of the “planar pathway” it might be deduced that the LMCT<sub>2</sub> state is a relevant intermediate for the LC<sub>1</sub> → MC<sub>1</sub> transition. However,



to quantify to which extend the LMCT<sub>2</sub> state, and any other state, is involved in the excited-state dynamics, nonadiabatic dynamics calculations were performed, thus also accounting for dynamic nuclear motion. In these calculations, the focus lies on the planar conformer, where it is expected that the LMCT<sub>2</sub> state has the highest probability of being significantly involved in the dynamics and which might be considered representative for the total set of possible conformers(110). Additionally, changes introduced to the dynamics when starting from a different conformer are qualified by calculating a few sample trajectories starting from the ruffled conformer. This is detailed at the end of the following subsection.

### 4.1.3 Dynamics calculation

The experimental Q-band excitation was modeled in the nonadiabatic dynamics simulation by a projection of the ground-state wave function onto the PES of the sixth singlet state S<sub>6</sub> (LC<sub>1</sub>), which is the energetically lowest state with significant oscillator strength. In order to identify the short-lived intermediate, which has not been clearly identified by experiments yet, the first 500 fs of the dynamics are simulated. Based on the shortest lifetime, which was deduced from experiments, it is expected that the population is transferred to this intermediate within the given simulation time(12).

To facilitate comparative tracking of the population changes between the different states with time, the population of energetically close states with similar character, namely LC<sub>1,2</sub> and MC<sub>2,3</sub>, were summed together and considered as a group. Intuitively, one might track the population of states according to their energetic order at the energetically most favorable geometry of the planar conformer, *i.e.* the Frack-Condon (FC) point, which is labelled “Min GS planar” in Figure 13: S<sub>6</sub> and S<sub>7</sub> would then be assigned as the LC states, whereas states S<sub>3</sub> and S<sub>4</sub> could be combined into the MC<sub>2,3</sub> states. This analysis is referred to as FC-analysis in the following. However, as shown in the last subsection, the ordering of the states depends heavily on the molecular geometry and will therefore change during the dynamics. Therefore, a second means of state tracking was introduced, which accounts for the character of the populated state *via* analysis of relative excitation energies (thus abbreviated as E<sub>rel</sub>-analysis in the following). In this E<sub>rel</sub>-analysis, the energetic relations between particular states is

utilized to account for the character of the states during the dynamics: The  $LC_{1,2}$  states as well as the  $MC_{2,3}$  states are degenerate over large ranges of the PES (*cf.* Figure 13). Thus, an algorithm was used to identify these two pairs of approximately degenerate states. Furthermore, the energetic difference between the  $MC_{2,3}$  and the  $MC_1$  state stays around 150 meV for all critical points shown in Figure 13 but the conical intersection between them. Therefore, this energy difference can be used to assign the  $MC_1$  state, leaving the remaining states to be of LMCT character. Only if all these requirements are fulfilled for a given time step of a trajectory, this time step will be included in the analysis. (See section 7.6 in the appendix for a detailed description of the algorithm.)

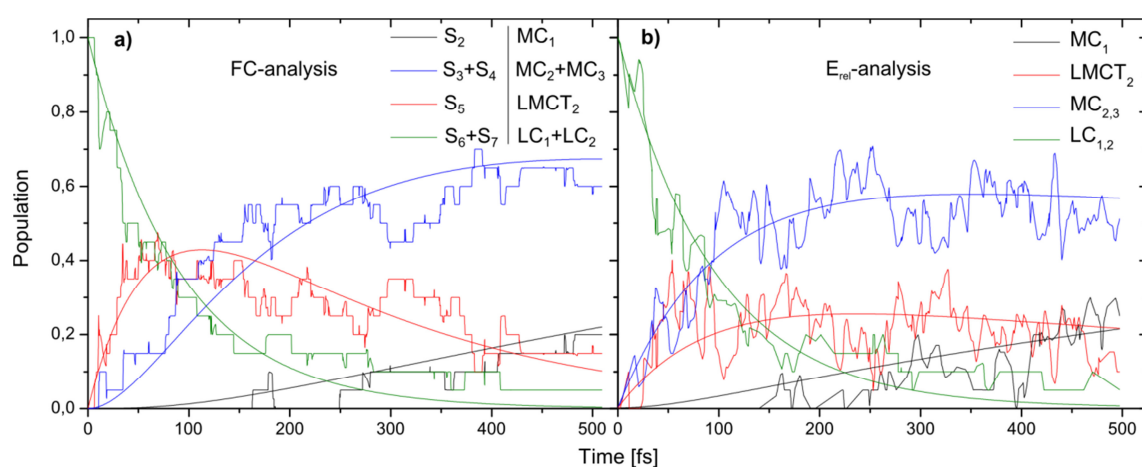


**Figure 14:** a) Population change of the singlet states during the dynamics averaged over 20 SSAIMS runs and a fit of the population decay. This includes the following grouping based on the ordering at the ground state conformer:  $S_6$  and  $S_7$  were grouped to  $LC_{1,2}$  states and the  $S_3$  and  $S_4$  states are grouped as  $MC_{2,3}$  states. b) Population change of states characterized based on energetic considerations as detailed in the main text.

As shown in Figure 14, both analyses of the dynamics calculations yield fast decaying LC-state populations (time constant  $\tau_{LC} \approx 100$  fs), slowly growing populations of the energetically lowest singlet excited state  $MC_1$ , and development of significant populations of both of the above discussed intermediate state  $MC_{2,3}$  and  $LMCT_2$  in less than 0.5 ps. The  $E_{rel}$ -analysis, which corrects for energetic state flipping as compared to the FC-analysis (*cf.* Figure 14 b) and a), respectively), reveals that the intermediates get populated equally fast within the first 100 fs to  $\approx 30\%$ . In the following, the  $LMCT_2$  state population slowly decays to  $\approx 20\%$  after 500 fs, whereas the joint populations of the  $MC_{2,3}$  states continuously rise to  $\geq 50\%$  within 200 fs and then are changing weakly ( $\approx 50\%$  at 500 fs).

To facilitate comparison of this computed excited-state dynamics with experimentally derived characteristics of this dynamics, a rough estimate of the lifetimes of the LMCT<sub>2</sub> and the MC<sub>2,3</sub> states was obtained by an exponential fit. For this analysis it was not possible to use a sequential model, as the LMCT<sub>2</sub> and the MC<sub>2,3</sub> states get populated simultaneously. Therefore, the following non-sequential model was used for the fit: the LC<sub>1,2</sub> states populate the LMCT<sub>2</sub> and the MC<sub>2,3</sub> states simultaneously with a portion of *A* being transferred to the LMCT<sub>2</sub> state and *(1-A)* being transferred to the MC<sub>2,3</sub> states. Both the LMCT<sub>2</sub> and the MC<sub>2,3</sub> states then populate the MC<sub>1</sub> state (see section 7.7 in the appendix for fit formulae). This fit yields a LMCT<sub>2</sub> lifetime of about 1 ps whereas the MC<sub>2,3</sub> states have a lifetime of over 3 ps (see Table 5). The thereby obtained reaction mechanism has been summarized in Figure 15. To test the robustness of the fitting-model the fit was repeated without consideration of the MC<sub>1</sub> state (see Table 5). This model includes less data, but does not assume that both intermediates are depopulated directly into the MC<sub>1</sub> state. Even if exclusion of the MC<sub>1</sub> state leads to overall slightly shorter lifetimes, both fits result in a portion of about 65% of the population being transferred to the MC<sub>2,3</sub> states and a more than three-fold longer lifetime for the MC<sub>2,3</sub> states than for the LMCT<sub>2</sub> state. Therefore, it can be concluded that the probability of experimental detection of the transient MC<sub>2,3</sub> states is larger than detecting the transient LMCT<sub>2</sub> state, if the experimental technique applied is equally sensitive to both states.

**Table 5: Fit of the population of states including or not including the MC<sub>1</sub> state.**

State	Life time $\tau$	
	Including LC <sub>1,2</sub> , LMCT <sub>2</sub> , MC <sub>2,3</sub> and MC <sub>1</sub>	Including only LC <sub>1,2</sub> , LMCT <sub>2</sub> and MC <sub>2,3</sub>
LC <sub>1,2</sub>	96.0 ± 0.4 fs	91.1 ± 0.4 fs
LMCT <sub>2</sub>	1.04 ± 0.03 ps	677 ± 15 fs
MC <sub>2,3</sub>	3.7 ± 0.2 ps	2.97 ± 0.14 ps

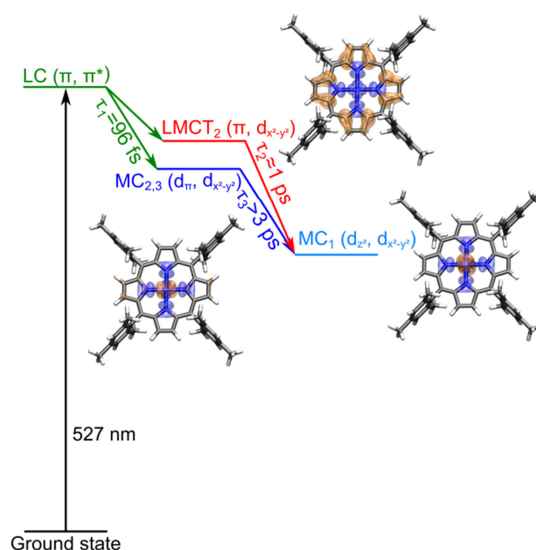


**Figure 15:** The decay mechanism is visualized including the lifetimes, as obtained by the non-sequential fit including the MC<sub>1</sub> population.

### *Influence of the conformer*

The analysis detailed above was started from the planar conformer. In order to characterize the changes introduced to the dynamics when starting from a different conformer, five sample runs starting from the ruffled conformer are calculated for 350 fs. Because of the lower number of runs, the average of the population for the ruffled conformer shows higher fluctuations than for the planar conformer. Hence, the population changes are compared only for states with significant population<sup>10</sup>, *i.e.* states S<sub>4</sub>, S<sub>5</sub> and S<sub>6</sub> (see Figure 16).

For the population of S<sub>6</sub> very similar behavior for the dynamics starting from both conformers can be seen. From Figure 16 upper panel, one would expect a similar time constant for the dynamics of the ruffled conformer as for the planar conformer, if the same number of runs, *i.e.* 20, was calculated. The population changes for S<sub>5</sub> and S<sub>4</sub> show more differences than seen for S<sub>6</sub>. However, this is mostly due to the lower number of runs. One example of a significant difference can be seen for the S<sub>5</sub> population between 50 and 60 fs. In this time regime, there are more than five runs with zero S<sub>5</sub> population for the planar conformer. Therefore, if only five runs per conformer were compared, a

<sup>10</sup> For the other states, the population is so low that when average over only five runs the signal-to-noise ratio is too low to conduct a meaningful comparison.

better agreement for this time range could be achieved. As detailed with this example, one can say that within the high statistical error of the calculation for the ruffled conformer, the population for  $S_5$  as well as  $S_4$  are in good agreement with those for the planar conformer.

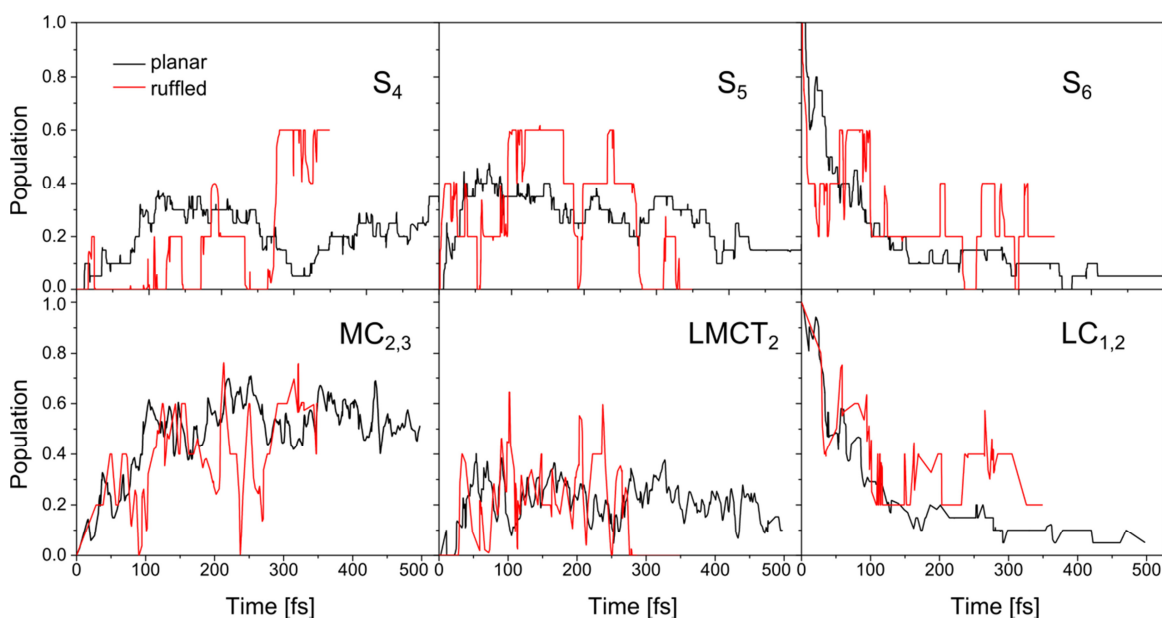


**Figure 16:** Comparison of the population change of the higher excited states for the dynamics starting from the ruffled and planar conformer. These have been averaged over 20 and 5 SSAIMS runs for the planar and ruffled conformer, respectively. Here the population changes of the states  $S_4$ ,  $S_5$  and  $S_6$  are displayed, as well as the changes for the  $LC_{1,2}$ ,  $LMCT_2$  and  $MC_{2,3}$  states in correspondence to Figure 14 b).

Additionally, the population changes as obtained by the  $E_{rel}$ -analysis are shown in Figure 16. This yields similar overall results as the comparison for  $S_4$ ,  $S_5$  and  $S_6$ . The increase in population for the  $MC_{2,3}$  and the  $LMCT_2$  state for the ruffled conformer are very similar to the one for the planar conformer, but again with a higher fluctuation, similar as has been the case for  $S_4$  and  $S_5$ . Thus, there is most likely only a minor influence of the starting conformer on the previously deduced deactivation mechanism. Hence, in the following the decay mechanism obtained based on the excited-state dynamics simulation is compared to the various experimental results, mentioned in the beginning of this section.

#### 4.1.4 Comparison to experiments

There have been several experimental studies on the ultrafast relaxation dynamics of NiTMP and similar compounds(12, 108, 109, 111-114). These show two ultrashort

lifetimes, one in the low hundreds of femtoseconds and one in the order of a few picoseconds, the former being very close to the instrument response time of the respective experiments. While the shortest lifetime is always assigned to the LC<sub>1,2</sub> states, different characters have been assigned to the second shortest lifetime, which was mostly based on exclusion of other states as potential intermediates as briefly outline in the following.

Two-pump–one-probe optical transient spectroscopy of nickel-tetraphenyl-porphyrin (NiTPP) previously suggested relaxation through an intermediate charge-transfer state with a lifetime of 4 ps<sup>(111)</sup>. However, in this study, the debated involvement of meta-stable MC states in the relaxation from the LC-states (excited at the second pump pulse) to the ground state is excluded by using the first pump pulse that already yields the long-living MC<sub>1</sub> state. In contrast, in previous pump-probe transient absorption measurements pumping the Q-band (the LC<sub>1,2</sub> states) of NiTPP, no indications of any charge-transfer state, which is expected to cause excited-state absorption features in the red spectral range<sup>(126, 127)</sup>, is observed within the initial 20 ps.<sup>(109)</sup> Instead, the dynamics within the first 20 ps after pumping, the LC-states are supposed to initially decay (after 350 fs) into a broad distribution of MC states that relaxes to a narrower distribution of MC states.<sup>(109)</sup> Following the latter work of Rodriguez and Holten<sup>(109)</sup>, Mizutani *et al.* assigned the signatures in their transient Raman spectra to the MC states and stated that these spectra gave no evidence for an additional excited state involved in the dynamics from the initially pumped LC to the relaxed MC states.<sup>(108)</sup> In a very recent study on NiTMP, Shelby *et al.*<sup>(12)</sup> probed optically dark states involving the 3d Nickel orbitals by means of transient X-ray absorption spectroscopy (XAS).<sup>(12)</sup> These investigations revealed two time constants, one below 300 fs and one of 1 ps, that are proposed to be of LC and LMCT character based on theoretically calculated XAS-signals<sup>11</sup>.

Corresponding to the experimental studies, our calculated 100 fs lifetime of the initially pumped LC<sub>1,2</sub> states fits to the very short experimental time constant <300 fs. The involvement of the transient broad MC manifold decaying within the first 20 ps

---

<sup>11</sup> The assignment which of the two lifetimes has to be assigned to which character is however not unambiguous.

discussed by Rodriguez and Holten(109) as well as by Mizutani *et al.*(108) might involve the longer-lived  $MC_{2,3}$  states identified in our work. The transient LMCT state identified in this work might be too weakly populated to be observable in these experimental pump-probe transient absorption measurements(109). However, an intermediate of this character was proposed by Shelby *et al.*(12) based on the calculated XAS signals for an LMCT states. To investigate whether MC states might be hidden alongside the LMCT state in the transient XAS data reported by Shelby *et al.*(12) I calculated the XAS signal of the MC state in addition to the reported XAS signal of the LMCT state(12) (see Figure 17, see section 7.8 in the appendix for details on the calculation). Both the calculated LMCT and MC show XAS peaks around 8337.5 eV close to the maximum of the peak of the transient intermediate seen in the experiment(12). As there is no isosbestic point in the experimental transient XAS spectra between the ground state bleach and the intermediate signal, I conclude, that the signals of the MC and LMCT states overlap to form this transient peak.

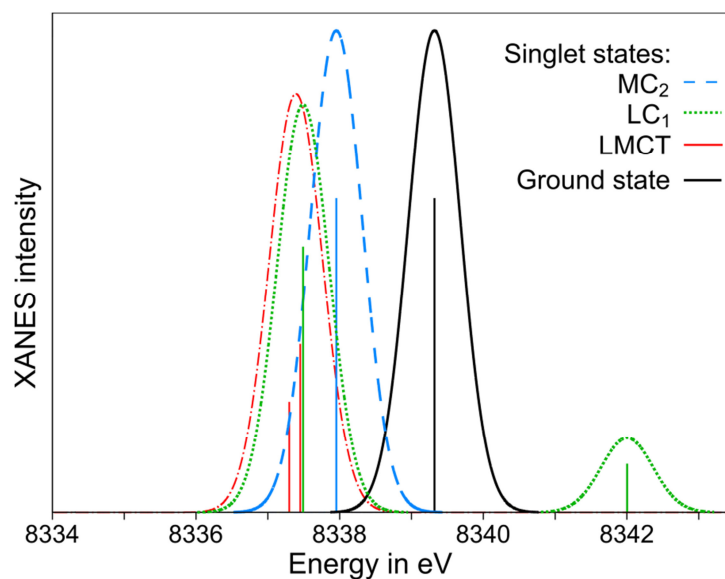


**Figure 17:** Calculated XANES spectra for the  $1s \rightarrow 4p_z$  energy region of the singlet states of interest. The spectra were calculated using Ahlrich's all-electron double zeta basis set(65) with polarization functions and were shifted by 67.2 eV in order to fit the experiment. The peak positions of the LMCT state were taken the literature.(12)

In summary, the *ab-initio* derived data is in agreement with all experimentally determined results, thus resolving the apparently contradicting findings on the involvement of LMCT or MC transient species between the initially pumped LC and the relaxed MC states. Hence, it was shown, how the methods selected in the previous chapters can be used to further detail the reaction mechanism of a big transition metal

complex. The  $E_{\text{rel}}$ -analysis represents a new strategy for the evaluation of the dynamics of transition metal complexes with complicated electronic structures, which might be adapted for future calculations of metal complexes. To the best of my knowledge, this is the first simulation of the excited-state dynamics of a transition metal complex with more than 100 atoms and 500 fs simulation time conducted up to date. It was thereby shown, that calculations of big transition metal complexes are nowadays feasible with the given methods.

## **4.2 NiDEPE**

It was shown above that the simulation of the ultrafast excited-state dynamics of even the extended transition metal complex NiTMP can be successfully performed to yield valuable atomistic insights and that those calculations can be considered computationally affordable with the combination of methods presented in this thesis. Therefore, this method combination might evolve to a routine technique for predicting so far unknown ultrafast excited-state dynamics for cases where TDDFT suffices for description of the electronic structure. One such example, which has structural similarity to NiTMP, but is less symmetric, is nickel-methyl-3-devinyl-pyropheophorbide-a (NiDEPE, inset of Figure 20). The corresponding  $\text{Mg}^{2+}$ -complex might be an intermediate during degradation of chlorophyll to chemically stable porphyrinoids(115, 128), and its excited-state dynamics, so far unknown to the best of our knowledge, will be predicted in the following.

### **4.2.1 Steady-state UV-vis absorption spectra**

NiDEPE has a significantly different absorption spectrum in comparison to NiTMP (see Figure 18). The transitions to the LC states, which constitute the Q-band, are not symmetry-forbidden for the asymmetric NiDEPE. Therefore, the Q-band shows a much higher intensity than in case of the rather symmetric NiTMP. Furthermore, the LC states are not degenerated in NiDEPE because of the molecular asymmetry. Our TDDFT-calculations (see Figure 18) show that the  $\text{LC}_1$  state is energetically significantly stabilized and finally has an even lower energy than the  $\text{MC}_2$  state at the Franck-Condon point. In addition, the  $\text{MC}_2$  and  $\text{MC}_3$  states are not degenerate as in case of NiTMP. Furthermore,



the LMCT<sub>2</sub> state is the lowest singlet state S<sub>1</sub> in NiDEPE, whereas it was S<sub>5</sub> for the planar NiTMP conformer.

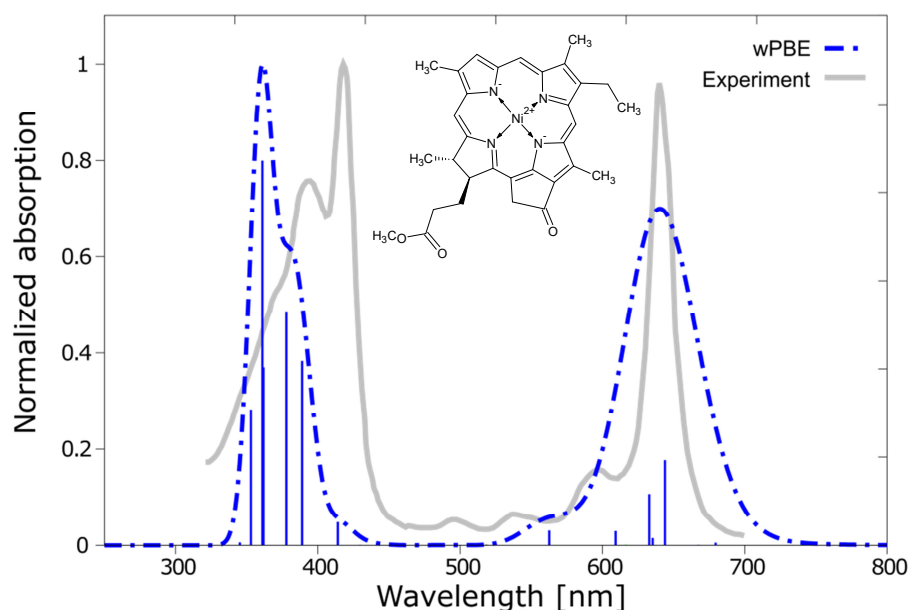


**Figure 18:** Experimental(115) and calculated absorption spectra of Ni-DEPE. Theoretical stick spectra are broadened with a Gaussian function with a width of 0.2 and shifted by 0.42 eV.

**Table 6:** Electronic excitations at the Franck-Condon point.

State	Vertical absorption energy [eV]	Oscillator strength
LMCT <sub>2</sub> ( $\pi$ - $d_{x^2-y^2}$ )	2.09	0.0004
MC <sub>1</sub> ( $d_{z^2}$ - $d_{x^2-y^2}$ )	2.24	0.0039
MC <sub>1</sub> ( $d_{z^2}$ - $d_{x^2-y^2}$ )/ LMCT <sub>1</sub> ( $\pi$ - $d_{x^2-y^2}$ )	2.28	0.0007
LC <sub>1</sub> ( $\pi$ - $\pi^*$ )	2.35	0.1223
MC <sub>2</sub> ( $d_{\pi}$ - $d_{x^2-y^2}$ )	2.37	0.0106
MLCT <sub>1</sub> ( $d_{\pi}$ - $\pi$ )	2.38	0.0739
MLCT <sub>2</sub> ( $d_{\pi}$ - $\pi$ )	2.46	0.0207
MC <sub>3</sub> ( $d_{\pi}$ - $d_{x^2-y^2}$ )	2.54	0.0004
LC <sub>2</sub> ( $\pi$ - $\pi^*$ )	2.62	0.0214

#### 4.2.2 Dynamics calculation

In the following, the first 500 fs of the nonadiabatic dynamics of NiDEPE including six singlet excited states are studied. To simulate the optical excitation, the ground-state wave function was projected onto the PES of the fourth singlet state, which is the state with the highest oscillator strength in the Q-band region. In order to analyze the data, one again needs to decide how to track the population of specific states. Because

NiDEPE shows less energetic state flipping than NiTMP, as revealed by the calculated energy levels at the critical points, see Figure 19, the straight forward FC-analysis introduced above appears to be sufficiently accurate for the population tracking of NiDEPE's excited states. The only relevant energetic state flipping involves the  $LC_1$  state ( $S_4$  at the Franck-Condon point) that switches with the  $MC_{2,3}$  states and becomes  $S_6$  at the other critical points. In order to account for this switching, both the  $LC_1$  state and the  $MC_{2,3}$  states are tracked together and assigned a single lifetime of 207 fs, see Figure 20. However, a consideration of the oscillator strengths can be used to compute the lifetime of the  $LC_1$  state alone, as it is the only bright state involved in the simulation (see Figure 21 for the change of averaged oscillator strength). This tracking yields a lifetime of the  $LC_1$  state lower than 10 fs. Therefore, one can conclude that the lifetime of the combined  $LC_1$  and  $MC_{2,3}$  states is mostly dominated by the  $MC_{2,3}$  states. The robustness of the fitting-model was tested by a repeated fit, which should yield the  $MC_{2,3}$  lifetime. For this purpose, the population of  $S_6$  was excluded from the fit, as for most conformations it has LC character. This second fit gave a time constant of 187 fs for the depopulation of  $MC_{2,3}$ , which differs only by 10 % from the 207 fs lifetime obtained before.

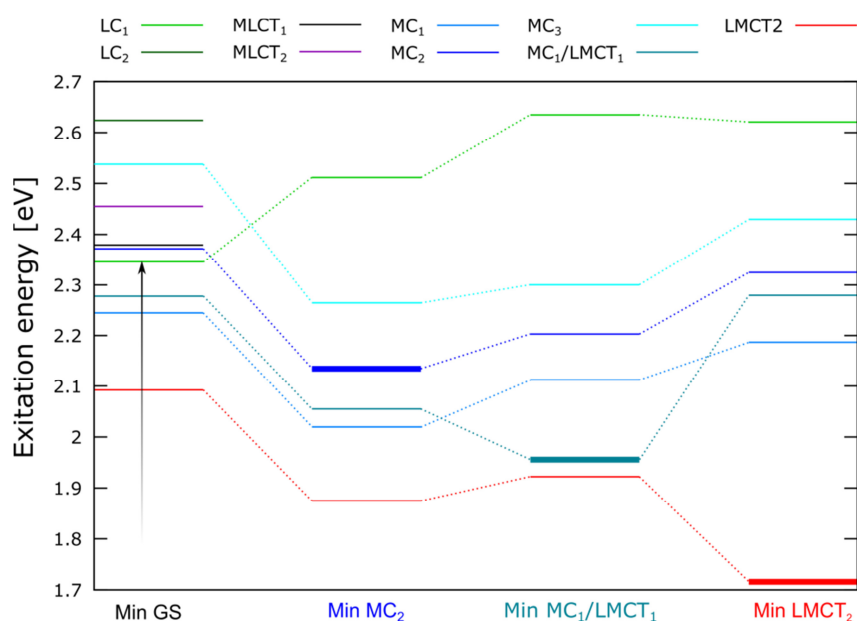
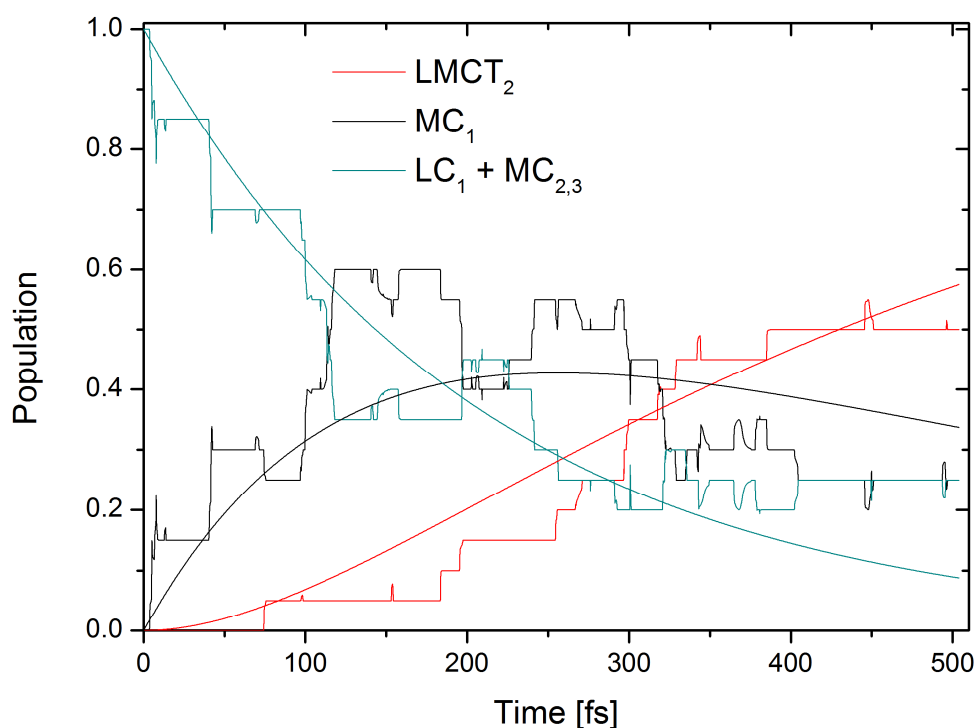


Figure 19: Electronic energies (reference is the ground-state of the planar conformer) of the six (nine) lowest lying excited singlet states at the energetic minima of the excited states (ground state) of NiDEPE. Dotted lines connect the energies of the states between different stationary points. The ground state minimum is marked with an arrow symbolizing the excitation into the  $LC_1$  state. Energetic minima (Min) of the excited states are highlighted by a broadened line for the respective state.

The deactivation continues by population transfer from the  $MC_{2,3}$  states into the  $MC_1$  state. The  $MC_1$  state populates the lowest lying  $LMCT_2$  state with a time constant of 506 fs. The general difference of the order of the states in NiDEPE compare to NiTMP leads to general changes in the dynamics. Whereas in NiTMP the  $LC_{1,2}$  states directly populated the  $LMCT_2$  state, the latter is the lowest energy state in NiDEPE and therefore is populated after the MC states. Furthermore, NiDEPE shows overall shorter time constants than NiTMP, which is visible for the  $LC_1$  state and the  $MC_{2,3}$  states that each have lifetimes one order of magnitude shorter for NiDEPE than for NiTMP (10 fs vs. 100 fs and 200 fs vs. >3 ps). This fact can be explained as the critical points of NiDEPE do not hint to trapping of population, as was the case for NiTMP.



**Figure 20:** Population change of the first five singlet states, which include the first LC state, the  $LMCT_2$  state and the MC states during the dynamics averaged over 20 AIMS runs and a fit of the population decay.  $S_4$  and  $S_5$  have been combined to LC (+MC) and  $S_2$  and  $S_3$  have been combined to the  $MC_1$  ( $d_{z^2} \rightarrow d_{x^2-y^2}$ ). Decay time for the combined  $S_4$ ,  $S_5$  and  $S_6$  is 207 fs and for  $S_2$  and  $S_3$  it is 506 fs. The inset shows the molecule NiDEPE.

In summary, the simulation of the first 500 fs of the excited-state dynamics of NiDEPE was predicted and compared to the dynamics of the more symmetric NiTMP. A sequential reaction mechanism with two time constants in the femtosecond range was found. This predictive simulation highlights the potential of SSAIMS/TDDFT for a routine application to transition metal complexes. With a total simulation time of about two

months using two GPUs per SSAIMS run, this investigation reaches efficiencies that would enable the preselection of target structures for specific applications before the elaborate synthesis, which might take more than two months to complete.

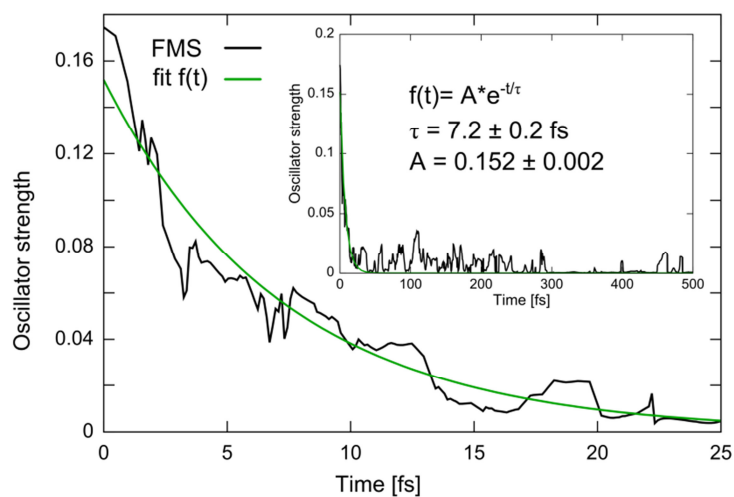


**Figure 21:** Change of the oscillator strength of the state with the highest population during the first 25 fs of the dynamics averaged over all runs. Inset shows an image of the whole dynamics. The fit formula and the parameters are given in the inset.

## 5 Conclusion

Computational chemistry, which arose as a new field only in the last century, has nowadays reached high importance, especially for physical chemistry. In this field, the simulation of a great variety of steady-state spectra has become a routine task, while the modelling of ultrafast processes like photochemical reactions is still very demanding. Therefore, simulations of such processes have been focused mostly on small to medium-sized organic molecules. However, for various applications like DNA intercalation, cancer theranostics and photocatalysis, big transition metal complexes are a much more promising choice to study than small organic molecules. Simulation of such big compounds has come into reach recently driven by the exponential growth of computational power available. However, the calculation of metal complexes poses several challenges to quantum chemical methods. (i) For big metal complexes with more than 100 atoms, a huge number of degrees of freedom have to be simulated. (ii) The unfilled d-shells of transition metals cause a high number and density of states. For these energetically close lying states, a higher number of interactions than for organic molecules is expected and has to be modeled.

The aim of this thesis was to meet the challenges posed by the simulation of photochemical processes of transition metal complexes. This was achieved by identifying suitable methods for the description of the nuclei as well as the electrons of the metal complexes, and the validation of the findings for a big transition metal complex. Furthermore, the potential of the methods was demonstrated by predicting the dynamics for a nickel-porphyrin.

For the description of the dynamics of the nuclei of big metal complexes with more than 100 atoms, a method is needed which allows for the calculation of more than 300 nuclear degrees of freedom. Full quantum mechanical treatment or other grid-based methods, like MCTDH, cannot be considered for this task because of their high computational cost. A more suitable choice is a trajectory-based approach. Two such methods have been compared over the course of this thesis: (i) The easily evaluable fewest switching surface hopping (FSSH), which treats the nuclei as a swarm of fully classical trajectories. Thus, it cannot describe some of the nuclear quantum effects

correctly, which is why several extensions of this method have been proposed. (ii) The *ab-initio* multiple spawning (AIMS) method employs a semiclassical treatment of the nuclei and can describe the nuclear quantum effects to sufficient accuracy. In the context of this thesis, the correct quantum-mechanical description of the decoherence effect of the nuclei is of special importance. In chapter 2, a comparison between FSSH and AIMS demonstrates the deficiencies of FSSH to describe this effect, which presented as a more than seven times shorter lifetime for FSSH than for AIMS. This comparison was done exemplarily for an organic molecule. However, decoherence is even more important for transition metal complexes than for organic molecules, because of the more complicated PES and the higher density of the states.

After a method for the description of the nuclei was identified, a method for the description of the electrons needs to be found. Here, a compromise between accuracy and computational cost is important, as on the one hand the electronic structure has to be evaluated at least once per time step and trajectory during the dynamics. On the other hand, the main features of the PES need to be described correctly to ensure valid overall results. Time-dependent density functional theory (TDDFT) is a promising candidate for this task, as it can achieve a good balance between accuracy and computational cost. However, it is known that TDDFT has problems describing charge-transfer states and doubly excited states. In chapter 3, it was shown for  $\text{Fe}(\text{CO})_5$  that charge-transfer states could be modeled well with a wisely chosen density functional. Furthermore, the limitations of TDDFT were elucidated by a comparison to CASPT2. According to CASPT2, doubly excited states come into play at higher dissociating bond lengths, which are not present in the TDDFT simulations. Therefore, care has to be taken when dissociations or other processes with greatly elongated bond lengths are simulated. Paying attention to these limitations, TDDFT can be used to model the dynamics of big transition metal complexes. A particularly efficient implementation of TDDFT on graphics cards can lower the computational cost even further by several orders of magnitude compared to CPU-implementations as has been shown for stationary point calculations. Thus, the simulation of huge metal complexes greatly benefitted from the combination of the GPU-based program TeraChem with the FMS90

software, which I implemented as part of this thesis and used for the calculation of all metal complexes herein.

The combination of methods mentioned before made the calculation of the big metal complex nickel-tetramesityl-porphyrin (NiTMP) possible. To the best of my knowledge, this is the first calculation to be done to date for a transition metal complex with over 100 atoms and a simulation time of 500 fs. With a calculation time of about 6 months<sup>12</sup> for the dynamics starting from one conformer, such calculations are now within reach for more routine studies of metal complexes.

In case of NiTMP, the experimentally determined excited-state dynamics involve excitations to ligand-centered (LC) states, *i.e.* essentially ( $\pi, \pi^*$ )-excitations giving rise to the well-known Q-band, that are depopulated with a time constant of smaller than 0.6 ps, as independently determined by different research groups and approximately reproduced by the AIMS/TDDFT simulations ( $\tau_{LC}=100$  fs). The excited state that is populated eventually is a metal-centered triplet (MC) state that has a characteristic lifetime of several hundreds of picoseconds as also determined independently by these research groups. The decay of that final electronic state can inherently not be described by means of AIMS/TDDFT as TDDFT within the approximation used cannot describe nonadiabatic couplings between the electronic ground state and the first excited one. However, this lifetime has been identified without doubt in the literature, whereas the essential question still under debate is the involvement of excited states between the initial LC-excitation and the final population of the triplet MC excited state. As revealed by my AIMS/TDDFT calculations, the initially pumped LC states get depopulated while a ligand-to-metal charge-transfer (LMCT) state and two MC states get populated quickly within 200 fs. These results clearly show that both intermediates get populated with approximately the same speed but the MC-populations clearly exceed the one of the LMCT state by a factor of two. This quantification of the involvement of both transient states now enables an in-depth interpretation of the seemingly contradicting experimental results reported in the literature. All experimental findings can be explained within the model derived here. Some experiments show only one of the

---

<sup>12</sup> Using two GPUs per AIMS run.

intermediates because of the limit in time resolution. The latest transient X-ray absorption experiments show two intermediate peaks with similar lifetimes, as can be inferred from the lack of an isosbestic point.

As mentioned above, the AIMS/TDDFT combination was applied to predict the excited-state dynamics of nickel-methyl-3-devinyl-pyropheophorbide-a (NiDEPE). For this complex, the break in the symmetry complicates the description of the excited-state characters as compared to NiTMP. However, I was able to propose the following reaction mechanism: The excited LC state populates a MC state with a time constant of less than 10 fs. This state then depopulates into another MC state with a time constant of 200 fs, which is depopulated into a LMCT state with a time constant of 500 fs. In contrast to NiTMP, this is a sequential decay mechanism, which happens on faster time scales. This simulation is the first one to predict the ultrafast dynamics of a transition metal complex, therefore highlighting the potential for routine application of these methods.

In summary, in this thesis, AIMS was selected for the description of transition metal complexes, as it was shown to yield better lifetimes for excited states than FSSH. Furthermore, TDDFT in its GPU-implementation has been selected as the electronic structure method most appropriate for the simulation of big transition metal complexes with ten or more excited states of interest and for timescales of several hundreds of femtoseconds. The selected methods have been applied in the biggest calculation done up to now on NiTMP, a transition metal complex with more than 100 atoms. The methods were validated to work for big transition metal complexes with a comparison to experimental results and the dynamics of NiTMP is further elucidated. These new findings on the dynamics of NiTMP illustrate that AIMS/TDDFT is capable of answering open research questions about the ultrashort time scale of the excited-state dynamics of transition metal complexes. Additional simulations of the rather unexplored NiDEPE further highlight how the methods can be applied without *a priori* knowledge about the excited-state dynamics. Therefore, the simulations detailed in this thesis lay the foundation of further investigations of the dynamics of transition metal complexes by highlighting the advantages but also the limitations of AIMS and TDDFT and by further demonstrating strategies for the evaluation of the dynamics of a high number of



excited states. This will be further aided by the growth in computational power available, which will make calculation of even longer time scales than 500 fs possible. Thus, the simulation of time constants in the low picosecond range will soon come into reach for big transition metal complexes. With such efficient computational methods at hand, the preselection of synthetic target structures comes into reach as computational preselection gets less time-consuming than the actual synthesis and experimental characterization.

## 6 Zusammenfassung

Das im letzten Jahrhundert neu aufgekommene Forschungsgebiet der Quantenchemie, hat gegenwärtig eine hohe Bedeutung insbesondere für die physikalische Chemie. In diesem Gebiet ist die Berechnung von Gleichgewichtsspektren zu einer Routineaufgabe geworden, wohingegen die Modellierung von ultraschnellen Prozessen wie photochemischen Reaktionen noch heute sehr anspruchsvoll ist. Daher wurden solche Prozesse bisher vorrangig für kleine bis mittelgroße organische Moleküle simuliert. Für viele Anwendungen wie DNS-Einlagerung, Krebstheranostik und Photokatalyse ist es jedoch vielversprechender große Übergangsmetallkomplexe zu untersuchen. Die Simulation solch großer Verbindungen ist jüngst durch den exponentiellen Anstieg der Rechenleistung möglich geworden. Die Berechnung von Übergangsmetallkomplexen stellt jedoch einige Herausforderungen an die quantenmechanischen Methoden. (i) Für große Metallkomplexe mit mehr als 100 Atomen muss eine immense Zahl an Freiheitsgraden simuliert werden. (ii) Die ungefüllten d-Schalen der Übergangsmetalle führen zu einer hohen Anzahl und Dichte von elektronischen Zuständen. Für diese energetisch sehr ähnlichen Zustände sind mehr Wechselwirkungen zu erwarten und müssen demnach auch simuliert werden.

Das Ziel der Promotion war es, die Herausforderungen zu meistern, die die Simulation der photochemischen Prozesse von Übergangsmetallkomplexen an quantenchemischen Methoden stellen. Dies wurde erreicht durch die Identifikation geeigneter Methoden für die Beschreibung sowohl der Atomkerne als auch der Elektronen von Metallkomplexen und durch die Validierung der Methoden für einen großen Metallkomplex. Des Weiteren wurde das Potential der Methoden durch die Vorhersage der Dynamik eines Nickelporphyrins demonstriert.

Zur Beschreibung der Dynamik der Kerne eines großen Metallkomplexes mit mehr als 100 Atomen wird eine Methode benötigt mit der mehr als 300 nukleare Freiheitsgrade berechnet werden können. Die komplett quantenmechanische Beschreibung oder andere Gitter-basierte Methoden, wie MCTDH (engl. für *multi-configurational time-dependent Hartree*), kommen aufgrund ihres hohen Rechenaufwands nicht in Frage. Eine bessere Wahl dafür sind Trajektorien basierte Methoden, von denen zwei im

Rahmen dieser Promotion verglichen wurden: (i) Das einfach auszuwertende FSSH (engl. für *fewest switching surface hopping*) beschreibt die Atomkerne durch einen Schwarm von komplett klassischen Trajektorien. Daher kann es einige nukleare quantenmechanische Effekte nicht korrekt modellieren, weshalb Erweiterungen zu dieser Methode entwickelt werden. (ii) Das AIMS (engl. für *ab-initio multiple spawning*) behandelt die Kerne semiklassisch und kann daher nukleare quantenmechanische Effekte mit ausreichender Genauigkeit beschreiben. Im Kontext dieser Arbeit ist die korrekte quantenmechanische Beschreibung des Dekohärenzeffektes der Kerne von besonderer Wichtigkeit. Im zweiten Kapitel wurden durch einen Vergleich zwischen FSSH und AIMS die Defizite von FSSH bei der Beschreibung dieses Effektes gezeigt, welche sich in einer siebenmal kürzeren Lebenszeit für FSSH als für AIMS äußern. Dieser Vergleich wurde am Beispiel eines organischen Moleküls durchgeführt. Die Dekohärenz ist jedoch von noch größerer Bedeutung für Übergangsmetallkomplexe als für organische Moleküle, da diese kompliziertere Potentialflächen und eine höhere Zustandsdichte besitzen.

Nach der Identifizierung einer Methode zur Beschreibung der Atomkerne, wird nun auch eine Methode benötigt mit der die Elektronen beschrieben werden können. Dabei ist ein Kompromiss zwischen Genauigkeit und Rechenaufwand sehr wichtig, da zum Einen die elektronische Struktur mindestens einmal pro Zeitschritt und Trajektorie berechnet werden muss. Zum Anderen müssen die Hauptmerkmale der Potentialflächen korrekt beschrieben werden, um die Zuverlässigkeit der Ergebnisse sicherzustellen. Zeitabhängige Dichtefunktionaltheorie (TDDFT, engl. für *time-dependent density functional theory*) ist ein vielversprechender Kandidat für diese Aufgabe, da sie eine gute Balance zwischen Genauigkeit und Ressourcenaufwand ermöglicht. Es ist jedoch bekannt, dass TDDFT Probleme bei der Beschreibung von Ladungstransferzuständen und Doppelanregungen aufweist. In Kapitel 3 wird am Beispiel von  $\text{Fe}(\text{CO})_5$  gezeigt, dass Ladungstransferzustände mit einem sinnvoll gewählten Dichtefunktional gut modelliert werden können. Zudem wurden die Grenzen von TDDFT durch einen Vergleich zu CASPT2 (engl. für *complete active space perturbation theory second order*) aufgezeigt. CASPT2 zufolge treten bei höheren Dissoziationsbindungsängen doppelt angeregte Zustände auf, welche mit TDDFT nicht berechnet wurden. Daher muss man bei der

Simulation von Dissoziationen und anderen Prozessen mit sich stark verändernden Bindungslängen besonders vorsichtig sein. Wenn man diese Grenzen beachtet, kann TDDFT zur Modellierung der Dynamik großer Übergangsmetallkomplexe genutzt werden. Eine besonders effiziente Implementierung von TDDFT auf Graphikkarten kann zur weiteren Senkung der Rechenzeit um mehrere Größenordnungen im Vergleich zu CPU-Implementierungen beitragen, wie bereits für Berechnungen von stationären Punkten gezeigt wurde. Daher profitieren die Simulationen von großen Übergangsmetallkomplexen sehr von der Schnittstelle des GPU-basierten Programms TeraChem und der FMS90 Software, welche ich im Rahmen dieser Arbeit implementiert und für alle Berechnungen von Metallkomplexen benutzt habe.

Die oben genannte Methodenkombination ermöglicht die Berechnung des großen Übergangsmetallkomplexes Nickeltetramesithylporphyrin (NiTMP). Nach meinem besten Wissen war dies die erste Berechnung eines Übergangsmetallkomplexes mit mehr als 100 Atomen und einer Simulationszeit von 500 fs. Mit einer Rechenzeit von etwa 6 Monaten<sup>13</sup> für die Dynamik eines Konformeres sind solche Berechnungen nun in Reichweite, um routinemäßig an Metallkomplexen durchgeführt zu werden.

Für NiTMP wurde die Dynamik der angeregten Zustände durch experimentelle Anregung von Zuständen untersucht, die auf dem Liganden zentriert (LC, engl. für *ligand-centered*) sind, das heißt ( $\pi, \pi^*$ )-Anregungen, die dem wohlbekannten Q-band zugrunde liegen, welche mit einer Zeitkonstante von weniger als 0.6 ps entvölkert werden, wie mehrere Forschungsgruppen unabhängig voneinander ermittelten und näherungsweise durch die AIMS/TDDFT Berechnungen ( $\tau_{LC}=100$  fs) reproduziert wurden. Der angeregte Zustand, der final besetzt wird, ist ein auf dem Metall zentrierter (MC, engl. für *metal-centered*) Tripletzustand, welcher eine Lebenszeit von mehreren hundert Picosekunden hat, wie ebenfalls unabhängig von diesen Forschungsgruppen gezeigt wurde. Die Relaxation dieses finalen Zustandes zurück in den Grundzustand kann grundsätzlich nicht mit AIMS/TDDFT beschrieben werden, da TDDFT innerhalb der benutzten Näherungen die nichtadiabatische Kopplung zwischen angeregtem und Grundzustand nicht beschreiben kann. Allerdings wurde diese Lebenszeit ohne jeden Zweifel durch Experimente

---

<sup>13</sup> Bei Nutzung von zwei GPUs pro AIMS Einzelberechnung.

bestimmt, wohingegen die zentrale Frage, die momentan diskutiert wird, die nach der Beteiligung des angeregten Zustandes zwischen der initial LC-Anregung und dem letztlich besetzten Triplet MC-Zustand ist. Wie durch meine AIMS/TDDFT Berechnungen gezeigt wird, werden die initial angeregten LC-Zustände entvölkert während ein Ladungstransferzustand (LMCT, engl. für *ligand-to-metal charge-transfer*) und zwei MC-Zustände, in weniger als 200 fs besetzt werden. Diese Ergebnisse zeigen deutlich, dass beide Zwischenzustände mit annähernd der gleichen Geschwindigkeit besetzt werden, DIN EN.CITE <EndNote><Cite><Author>Ihee</Author><YeCT Zustandes deutlich um Faktor zwei übertrifft. Diese Quantifizierung der Beteiligung beider Zwischenzustände ermöglicht nun eine detaillierte Interpretation der scheinbar widersprüchlichen experimentellen Ergebnisse, die bisher publiziert wurden. Alle experimentellen Resultate können mit dem hier abgeleiteten Modell erklärt werden. In einige Experimenten wurde aufgrund ihrer begrenzten Zeitauflösung nur einer der Zwischenzustände beobachtet. Die neusten Röntgenabsorptionsexperimente zeigen zwei intermediäre Peaks mit ähnlichen Lebenszeiten, wie man aus dem Fehlen eines isosbestischen Punktes schlussfolgern kann.

Wie oben erwähnt, wurde die AIMS/TDDFT Kombination zur Vorhersage der Dynamik der angeregten Zustände von Nickelmethyl-3-devinylpyropheophorbide-a (NiDEPE) verwendet. Für diesen Komplex erschwert der Symmetriebruch die Beschreibung des Charakters der angeregten Zustände. Es war mir trotzdem möglich, den folgenden Reaktionsmechanismus zu bestimmen: Der angeregte LC-Zustand bevölkert den MC-Zustand mit einer Lebenszeit von weniger als 10 fs. Dieser Zustand gibt seine Besetzung anschließend mit einer Lebenszeit von 200 fs an einen weiteren MC-Zustand weiter, welcher mit einer Lebenszeit von 500 fs einen LMCT-Zustand bevölkert. Im Gegensatz zu NiTMP liegt hier ein sequentieller Reaktionsmechanismus vor, der auf deutlich kürzeren Zeitskalen stattfindet. Diese Simulation ist die Erste, die Vorhersagen über die ultraschnelle Dynamik eines Übergangsmetallkomplexes trifft und damit das Potential dieser Methoden für Routineanwendungen aufzeigt.

Alles in allem wurde in der Promotion AIMS für die Beschreibung von Übergangsmetallkomplexen ausgewählt, da gezeigt werden konnte, dass damit bessere Lebenszeiten für die angeregten Zustände berechnet werden können als mit FSSH. Des Weiteren wurde

TDDFT in seiner GPU-Implementierung als die Methode ausgewählt, die sich am besten zur Berechnung der elektronischen Struktur von großen Metallkomplexen mit zehn oder mehr angeregten Zuständen von Interesse und von Zeiten im Bereich mehreren hundert Femtosekunden eignet. Die ausgewählten Methoden wurden auf die bisher größte Berechnung von NiTMP, einem Übergangsmetallkomplex mit mehr als 100 Atomen, angewendet. Durch einen Vergleich zu experimentellen Ergebnissen wurden validiert, dass die Methoden für große Übergangsmetallkomplexe angewendet werden können und die Dynamik von NiTMP wurde weiter aufgeklärt. Diese neuen Erkenntnisse über die Dynamik von NiTMP demonstrieren, dass AIMS/TDDFT geeignet ist, um offene Fragestellungen zur ultraschnellen Dynamik der angeregten Zustände von Übergangsmetallkomplexen zu beantworten. Zusätzliche Simulationen des bisher kaum untersuchten NiDEPE zeigen außerdem, wie die Methoden ohne Vorkenntnisse über die Dynamik der angeregten Zustände benutzt werden können. Damit bilden die Simulationen dieser Promotion die Grundlage weiterer Untersuchungen der Dynamik von Übergangsmetallkomplexen durch die Demonstration der Vorteile aber auch der Nachteile von AIMS und TDDFT und des Weitern durch das Aufzeigen von Strategien zur Auswertung der Dynamik einer hohen Anzahl von angeregten Zuständen. Dies wird zudem begünstigt durch den weiteren Anstieg an zur Verfügung stehender Rechenleistung, welche die Berechnung längerer Zeiten als 500 fs ermöglichen wird. Damit rückt in Zukunft auch die Berechnung von Lebenszeiten im niedrigen Picosekundenbereich für große Übergangsmetallkomplexe in greifbare Nähe. Mit solch effizienten Methoden ist in Zukunft auch die Vorselektion von potentiellen Zielstrukturen für die Synthese möglich, wenn der Zeitaufwand für die Computerbasierte Vorauswahl unter den der tatsächlichen Synthese und experimentellen Charakterisierung fällt.

## 7 Appendix

### 7.1 The Hartree-Fock approach

The most naïve approximation for the multi-electron wave function is an independent description of each electron.(70) This is realized in the so-called Hartree product *ansatz* by multiplying one-electron wave functions  $\varphi_i(\mathbf{r}_j)$ , each of which only depends on the coordinates of one electron.(68) However, within this approximation, Pauli's exclusion principle is not fulfilled.(68) This is corrected within the Hartree-Fock (HF) approximation, which anti-symmetrizes the electronic wave function(129) by writing  $\phi_{HF}$  as a determinant, which is called the Slater determinant:(68)

$$\phi_{HF} = \frac{1}{\sqrt{n!}} \begin{vmatrix} \varphi_1(\mathbf{r}_1) & \varphi_2(\mathbf{r}_1) & \dots & \varphi_n(\mathbf{r}_1) \\ \varphi_1(\mathbf{r}_2) & \varphi_2(\mathbf{r}_2) & & \varphi_n(\mathbf{r}_2) \\ \cdot & \cdot & & \cdot \\ \cdot & \cdot & & \cdot \\ \varphi_1(\mathbf{r}_n) & \varphi_2(\mathbf{r}_n) & \dots & \varphi_n(\mathbf{r}_n) \end{vmatrix} \quad (7.1.1)$$

The  $i^{\text{th}}$  one-electron wave functions  $\varphi_i(j)$  of the  $j^{\text{th}}$  electron out of the  $n$  electrons is called molecular orbital. These orbitals are usually chosen to be orthonormal. Within this approximation, the energy equals to(68):

$$\begin{aligned} E_{HF} = & \int \varphi_i^*(\mathbf{r}) \left( -\frac{1}{2} \sum_i \nabla_i^2 + \hat{V}_{ext} \right) \varphi_i(\mathbf{r}) d\mathbf{r} \\ & + \frac{1}{2} \sum_{i,j} \int \frac{\varphi_i^*(\mathbf{r}_1) \varphi_i(\mathbf{r}_1) \varphi_j^*(\mathbf{r}_2) \varphi_j(\mathbf{r}_2)}{|\mathbf{r}_i - \mathbf{r}_j|} d\mathbf{r}_1 d\mathbf{r}_2 \\ & - \frac{1}{2} \sum_{i,j} \int \frac{\varphi_i^*(\mathbf{r}_1) \varphi_j(\mathbf{r}_1) \varphi_i(\mathbf{r}_2) \varphi_j^*(\mathbf{r}_2)}{|\mathbf{r}_i - \mathbf{r}_j|} d\mathbf{r}_1 d\mathbf{r}_2 \end{aligned} \quad (7.1.2)$$

The first term is the one-electron energy part, the second term embodies the classical Coulomb energy and the third term denotes the exchange energy. This energy expression is a **mean field approximation**, *i.e.* the electrons interact with a field that consists of the interactions between all electrons, where the interaction field for one electron depends on wave functions of all other electrons.(68) Because of this

dependence, an iterative procedure is needed to obtain the minimal energy and the corresponding orbitals.(68) This is called a self-consistent field (SCF) method(68) and yields variationally the electronic ground state wave function, where the  $n/2$  orbitals with the lowest energies are occupied. However, HF does not treat the correlation between particles of different spins correctly.(70) Therefore, the so called post-HF-methods have been introduced, which are based on the HF orbitals.(130) Some of these methods are detailed in the following two subsections.

## 7.2 Configuration Interaction and the importance of correlation

A variety of wave function determinants can be formed from the HF orbitals.(130) Starting from the reference ground state wave function, these can be described by the differences in occupations in relation to the ground state.(68) Depending on the number of orbitals with changed population, these determinants are classified as single, double, triple, ... excitations and can be used not only to approximate the ground state but also the excited states.(68) The exact wave function  $\phi_0$  can be constructed as a linear combination of all possible excitations, which is called full configuration interaction (full CI).(68)

$$|\phi_0\rangle = c_0 |\Phi_0\rangle + \sum_{ar} c_a^r |\Phi_a^r\rangle + \sum_{\substack{a<b \\ r<s}} c_{ab}^{rs} |\Phi_{ab}^{rs}\rangle + \sum_{\substack{a<b<c \\ r<s<t}} c_{abc}^{rst} |\Phi_{abc}^{rst}\rangle + \dots \quad (7.2.1)$$

A variational procedure is used to determine the coefficients,  $c$ , which minimize the energy. However, this is in practice only feasible for very small systems, as already for a molecule like  $N_2$  in a small basis set about  $10^{10}$  excitations need to be included in the calculation.(131) To avoid such scaling, CI calculations are often truncated, *e.g.* after the third term of equation (7.2.1), thereby only using single and double excitations, called CISD.(68) An alternative method, which is also mostly used in a truncated form, is the coupled cluster theory.(130) It takes the excitations into account via an exponential excitation operator(130), given here for the coupled-cluster singles-and-doubles (CCSD) truncation:

$$|\phi_0\rangle = e^{\hat{T}} |\Phi_0\rangle = e^{(\hat{T}_1 + \hat{T}_2)} |\Phi_0\rangle \quad (7.2.1)$$



Here,  $\hat{T}_1$  and  $\hat{T}_2$  are single and double excitation operators, respectively.(68)

Full CI accounts for the electronic interaction that is neglected by the mean field description of the HF method, which is called **electronic correlation**.(68) The correlation is usually divided into two parts: static and dynamic correlation(132). *Dynamic* correlation refers to the correlated movement of electrons, which originates from the fact that electrons avoid each other.(70) Electrons of different spins in the same orbital will move in a way so they do not get close to each other.(70) This effect, which is of general importance, cannot be treated in the mean field HF approximation. The use of configuration interaction methods like CISD and coupled cluster methods like CCSD will recover most of the dynamic correlation(70). *Static* correlation can be caused by near degeneracies of partially filled shells which might lead to a rearrangement of electrons within the shells.(133) This is of special importance for transition metals. Static correlation is also important for the description of bond breaking. Consider the dissociation of  $H_2$  into two hydrogen atoms. HF gives a wrong dissociation behavior(70): For long hydrogen-hydrogen distances, it predicts the same probability for having two isolated hydrogen atoms as for being in an ionic state where one hydrogen has both electrons, while the other is a plain proton. In order to describe such bond breaking correctly, one needs to consider more than one determinant for the reference wave function, which can be achieved with the so called **multi-reference** methods.(70) An ansatz to take static correlation into account and an extension to include both static and dynamic correlation are described briefly in the following subsection.

### 7.3 MCSCF, CASSCF and beyond

Instead of using a single determinant, as is the case in the HF method, within the multi-configuration self-consistent field (MCSCF) method multiple determinants are used as reference.(134) The MCSCF wave function  $\phi_{MCSCF}$  is defined as a linear combination of different configurations  $\psi_a$ :(134)

$$\phi_{MCSCF} = \sum_a A_a \psi_a \quad (7.3.1)$$

Here, determinants obtained from HF would not be a good choice for  $\psi_a$ , as they have been optimized for a single-reference.(68) Therefore, within the MCSCF one jointly optimizes also the  $\psi_a$ , which can be expanded in a basis of atomic orbitals:(68)

$$\psi_a = \sum_r B_a^r \phi_r \quad (7.3.2)$$

This is done using the variational principle by minimizing the energy with respect to the coefficients  $A$  and  $B$ .(134) Note that HF orbitals can be used as starting orbitals for the wave function of the self-consistent procedure. However, it is not *a priori* clear what configurations to include in the calculation.(68) Roos *et al.*(135) introduced an approach where all configurations within a given set of “active orbitals” are used, called complete active space self-consistent field method (CASSCF). By the choice of the active orbitals, it is also determined how many electrons are included in the configuration interaction treatment. This approach can be considered to be full CI within the space of the active orbitals. However, because of the inclusion of the orbitals in the variational optimization, all determinants are treated equally, in contrast to configuration interaction methods, where one determinant is singled out as a reference that is optimized.(70)

A generalization of this is the generalized active space self-consistent field method (GASSCF)(74). Within this method, an arbitrary number of subspaces of active orbitals is defined.(74) For these subspaces, a minimum and maximum occupation, i.e. total number of electrons inside the subspace, is then applied to limit the number of configurations included in the calculation.(74) A special case of this method is the restricted active space self-consistent field method (RASSCF), which has exactly three subspaces: one mostly occupied and one mostly unoccupied space with a restricted number of holes and electrons, respectively, and one subspace where all configurations are considered.(136)

All the aforementioned MCSCF methods include static correlation in the calculation.(70) However, because the variational principle is limited to the active orbitals, not all of the dynamic correlation can be captured.(70) Based on the CASSCF orbitals, dynamic correlation can be added *via* a perturbation theory treatment, e.g. within the complete

active space perturbation theory second order (CASPT2) method.(130) This method gives a second order estimate of the dynamic correlation energy and adds it to the CASSCF energy.(130)

All of the methods introduced in this subsection can be extended to the description of excited states. This is done by determining a common set of orbitals for all states of interest *via* the variational minimization of an averaged energy of all states, rather than just the ground state energy, called state-averaging.(72)

## 7.4 Density functional theory

### 7.4.1 Ground state density functional theory

Density functional theory (DFT) is based on the fact that the one-particle probability density of the ground state  $\rho_0(\mathbf{r})$  is, in principle, sufficient to obtain all desired information about the  $n$ -electron system, without the need to calculate the full wave function  $\phi(\mathbf{r}_1, \mathbf{r}_2 \dots \mathbf{r}_n)$  itself(83).

$$\rho_0(\mathbf{r}) = \int \phi(\mathbf{r}, \mathbf{r}_2, \mathbf{r}_3 \dots \mathbf{r}_n)^* \phi(\mathbf{r}, \mathbf{r}_2, \mathbf{r}_3 \dots \mathbf{r}_n) d\mathbf{r}_2 d\mathbf{r}_3 \dots d\mathbf{r}_n \quad (7.4.1)$$

This basis for this was laid by Hohenberg and Kohn in 1964 (137), who proved that there exists a one-to-one correspondence between the ground state density and the potential. Therefore, it is possible to reconstruct the Hamiltonian from the ground state density alone and from this, the full wave function can be obtained by solving the Schrödinger equation.(83) Hence, the wave function is formally a functional of the ground state density and thus also all observables can be written as density functionals.(83)

The description of observables with respect to the density can be advantageous as the density is a function of only three rather than  $3n$  variables like the full wave function.(80) However, one must find a way to use this advantage, as the full wave function is still needed to construct the density. The advantageous use of the density can be achieved by using the Kohn-Sham formalism(84): the density of the full interacting system is modelled by a fictitious system of noninteracting single-particles

that are described by orthogonal one-electron orbitals  $\varphi_i$ , known as Kohn-Sham-orbitals. Thus, the density can be calculated as:(138)

$$\rho_0 = \sum_i^N b_i |\varphi_i|^2 \quad (7.4.2)$$

Where the spin coordinate is taken into account by the occupation number  $b_i$  of the  $i^{\text{th}}$  orbital<sup>14</sup>, which gives consistency to Pauli's principle. Each of the Kohn-Sham orbitals fulfills a single-particle Schrödinger equation with the potential  $V_{KS}$  that reproduces the exact ground state density of the interacting system, the so-called Kohn-Sham equations:(83)

$$\left[ -\frac{1}{2} \nabla^2 + V_{KS}[\rho](\mathbf{r}) \right] \varphi_i(\mathbf{r}) = \varepsilon_i \varphi_i(\mathbf{r}) \quad (7.4.3)$$

The potential of the noninteracting system  $V_{KS}[\rho](\mathbf{r})$  therefore needs to correct for the interactions, which determine the full interacting system.(83) The potential can be split into three contributions:(83)

$$V_{KS}[\rho](\mathbf{r}) = V_{ext}(\mathbf{r}) + \int \frac{\rho(\mathbf{r}')}{|\mathbf{r} - \mathbf{r}'|} d\mathbf{r}' + v_{xc}[\rho](\mathbf{r}) \quad (7.4.4)$$

The first term on the right hand side is the external potential of the interacting system. The second term is the Hartree potential, which represents the classical Coulomb potential of the interacting system.(83)  $v_{xc}[\rho](\mathbf{r})$  accounts for all remaining electronic many-body effects and is given by the functional derivative of the exchange-correlation energy with respect to the density:(80)

$$v_{xc}[\rho](\mathbf{r}) = \frac{\delta E_{xc}[\rho]}{\delta \rho} \quad (7.4.5)$$

However, the exact exchange-correlation potential is not known and therefore has to be approximated.(83) Many different functionals for the exchange-correlation potential

---

<sup>14</sup> $b_i$  varies between zero and two

have been proposed, some based on parametrization and fit to experimental results, others purely on the basis of general rules of quantum mechanics.(83) The performance of each functional varies for specific applications.(80) For example, a special kind of functionals has been introduced in order to improve the accuracy for the calculation of charge-transfer states.(83) Therefore, care has to be taken when choosing a functional for a specific application.

#### 7.4.2 Time-dependent density functional theory

All the above considerations are only valid for the ground state. However, as this work focuses on excited-state dynamics, a time-dependent (TD) variant needs to be applied. The fundamentals and the basic approach of this TD theory are similar to the ground state DFT.(83) However, there are some important differences, which are therefore the topic of the next subsection.

The TD equivalent to Hohnberg and Kohn's theorems for the ground state was introduced by Runge and Gross (45) in 1984 and establishes for a given initial state a one-to-one connection between the TD density and the TD potential. In addition, the Kohn-Sham formalism can similarly be applied and yields the following TD Kohn-Sham equations for the noninteracting system:(83)

$$i \frac{\partial}{\partial t} \varphi_i(\mathbf{r}, t) = \left[ -\frac{1}{2} \nabla^2 + V_{KS}(\mathbf{r}, t) \right] \varphi_i(\mathbf{r}, t) \quad (7.4.6)$$

Where the TD effective external potential  $V_{KS}$  of the noninteracting system is now not just a functional of the density  $\rho$  but also a functional of the initial states of the interacting system  $\phi_0$  and the noninteracting systems  $\varphi_0$ .(83)

$$V_{KS}[\rho, \phi_0, \varphi_0](\mathbf{r}, t) = V_{ext}[\rho, \phi_0](\mathbf{r}, t) + V_H[\rho](\mathbf{r}, t) + V_{xc}[\rho, \phi_0, \varphi_0](\mathbf{r}, t) \quad (7.4.7)$$

When a system is initially in its ground state, the functional dependence on the initial states  $\phi_0$  and  $\varphi_0$  can be neglected, and, thus, it is only a functional of the density.(83) However, this dependence is highly non-local, as the potential at a given point in space-time depends on the density at all positions and at all earlier times.(83) One crude but often used approximation, the adiabatic approximation, which assumes that the

external potential varies so slowly with time that the density can react instantaneously and the history of the density can be neglected.(83) Within this approximation the well-known functionals of the ground state density functional theory can be used.(139) Even though this is often not the case, the adiabatic approximation has been proven to work quite well.(140) Hence, this approach is used in most of the implementations of TDDFT nowadays.(83)

In practice, one usually does not solve the TD Kohn-Sham equation, which would require to propagate these equations forward in time on a discretized time grid.(139) Instead, for applications like spectroscopy, it is usually sufficient to use perturbation theory, as excitation with visible light can be considered a weak probe.(83) The perturbation treatment is detailed in the next subsection.

#### 7.4.2.1 Linear response theory for excitation energies

In cases of small perturbations, the response of the density in first order dominates all higher order contributions.(83) This linear response theory can be used to directly calculate the change of different observables, like excitation energies, in first order without having to determine the wave function.(139) In the frequency, domain the linear response of the density  $\delta\rho(\mathbf{r},\omega)$  to a perturbative change of the potential  $\delta V_{ext}(\mathbf{r},t)$  can be written as follows:(139)

$$\delta\rho(\mathbf{r},\omega) = \int \xi(\mathbf{r},\mathbf{r}',\omega) \delta V_{ext}(\mathbf{r}',\omega) d\mathbf{r}' \quad (7.4.7)$$

Here, the density-density response function  $\xi(\mathbf{r},\mathbf{r}',\omega)$  was introduced. It can be calculated as follows:(83)

$$\begin{aligned} \xi(\mathbf{r},\mathbf{r}',\omega) = & \lim_{\eta \rightarrow 0^+} \sum_i \langle \phi_{gs} | \rho(\mathbf{r}) | \phi_i \rangle \langle \phi_i | \rho(\mathbf{r}') | \phi_{gs} \rangle \\ & \times \left( \frac{1}{\omega - (\varepsilon_i - \varepsilon_0) + i\eta} - \frac{1}{\omega + (\varepsilon_i - \varepsilon_0) + i\eta} \right) \end{aligned} \quad (7.4.7)$$

From this, it is evident that this function has poles at the exact excitation energies  $(\varepsilon_i - \varepsilon_0)$  of the many-body system.(83) Within the Kohn-Sham formalism, one can find a

similar equation for the density-density response function  $\xi_{KS}$  of the noninteracting system.(83) However, to reconstruct the exact poles of the interacting system from the Kohn-Sham density-density response function, one has to use a self-consistent algorithm.(83) In order to avoid possible numerical instabilities with such an iterative solution, another algorithm for the solution was introduced. It is detailed in the next subsection.

#### 7.4.2.2 Casida Equations

An easier calculation scheme for absorption spectra was developed by Casida (138) in 1995. He reformulated the linear response equations in a manner similar to how systems of coupled oscillators are treated in classical mechanics(141) when the oscillations are small. Starting from the equations of motion, the following eigenvalue equation can be derived:(138)

$$\Omega(\omega) \mathbf{F}_{kl} = \omega_{kl}^2 \mathbf{F}_{kl} \quad (7.4.7)$$

Here, the excitation energies are the eigenvalues  $\omega_{kl}$  and the oscillator strengths can be obtained from the eigenvectors  $\mathbf{F}_{kl}$ . The matrix elements  $\Omega_{ij}(\omega)$  are:(140)

$$\Omega_{ij}(\omega) = \delta_{ik} \delta_{jl} \omega_{kl}^2 + 2\sqrt{\omega_{ij} \omega_{kl}} K_{ij,kl} \quad (7.4.7)$$

Here, the coupling matrix  $K_{ij,kl}(\omega)$  is introduced as follows:(83)

$$K_{ij,kl}(\omega) = \int d\mathbf{r}' \int d\mathbf{r} \varphi_i^*(\mathbf{r}) \varphi_j^*(\mathbf{r}) \left[ \frac{1}{|\mathbf{r} - \mathbf{r}'|} + f_{xc}(\mathbf{r}, \mathbf{r}', \omega) \right] \varphi_k(\mathbf{r}') \varphi_l(\mathbf{r}') \quad (7.4.7)$$

The K matrix couples excitations and de-excitations. It is set to zero within the Tamm-Dancoff approximation, which is valid if the excitation energies are not close to zero. This approximation is often applied, as it compensates for errors that are introduced because the exact exchange-correlation functional is not known.(83)

## 7.5 Population changes in $Fe(CO)_5$

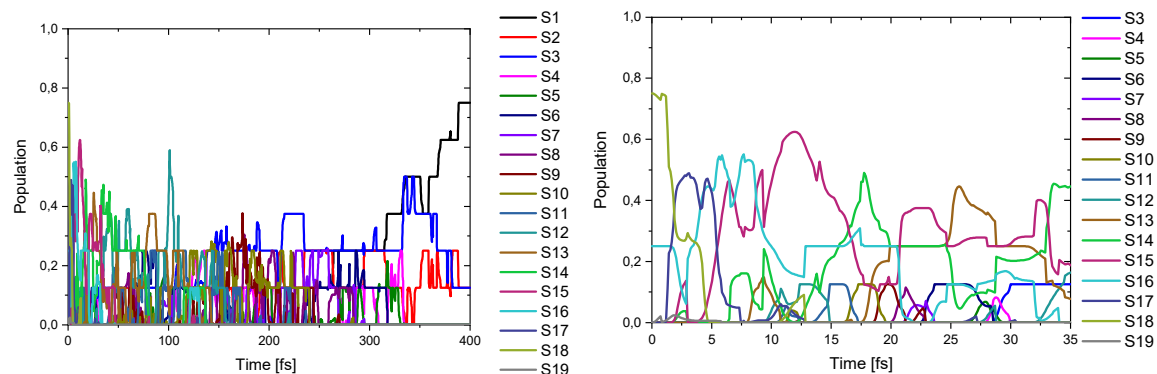


Figure 22: Population change of all 19 singlet excited states during the first a) 400 and b) 35 fs of the SSAIMS-dynamics averaged over all TBFs.

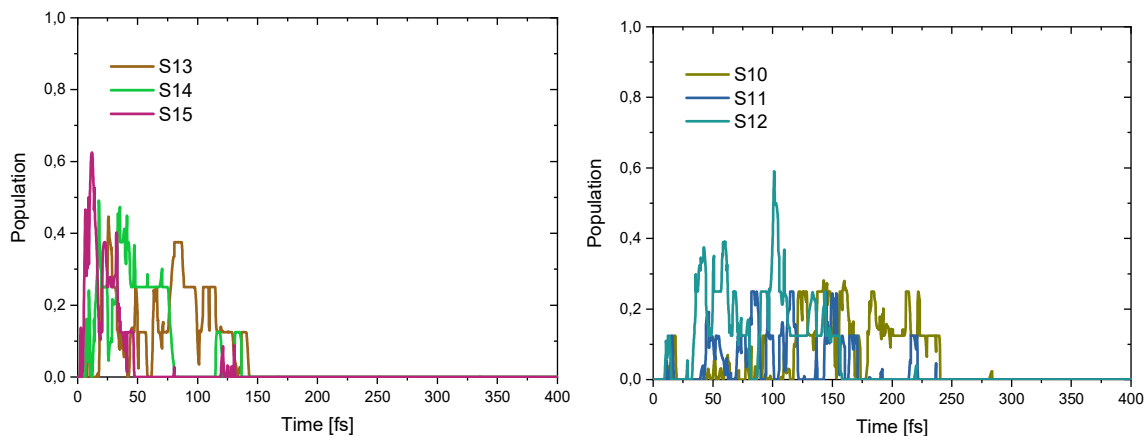


Figure 23: Population change of singlet excited states a)  $S_{13}$  to  $S_{15}$  and b)  $S_{10}$  to  $S_{12}$  during the first 400 fs of the SSAIMS-dynamics averaged over all TBFs.

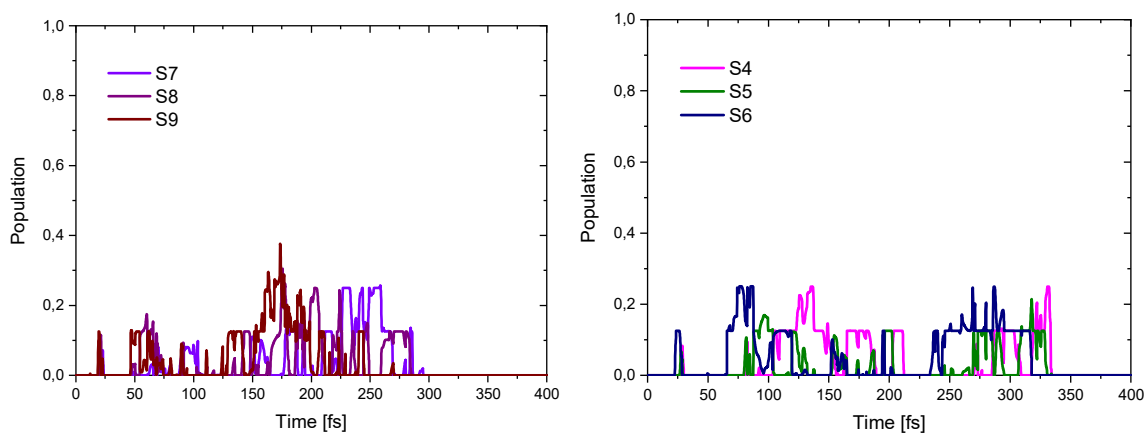


Figure 24: Population change of singlet excited states a)  $S_7$  to  $S_9$  and b)  $S_4$  to  $S_6$  during the first 400 fs of the SSAIMS-dynamics averaged over all TBFs.



## 7.6 Algorithm for the $E_{rel}$ -analysis for all time steps during the dynamics

- For each time step of each trajectory basis function:
- If exactly one pair of degenerate states is found among the five lowest singlet states ( $\Delta E \leq 65$  meV)
  - Assign them  $MC_2$  and  $MC_3$  character
  - Search among the lower states for a state with an energy difference to  $MC_2$  between 125 meV and 178 meV (these values are determined empirically based on the energy differences at the stationary points)
    - If exactly one was found
    - $\rightarrow$  assign it  $MC_1$  character
    - $\rightarrow$  other states with energy lower than  $MC_2$  are assigned LMCT character
  - Search for a pair of degenerate states within the states above  $MC_3$  (up to state  $S_7$ ) ( $\Delta E \leq 45$  meV)
    - If exactly one pair is found
    - $\rightarrow$  assign them  $LC_1$  and  $LC_2$  character
    - $\rightarrow$  other states will be assigned LMCT character
- Only if all MC and LC state could be assigned, the information for this time step is printed for further analysis.

## 7.7 Fit formulae for dynamics of NiTMP

Sequential fit of the dynamics for the FC-analysis:

$$P(LC) = e^{-\frac{t}{\tau_1}}$$

$$P(LMCT) = \left(1 - e^{-\frac{t}{\tau_1}}\right) \cdot e^{-\frac{t}{\tau_2}}$$

$$P(MC_{2,3}) = \left(1 - e^{-\frac{t}{\tau_1}}\right) \cdot \left(1 - e^{-\frac{t}{\tau_2}}\right) \cdot e^{-\frac{t}{\tau_3}}$$

$$P(MC_1) = \left(1 - e^{-\frac{t}{\tau_1}}\right) \cdot \left(1 - e^{-\frac{t}{\tau_2}}\right) \cdot \left(1 - e^{-\frac{t}{\tau_3}}\right)$$

$$LC \xrightarrow{\tau_1} LMCT \xrightarrow{\tau_2} MC_{2,3} \xrightarrow{\tau_3} MC_1$$

Non-sequential fit of the dynamics for the  $E_{\text{rel}}$ -analysis:

$$P(\text{LC}) = e^{-\frac{t}{\tau_1}}$$

$$P(\text{LMCT}) = a \left(1 - e^{-\frac{t}{\tau_1}}\right) \cdot e^{-\frac{t}{\tau_2}}$$

$$P(\text{MC}_{2,3}) = (1 - a) \cdot \left(1 - e^{-\frac{t}{\tau_1}}\right) \cdot e^{-\frac{t}{\tau_3}}$$

$$P(\text{MC}_1) = \left(1 - e^{-\frac{t}{\tau_1}}\right) \cdot \left[ a \left(1 - e^{-\frac{t}{\tau_2}}\right) + (1 - a) \left(1 - e^{-\frac{t}{\tau_3}}\right) \right]$$

## 7.8 XANES calculation

The calculation of transient X-ray spectra needs to be done in two steps. First, the wave functions of the states to probe are calculated at their respective minimum geometry. Using these wave functions, the core excitations are then simulated. The core excitations can only be modeled with an all-electron basis set because one needs to describe the Ni 1s orbital explicitly. Hence, for all XANES calculations, the polarizable double zeta basis set of Ahlrichs *et al.*(65) was used. After optimization of the geometries for the ground states and all electronic states of interest, the maximum overlap method (MOM)(142) was applied to converge the SCF to the wave function of the excited states of interest. Based on these orbitals, the X-ray absorption was simulated by a CASCI calculation with an active space of two electrons in 71 orbitals, where the Ni 1s orbital was swapped with the HOMO to include it in the active space of the calculation.

## 8 Bibliography

### List of Publication with My Participation

7. J. Preiß *et al.*, How Does Peripheral Functionalization of Ruthenium(II)–Terpyridine Complexes Affect Spatial Charge Redistribution after Photoexcitation at the Franck–Condon Point? *ChemPhysChem* **16**, 1395-1404 (2015).
8. J. Preiß *et al.*, Absorption and Fluorescence Features of an Amphiphilic meso-Pyrimidinylcorrole: Experimental Study and Quantum Chemical Calculations. *The Journal of Physical Chemistry A* **121**, 8614-8624 (2017).
9. J. Preiß *et al.*, Ab-initio Prediction of Fluorescence Lifetimes Involving Solvent Environments by Means of COSMO and Vibronic Effects. *In preparation*, (2018).
11. J. Preiß, B. Curchod, B. Dietzek, T. Martinez, M. Presselt, Ab-initio multiple spawning calculation of ultrafast excited-state dynamics in Nickel Tetra-Mesityl-Porphyrin and NiDEPE. *In preparation*, (2018).
99. C. Song *et al.*, Efficient implementation of effective core potential integrals and gradients on graphical processing units. *The Journal of Chemical Physics* **143**, 014114 (2015).

### Other References

1. G. Serdaroğlu, J. V. Ortiz, Ab Initio Calculations on some Antiepileptic Drugs such as Phenytoin, Phenbarbital, Ethosuximide and Carbamazepine. *Structural Chemistry* **28**, 957-964 (2017).
2. T. van Mourik, First-principles quantum chemistry in the life sciences. *Philosophical Transactions of the Royal Society of London. Series A: Mathematical, Physical and Engineering Sciences* **362**, 2653 (2004).
3. M. Kaupp, F. H. Köhler, Combining NMR spectroscopy and quantum chemistry as tools to quantify spin density distributions in molecular magnetic compounds. *Coordination Chemistry Reviews* **253**, 2376-2386 (2009).
4. C. Duboc, Determination and prediction of the magnetic anisotropy of Mn ions. *Chemical Society Reviews* **45**, 5834-5847 (2016).
5. V. van Speybroeck, R. Gani, R. J. Meier, The calculation of thermodynamic properties of molecules. *Chemical Society Reviews* **39**, 1764-1779 (2010).
6. A. Jinich *et al.*, Quantum Chemical Approach to Estimating the Thermodynamics of Metabolic Reactions. *Scientific Reports* **4**, 7022 (2014).
10. D. A. McQuarrie, *Quantum Chemistry (Physical Chemistry Series)*. (University Science Books, 1983), pp. 517.
12. M. L. Shelby *et al.*, Ultrafast Excited State Relaxation of a Metalloporphyrin Revealed by Femtosecond X-ray Absorption Spectroscopy. *J. Am. Chem. Soc.* **138**, 8752-8764 (2016).
13. P. J. Stephens, F. J. Devlin, C. F. Chabalowski, M. J. Frisch, Ab-Initio Calculation of Vibrational Absorption and Circular-Dichroism Spectra Using Density-Functional Force-Fields. *The Journal of Physical Chemistry* **98**, 11623-11627 (1994).
14. C. Diedrich, S. Grimme, Systematic investigation of modern quantum chemical methods to predict electronic circular dichroism spectra. *The Journal of Physical Chemistry A* **107**, 2524-2539 (2003).
15. A. H. Zewail, Femtochemistry: Atomic-Scale Dynamics of the Chemical Bond. *The Journal of Physical Chemistry A* **104**, 5660-5694 (2000).
16. S. Mai, M. Richter, P. Marquetand, L. González, in *Photoinduced Phenomena in Nucleic Acids I: Nucleobases in the Gas Phase and in Solvents*, M. Barbatti, A. C. Borin, S. Ullrich, Eds. (Springer International Publishing, Cham, 2015), pp. 99-153.

17. M. H. Beck, A. Jäckle, G. A. Worth, H. D. Meyer, The multiconfiguration time-dependent Hartree (MCTDH) method: a highly efficient algorithm for propagating wavepackets. *Physics Reports* **324**, 1-105 (2000).
18. J. E. Subotnik *et al.*, Understanding the Surface Hopping View of Electronic Transitions and Decoherence. *Annual Review of Physical Chemistry* **67**, 387-417 (2016).
19. M. Ben-Nun, J. Quenneville, T. J. Martínez, Ab Initio Multiple Spawning: Photochemistry from First Principles Quantum Molecular Dynamics. *The Journal of Physical Chemistry A* **104**, 5161-5175 (2000).
20. M. Persico, G. Granucci, An overview of nonadiabatic dynamics simulations methods, with focus on the direct approach versus the fitting of potential energy surfaces. *Theor. Chem. Acc.* **133**, 1526 (2014).
21. M. Barbatti, Nonadiabatic dynamics with trajectory surface hopping method. *Wiley Interdisciplinary Reviews: Computational Molecular Science* **1**, 620-633 (2011).
22. G. A. Worth, M. A. Robb, B. Lasorne, Solving the time-dependent Schrödinger equation for nuclear motion in one step: direct dynamics of non-adiabatic systems. *Molecular Physics* **106**, 2077-2091 (2008).
23. B. R. Landry, J. E. Subotnik, Quantifying the Lifetime of Triplet Energy Transfer Processes in Organic Chromophores: A Case Study of 4-(2-Naphthylmethyl)benzaldehyde. *Journal of Chemical Theory and Computation* **10**, 4253-4263 (2014).
24. J. C. Tully, R. K. Preston, Trajectory Surface Hopping Approach to Nonadiabatic Molecular Collisions: The Reaction of H<sup>+</sup> with D<sub>2</sub>. *The Journal of Chemical Physics* **55**, 562 (1971).
25. J. C. Tully, Molecular dynamics with electronic transitions. *The Journal of Chemical Physics* **93**, 1061-1071 (1990).
26. Y. Fan *et al.*, Methyl substitution enhanced photoisomerization of trans,trans-1,4-diphenyl-1,3-butadiene: direct ab initio trajectory surface hopping dynamic simulations. *Physical Chemistry Chemical Physics* **20**, 2260-2273 (2018).
27. Y. Gan, L. Yue, X. Guo, C. Zhu, Z. Cao, Multi-state nonadiabatic deactivation mechanism of coumarin revealed by ab initio on-the-fly trajectory surface hopping dynamic simulation. *Physical Chemistry Chemical Physics* **19**, 12094-12106 (2017).
28. S. Mai, P. Marquetand, M. Richter, J. González-Vázquez, L. González, Singlet and Triplet Excited-State Dynamics Study of the Keto and Enol Tautomers of Cytosine. *Chemphyschem* **14**, 2920-2931 (2013).
29. J. W. Park, T. Shiozaki, On-the-Fly CASPT2 Surface-Hopping Dynamics. *Journal of Chemical Theory and Computation* **13**, 3676-3683 (2017).
30. R. Crespo-Otero, M. Barbatti, Cr(CO)<sub>6</sub> photochemistry: Semi-classical study of UV absorption spectral intensities and dynamics of photodissociation. *The Journal of Chemical Physics* **134**, 164305 (2011).
31. I. Tavernelli, B. F. E. Curchod, U. Rothlisberger, Nonadiabatic molecular dynamics with solvent effects: A LR-TDDFT QM/MM study of ruthenium (II) tris (bipyridine) in water. *Chem. Phys.* **391**, 101-109 (2011).
32. X. Liu, F. Y. Wang, Transition metal complexes that catalyze oxygen formation from water: 1979-2010. *Coord. Chem. Rev.* **256**, 1115-1136 (2012).
33. S. Mathew *et al.*, Dye-sensitized solar cells with 13% efficiency achieved through the molecular engineering of porphyrin sensitizers. *Nat Chem* **6**, 242-247 (2014).
34. M. Gratzel, Solar energy conversion by dye-sensitized photovoltaic cells. *Inorg. Chem.* **44**, 6841-6851 (2005).
35. H. K. Liu, P. J. Sadler, Metal Complexes as DNA Intercalators. *Acc. Chem. Res.* **44**, 349-359 (2011).
36. T. W. Liu, E. Huynh, T. D. MacDonald, G. Zheng, in *Cancer Theranostics*. (Academic Press, Oxford, 2014), pp. 229-254.

37. A. Hagfeldt, G. Boschloo, L. C. Sun, L. Kloo, H. Pettersson, Dye-Sensitized Solar Cells. *Chemical Reviews* **110**, 6595-6663 (2010).
38. S. Ardo, G. J. Meyer, Photodriven heterogeneous charge transfer with transition-metal compounds anchored to TiO<sub>2</sub> semiconductor surfaces. *Chemical Society Reviews* **38**, 115-164 (2009).
39. B. F. E. Curchod, T. J. Martínez, Ab Initio Nonadiabatic Quantum Molecular Dynamics. *Chemical Reviews* **118**, 3305-3336 (2018).
40. A. Virshup, B. Levine, T. Martínez, Steric and electrostatic effects on photoisomerization dynamics using QM/MM ab initio multiple spawning. *Theor. Chem. Acc.* **133**, 1-11 (2014).
41. J. W. Snyder, B. F. E. Curchod, T. J. Martínez, GPU-Accelerated State-Averaged Complete Active Space Self-Consistent Field Interfaced with Ab Initio Multiple Spawning Unravels the Photodynamics of Provitamin D<sub>3</sub>. *The Journal of Physical Chemistry Letters* **7**, 2444-2449 (2016).
42. T. J. A. Wolf *et al.*, Hexamethylcyclopentadiene: time-resolved photoelectron spectroscopy and ab initio multiple spawning simulations. *Phys. Chem. Chem. Phys.* **16**, 11770-11779 (2014).
43. M. Iwamura, S. Takeuchi, T. Tahara, Ultrafast Excited-State Dynamics of Copper(I) Complexes. *Accounts of Chemical Research* **48**, 782-791 (2015).
44. F. de Carvalho, M. Bouduban, B. F. E. Curchod, I. Tavernelli, Nonadiabatic Molecular Dynamics Based on Trajectories. *Entropy* **16**, 62 (2014).
45. E. Runge, E. K. U. Gross, Density-Functional Theory For Time-Dependent Systems. *Phys. Rev. Lett.* **52**, 997-1000 (1984).
46. D. R. Hartree, *The Wave Mechanics of an Atom with a Non-Coulomb Central Field. Part I. Theory and Methods.* (1928), vol. 24.
47. M. Born, K. Huang, *Dynamical theory of crystal lattices.* (Clarendon Press, 1954).
48. M. Born, *Kopplung der Elektronen- und Kernbewegung in Molekeln und Kristallen, von M. Born.* (Vandenhoeck und Ruprecht, 1951).
49. A. Hofmann, Ludwig-Maximilians-Universität, (2001).
50. L. T. Belcher, Air University, (2011).
51. A. n. Vlček, The life and times of excited states of organometallic and coordination compounds. *Coordination Chemistry Reviews* **200-202**, 933-978 (2000).
52. H. D. Meyer, F. Gatti, G. A. Worth, *Multidimensional Quantum Dynamics.* (Wiley-VCH Verlag GmbH & Co. KGaA, 2009).
53. Q. Meng, H.-D. Meyer, A multilayer MCTDH study on the full dimensional vibronic dynamics of naphthalene and anthracene cations. *The Journal of Chemical Physics* **138**, 014313 (2013).
54. I. Tavernelli, E. Tapavicza, U. Rothlisberger, Non-adiabatic dynamics using time-dependent density functional theory: Assessing the coupling strengths. *Journal of Molecular Structure: THEOCHEM* **914**, 22-29 (2009).
55. O. V. Prezhdo, P. J. Rossky, Evaluation of quantum transition rates from quantum-classical molecular dynamics simulations. *The Journal of Chemical Physics* **107**, 5863-5878 (1997).
56. K. F. Wong, P. J. Rossky, Solvent-induced electronic decoherence: Configuration dependent dissipative evolution for solvated electron systems. *The Journal of Chemical Physics* **116**, 8429-8438 (2002).
57. M. Ben-Nun, T. J. Martínez, in *Adv. Chem. Phys.* (John Wiley & Sons, Inc., 2002), pp. 439-512.
58. B. F. E. Curchod, W. J. Glover, T. J. Martinez, SSAIMS – Stochastic-Selection Ab Initio Multiple Spawning for Efficient Nonadiabatic Molecular Dynamics. *In preparation*, (2018).

59. J. K. McCusker, Femtosecond Absorption Spectroscopy of Transition Metal Charge-Transfer Complexes. *Acc. Chem. Res.* **36**, 876-887 (2003).
60. M. D. Hack, A. M. Wensmann, D. G. Truhlar, M. Ben-Nun, T. J. Martínez, Comparison of full multiple spawning, trajectory surface hopping, and converged quantum mechanics for electronically nonadiabatic dynamics. *The Journal of Chemical Physics* **115**, 1172-1186 (2001).
61. A. Toniolo, C. Ciminelli, M. Persico, T. J. Martinez, Simulation of the photodynamics of azobenzene on its first excited state: Comparison of full multiple spawning and surface hopping treatments. *The Journal of Chemical Physics* **123**, 234308 (2005).
62. B. Xie *et al.*, Ab initio implementation of quantum trajectory mean-field approach and dynamical simulation of the N<sub>2</sub>CO photodissociation. *The Journal of Chemical Physics* **143**, 194107 (2015).
63. G. Granucci, M. Persico, A. Zocante, Including quantum decoherence in surface hopping. *The Journal of Chemical Physics* **133**, 134111 (2010).
64. G. Granucci, M. Persico, Excited state dynamics with the direct trajectory surface hopping method: azobenzene and its derivatives as a case study. *Theoretical Chemistry Accounts* **117**, 1131-1143 (2007).
65. A. Schäfer, H. Horn, R. Ahlrichs, Fully optimized contracted Gaussian basis sets for atoms Li to Kr. *The Journal of Chemical Physics* **97**, 2571-2577 (1992).
66. C. M. Isborn, N. Luehr, I. S. Ufimtsev, T. J. Martínez, Excited-State Electronic Structure with Configuration Interaction Singles and Tamm-Dancoff Time-Dependent Density Functional Theory on Graphical Processing Units. *J. Chem. Theory Comput.* **7**, 1814-1823 (2011).
67. I. Tavernelli, Nonadiabatic Molecular Dynamics Simulations: Synergies between Theory and Experiments. *Acc. Chem. Res.* **48**, 792-800 (2015).
68. A. Szabo, N. S. Ostlund, *Modern Quantum Chemistry: Introduction to Advanced Electronic Structure Theory*. (Dover Publications, Inc., Mineola, 1996).
69. R. Chakraborty, P. Ghosh, D. Ghosh, Evolutionary algorithm based configuration interaction approach. *Int. J. Quantum Chem* **118**, e25509 (2018).
70. D. P. Tew, W. Klopper, T. Helgaker, Electron correlation: The many-body problem at the heart of chemistry. *J. Comput. Chem.* **28**, 1307-1320 (2007).
71. B. Mignolet, B. F. E. Curchod, T. J. Martínez, Rich Athermal Ground-State Chemistry Triggered by Dynamics through a Conical Intersection. *Angewandte Chemie International Edition* **55**, 14993-14996 (2016).
72. R. N. Diffenderfer, D. R. Yarkony, Use of the state-averaged MCSCF procedure: application to radiative transitions in magnesium oxide. *The Journal of Physical Chemistry* **86**, 5098-5105 (1982).
73. A. Veillard, J. Demuyneck, in *Applications of Electronic Structure Theory*, H. F. Schaefer, Ed. (Springer US, Boston, MA, 1977), pp. 187-222.
74. D. Ma, G. L. Manni, L. Gagliardi, The generalized active space concept in multiconfigurational self-consistent field methods. *The Journal of Chemical Physics* **135**, 044128 (2011).
75. D. Ma, G. Li Manni, J. Olsen, L. Gagliardi, Second-Order Perturbation Theory for Generalized Active Space Self-Consistent-Field Wave Functions. *Journal of Chemical Theory and Computation* **12**, 3208-3213 (2016).
76. K. D. Vogiatzis, G. Li Manni, S. J. Stoneburner, D. Ma, L. Gagliardi, Systematic Expansion of Active Spaces beyond the CASSCF Limit: A GASSCF/SplitGAS Benchmark Study. *Journal of Chemical Theory and Computation* **11**, 3010-3021 (2015).
77. D. Escudero, L. González, RASPT2/RASSCF vs Range-Separated/Hybrid DFT Methods: Assessing the Excited States of a Ru(II)bipyridyl Complex. *J. Chem. Theory Comput.* **8**, 203-213 (2012).

78. F. Krausbeck, D. Mendive-Tapia, A. J. W. Thom, M. J. Bearpark, Choosing RASSCF orbital active spaces for multiple electronic states. *Computational and Theoretical Chemistry* **1040-1041**, 14-19 (2014).
79. V. Santolini, J. P. Malhado, M. A. Robb, M. Garavelli, M. J. Bearpark, Photochemical reaction paths of cis-dienes studied with RASSCF: the changing balance between ionic and covalent excited states. *Molecular Physics* **113**, 1978-1990 (2015).
80. S. Sousa, P. Fernandes, M. Ramos, General Performance of Density Functionals. *The Journal of Physical Chemistry A* **111**, 10439-10452 (2007).
81. B. O. Roos, R. Lindh, P. Å. Malmqvist, V. Veryazov, P. O. Widmark, in *Multiconfigurational Quantum Chemistry*, B. O. Roos, R. Lindh, P. Å. Malmqvist, V. Veryazov, P. O. Widmark, Eds. (John Wiley & Sons, 2016), pp. 103-130.
82. M. A. L. Marques, N. T. Maitra, F. M. S. Nogueira, E. K. U. Gross, A. Rubio, *Fundamentals of Time-Dependent Density Functional Theory*. Lecture Notes in Physics (Springer Berlin Heidelberg, Berlin, Heidelberg, 2012).
83. C. A. Ullrich, Z.-h. Yang, A Brief Compendium of Time-Dependent Density Functional Theory. *Brazilian Journal of Physics* **44**, 154-188 (2014).
84. W. Kohn, L. J. Sham, Self-Consistent Equations Including Exchange and Correlation Effects. *Physical Review* **140**, A1133 (1965).
85. A. J. Atkins, L. González, Trajectory Surface-Hopping Dynamics Including Intersystem Crossing in [Ru(bpy)<sub>3</sub>]<sup>2+</sup>. *The Journal of Physical Chemistry Letters* **8**, 3840-3845 (2017).
86. A. Vlček, S. Zálaiš, Modeling of charge-transfer transitions and excited states in d6 transition metal complexes by DFT techniques. *Coordination Chemistry Reviews* **251**, 258-287 (2007).
87. C. Adamo, V. Barone, Inexpensive and accurate predictions of optical excitations in transition-metal complexes: the TDDFT/PBE0 route. *Theoretical Chemistry Accounts* **105**, 169-172 (2000).
88. M. Huix-Rotllant, A. Nikiforov, W. Thiel, M. Filatov, in *Density-Functional Methods for Excited States*, N. Ferré, M. Filatov, M. Huix-Rotllant, Eds. (Springer International Publishing, Cham, 2016), pp. 445-476.
89. C. Long, in *Photophysics of Organometallics*, A. J. Lees, Ed. (Springer Berlin Heidelberg, Berlin, Heidelberg, 2010), pp. 159-191.
90. R. J. Ryther, E. Weitz, Diode laser probes of the product distribution of coordinatively unsaturated iron carbonyls produced following excimer laser photolysis of iron pentacarbonyl in the gas phase. *The Journal of Physical Chemistry* **96**, 2561-2567 (1992).
91. S. A. Trushin, W. Fuss, K. L. Kompa, W. E. Schmid, Femtosecond Dynamics of Fe(CO)<sub>5</sub> Photodissociation at 267 nm Studied by Transient Ionization. *The Journal of Physical Chemistry A* **104**, 1997-2006 (2000).
92. H. Ihee, J. Cao, A. H. Zewail, Ultrafast Electron Diffraction of Transient [Fe(CO)<sub>4</sub>]: Determination of Molecular Structure and Reaction Pathway. *Angew. Chem. Int. Ed.* **40**, 1532-1536 (2001).
93. C. Daniel, M. Benard, A. Dedieu, R. Wiest, A. Veillard, Theoretical aspects of the photochemistry of organometallics. 3. Potential energy curves for the photodissociation of pentacarbonyliron (Fe(CO)<sub>5</sub>). *The Journal of Physical Chemistry* **88**, 4805-4811 (1984).
94. M.-C. Heitz, C. Daniel, Photodissociation Dynamics of Organometallics: Quantum Simulation for the Dihydride Complex H<sub>2</sub>Fe(CO)<sub>4</sub>. *Journal of the American Chemical Society* **119**, 8269-8275 (1997).
95. L. A. Barnes, M. Rosi, C. W. B. Jr., An ab initio study of Fe(CO)<sub>n</sub>, n=1,5, and Cr(CO)<sub>6</sub>. *The Journal of Chemical Physics* **94**, 2031-2039 (1991).
96. O. Rubner, V. Engel, M. R. Hachey, C. Daniel, A CASSCF/MR-CCI study of the excited states of Fe(CO)<sub>5</sub>. *Chem. Phys. Lett.* **302**, 489-494 (1999).

97. A. Marquez, C. Daniel, J. Fernandez Sanz, The vacuum-ultraviolet spectrum of iron pentacarbonyl: An experimental analysis supported by a CASSCF CCI study of the Rydberg states. *The Journal of Physical Chemistry* **96**, 121-123 (1992).
98. M. Kotzian, N. Rösch, H. Schröder, M. C. Zerner, Optical spectra of transition-metal carbonyls: chromium hexacarbonyl, iron pentacarbonyl, and nickel tetracarbonyl. *J. Am. Chem. Soc.* **111**, 7687-7696 (1989).
100. T. H. Dunning, P. J. Hay, in *Methods of Electronic Structure Theory*, H. F. Schaefer, Ed. (Springer US, Boston, MA, 1977), chap. 1, pp. 1-27.
101. W. R. Wadt, P. J. Hay, Ab initio effective core potentials for molecular calculations. Potentials for main group elements Na to Bi. *The Journal of Chemical Physics* **82**, 284-298 (1985).
102. L. Bañares, T. Baumert, M. Bergt, B. Kiefer, G. Gerber, The ultrafast photodissociation of Fe(CO)<sub>5</sub> in the gas phase. *The Journal of Chemical Physics* **108**, 5799-5811 (1998).
103. H. R. Wang *et al.*, Silica-Metal Core-Shells and Metal Shells Synthesized by Porphyrin-Assisted Photocatalysis. *Chem. Mater.* **20**, 7434-7439 (2008).
104. D. G. Wu *et al.*, Novel NO Biosensor Based on the Surface Derivatization of GaAs by "Hinged" Iron porphyrins. *Angew. Chem. Int. Ed.* **39**, 4496-4500 (2000).
105. M.-C. Yoon *et al.*, Photophysics of meso- $\beta$  Doubly Linked Ni(II) Porphyrin Arrays: Large Two-Photon Absorption Cross-Section and Fast Energy Relaxation Dynamics. *J. Am. Chem. Soc.* **129**, 10080-10081 (2007).
106. K. Kurotobi, K. S. Kim, S. B. Noh, D. Kim, A. Osuka, A Quadruply Azulene-Fused Porphyrin with Intense Near-IR Absorption and a Large Two-Photon Absorption Cross Section. *Angew. Chem. Int. Ed.* **45**, 3944-3947 (2006).
107. J. Barbee, A. E. Kuznetsov, Revealing substituent effects on the electronic structure and planarity of Ni-porphyrins. *Computational and Theoretical Chemistry* **981**, 73-85 (2012).
108. Y. Mizutani, Y. Uesugi, T. Kitagawa, Intramolecular vibrational energy redistribution and intermolecular energy transfer in the (d,d) excited state of nickel octaethylporphyrin. *The Journal of Chemical Physics* **111**, 8950-8962 (1999).
109. J. Rodriguez, D. Holten, Ultrafast vibrational dynamics of a photoexcited metalloporphyrin. *The Journal of Chemical Physics* **91**, 3525-3531 (1989).
110. C. M. Drain *et al.*, Picosecond to microsecond photodynamics of a nonplanar nickel porphyrin: Solvent dielectric and temperature effects. *J. Am. Chem. Soc.* **120**, 3781-3791 (1998).
111. A. V. Zamyatin, A. V. Gusev, M. A. J. Rodgers, Two-Pump-One-Probe Femtosecond Studies of Ni(II) Porphyrins Excited States. *J. Am. Chem. Soc.* **126**, 15934-15935 (2004).
112. S. Sorgues *et al.*, Femtosecond electronic relaxation of excited metalloporphyrins in the gas phase. *The Journal of Chemical Physics* **124**, 114302 (2006).
113. C. M. Drain *et al.*, Dynamic photophysical properties of conformationally distorted nickel porphyrins .1. Nickel(II) dodecaphenylporphyrin. *The Journal of Physical Chemistry* **100**, 11984-11993 (1996).
114. X. Zhang *et al.*, Ultrafast Stimulated Emission and Structural Dynamics in Nickel Porphyrins. *The Journal of Physical Chemistry A* **111**, 11736-11742 (2007).
115. H. Tamiaki, S. Machida, K. Mizutani, Modification of 3-Substituents in (Bacterio)Chlorophyll Derivatives to Prepare 3-Ethylated, Methylated, and Unsubstituted (Nickel) Porphyrins and Their Optical Properties. *The Journal of Organic Chemistry* **77**, 4751-4758 (2012).
116. M. Gouterman, Spectra of porphyrins. *J. Mol. Spectrosc.* **6**, 138-163 (1961).
117. L. Serrano-Andrés, M. Merchán, M. Rubio, B. O. Roos, Interpretation of the electronic absorption spectrum of free base porphyrin by using multiconfigurational second-order perturbation theory. *Chem. Phys. Lett.* **295**, 195-203 (1998).



118. M. Rubio, B. O. Roos, L. Serrano-Andrés, M. Merchán, Theoretical study of the electronic spectrum of magnesium-porphyrin. *The Journal of Chemical Physics* **110**, 7202-7209 (1999).
119. C. Adamo, D. Jacquemin, The calculations of excited-state properties with Time-Dependent Density Functional Theory. *Chemical Society Reviews* **42**, 845-856 (2013).
120. W. Beenken *et al.*, Molecular Structures and Absorption Spectra Assignment of Corrole NH Tautomers. *The Journal of Physical Chemistry A* **118**, 862-871 (2014).
121. G. Ricciardi, A. V. Soldatova, A. Rosa, On the photophysics of metallophthalocyanine-based photothermal sensitizers: Synergism between theory and experiment. *J. Inorg. Biochem.* **102**, 406-413 (2008).
122. S. Patchkovskii, P. M. Kozłowski, M. Z. Zgierski, Theoretical analysis of singlet and triplet excited states of nickel porphyrins. *The Journal of Chemical Physics* **121**, 1317-1324 (2004).
123. D. M. Gampe *et al.*, Stable and Easily Accessible Functional Dyes: Dihydropentaazaanthracenes as Versatile Precursors for Higher Acenes. *Chemistry – A European Journal* **21**, 7571-7581 (2015).
124. L. X. Chen *et al.*, X-ray snapshots for metalloporphyrin axial ligation. *Chemical Science* **1**, 642-650 (2010).
125. R. E. Haddad *et al.*, Origin of the red shifts in the optical absorption bands of nonplanar tetraalkylporphyrins. *J. Am. Chem. Soc.* **125**, 1253-1268 (2003).
126. C. D. Tait, D. Holten, M. Barley, D. Dolphin, B. R. James, Picosecond studies of ruthenium(II) and ruthenium(III) porphyrin photophysics. *Journal of the American Chemical Society* **107**, 1930-1934 (1985).
127. D. Dolphin, R. H. Felton, Biochemical significance of porphyrin .pi. cation radicals. *Accounts of Chemical Research* **7**, 26-32 (1974).
128. J. Verne-Mismer, R. Ocampo, C. Bauder, H. J. Callot, P. Albrecht, Structural comparison of nickel, vanadyl, copper, and free base porphyrins from Oulad Abdoun oil shale (Maastrichtian, Morocco). *Energy & Fuels* **4**, 639-643 (1990).
129. F. W. Bobrowicz, W. A. Goddard, in *Methods of Electronic Structure Theory*, H. F. Schaefer, Ed. (Springer US, Boston, MA, 1977), pp. 79-127.
130. H. Paulsen, V. Schunemann, J. A. Wolny, Progress in Electronic Structure Calculations on Spin-Crossover Complexes. *Eur. J. Inorg. Chem.*, 628-641 (2013).
131. E. Rossi, G. L. Bendazzoli, S. Evangelisti, D. Maynau, A full-configuration benchmark for the N<sub>2</sub> molecule. *Chem. Phys. Lett.* **310**, 530-536 (1999).
132. W. Koch, M. C. Holthausen, *A Chemist's Guide to Density Functional Theory*. (Wiley-VCH Verlag GmbH, 2001), pp. 293.
133. I. Shavitt, in *Methods of Electronic Structure Theory*, H. F. Schaefer, Ed. (Springer US, Boston, MA, 1977), pp. 189-275.
134. A. C. Wahl, G. Das, in *Methods of Electronic Structure Theory*, H. F. Schaefer, Ed. (Springer US, Boston, MA, 1977), pp. 51-78.
135. B. O. Roos, P. R. Taylor, P. E. M. Siembahn, A complete active space SCF method (CASSCF) using a density matrix formulated super-CI approach. *Chem. Phys.* **48**, 157-173 (1980).
136. P. A. Malmqvist, A. Rendell, B. O. Roos, The restricted active space self-consistent-field method, implemented with a split graph unitary group approach. *The Journal of Physical Chemistry* **94**, 5477-5482 (1990).
137. P. Hohenberg, W. Kohn, Inhomogeneous electron gas. *Physical Review B* **136**, B864-B871 (1964).
138. M. E. Casida, in *Recent Advances in Density Functional Methods*. (WORLD SCIENTIFIC, 1995), vol. Volume 1, pp. 155-192.

139. A. Dreuw, M. Head-Gordon, Single-reference ab initio methods for the calculation of excited states of large molecules. *Chemical Reviews* **105**, 4009-4037 (2005).
140. K. Burke, J. Werschnik, E. K. U. Gross, Time-dependent density functional theory: Past, present, and future. *The Journal of Chemical Physics* **123**, 062206 (2005).
141. H. Goldstein, C. P. Poole, J. L. Safko, *Classical Mechanics*. (Addison Wesley, 2002).
142. A. T. B. Gilbert, N. A. Besley, P. M. W. Gill, Self-Consistent Field Calculations of Excited States Using the Maximum Overlap Method (MOM). *The Journal of Physical Chemistry A* **112**, 13164-13171 (2008).

## List of Figures

- Figure 1: Exemplaric depiction of the decoherence problem. The first column shows the correct quantum mechanical behavior of the wave packet: a) at the first coupling time  $t_{c1}$ , population is transferred from wave packet 1 on PES 1 to wave packet 2 on PES 2. b) With time evolving, wave packet 2 hits a barrier and is reflected, while wave packet 1 is accelerated downhill on PES 1. c) The second population transfer occurs at  $t_{c2}$  when wave packet 2 revisits the coupling region. The second column depicts the errors that can occur in FSSH exemplarily for one trajectory of the swarm. (Opaque dots mark the electronic state, which drives the dynamics; translucent dots depict how other electronic states are taken into account.): d) at the first hopping time  $t_{h1}$ , a hop of trajectory 1 on PES 1 to PES 2 occurs. e) With time evolving, the trajectory hits a barrier and is reflected. The product of the complex coefficients  $C_j^r(\tau)C_i^{r*}(\tau)$  (gray line), which influences the hopping probability does not decrease accordingly. f) Thus, the second hop can occur too early,  $t_{h2} < t_{c2}$ . ..... 11
- Figure 2: Calculated and experimental absorption spectra of the azaacene shown in the inset. The black dashed line represents the theoretical spectrum, calculated with B3LYP and Ahlrich's double zeta basis set(65) with polarization functions. The theoretical spectrum has been shifted by 0.42 eV and broadened by a Gaussian function with full width half maximum (FWHM) of 0.5 eV to better fit the experiment, as is customary. The experimental spectrum (gray line) was measured in toluene with a concentration of 32  $\mu\text{mol/l}$ . ..... 14
- Figure 3: Population change according to AIMS and SH calculations for the azaacene in red and blue, respectively. The data is averaged over 20 initial conditions. AIMS data contains also contributions of  $S_3$  and  $S_4$ . Orange and green lines show the exponential fit of the population for AIMS and SH, respectively. Underlying TDDFT calculations were done with B3LYP and Ahlrichs double zeta basis set with polarization functions. Inset: Change of the number of TBFs for the AIMS dynamics averaged over all 20 initial conditions. .... 16
- Figure 4: a) Normalized absorption spectra of  $\text{Fe}(\text{CO})_5$  calculated with different TDDFT functionals and experimental spectrum(97, 98) in gray. All calculation were computed using effective core potentials(99) and the associated basis set lanl2dz(100, 101) The

stick spectra were broadened with a Gaussian function with a FWHM of 0.7 eV and their maxima were shifted to 6.3 eV to maximally overlap with the main experimental absorption peak. The stick spectrum for  $\omega$ PBE is shown exemplarily. All spectra were calculated based on a geometry optimized with B3LYP. Inset shows the molecular structure of  $\text{Fe}(\text{CO})_5$ . b) Enlargement of the low-energy shoulder around 5.1 eV. The blue line shows literature CASSCF(96) calculations broadened with a Gaussian function with a FWHM of 0.7 eV. The orange line shows the  $\omega$ PBE results for the first 20 excited singlet states, which are obtained based on 150 configurations sampled from a Wigner distribution. The contributions of each of the individual states are shown as thin brown lines. Individual sticks for each configuration were broadened by 0.25 eV before summation and shifted by 0.5 eV. The light brown rectangles mark the energy regions from which the initial conditions are selected. ....24

Figure 5: a) Population change of the seven energetically lowest singlet excited states during the AIMS-dynamics averaged over all trajectory basis functions. b) Time evolution of the dissociating Fe-C bond length during the dynamics including seven excited states for all 15 SSAIMS runs and their average (thick black line). Light gray and dark gray lines are the SSAIMS runs, which ended in the dissociation of an axial and an equatorial carbonyl, respectively. The orange line marks the dissociation bond-length of 2.3 Å. The average (thick black line) reaches the dissociating bond-length at 157 fs.....26

Figure 6: Left: Optimized  $S_0$ -structure of  $\text{Fe}(\text{CO})_4$  as calculated with  $\omega$ PBE/lanl2dz,  $\omega=0.35 \text{ a.u.}^{-1}$ . Experimental values(92) are given in parenthesis, which agree perfectly with the shown computed structures. Middle:  $\text{Fe}(\text{CO})_5$  structure at the end of one SSAIMS/TDDFT run (after 392 fs) with the bond angles corresponding to the  $\text{Fe}(\text{CO})_4$  structure. Right:  $\text{Fe}(\text{CO})_5$  structure at the beginning of one SSAIMS/TDDFT run with the bond angles corresponding to the  $\text{Fe}(\text{CO})_4$  structure.....27

Figure 7: Population changes of singlet excited states a)  $S_{16}$  to  $S_{19}$  during the first 35 fs and b)  $S_1$  to  $S_3$  during the first 400 fs of the SSAIMS-dynamics averaged over all TBFs. The sum of the populations of the states, which are shown, is also given. For a), the sum was fitted with an exponential function:  $y=e^{-(t-t_0)/\tau}$ . Fit parameters are:  $t_0=1.5 \text{ fs}$ ,  $\tau=9.6 \text{ fs}$ .....28

Figure 8: Time evolution of the dissociating Fe-C bond lengths during the dynamics including 20 excited states for all eight SSAIMS runs and their average (thick black line). Light gray and dark gray lines are the SSAIMS runs, which ended in the dissociation of an

axial and an equatorial carbonyl ligand, respectively. The orange line marks the dissociation bond length of 2.3 Å. The average (thick black line) reaches the dissociating bond-length at 223 fs.....29

Figure 9: Comparison of the PES of the excited states of  $\text{Fe}(\text{CO})_5$  for a) CASPT2 and b) TDDFT for interpolated geometries between the start and end geometries of one SSAIMS/TDDFT run. The interpolation was done in internal coordinates and for a run that ended in the dissociation of an axial carbonyl, as visualized by the insets in a), which show the start and end geometry of PES. On the x-axis, the change in the coordinative bond length of the Fe to the dissociating carbonyl ligand is marked even though the other internal coordinates are also changing. CASPT2 calculations included eight states. For the TDDFT calculation, the twenty lowest lying excited singlet states and the ground state are shown. The radius of the filled circles along the curves scales with the oscillator strength of the respective excited state. For the ground state, filled circles have been added to highlight the raster of computations along the PES. TDDFT curves were calculated with TeraChem. CASPT2 curves were calculated with Molcas version 8.0. Groups of states with similar behavior are highlighted with colored background. MC states with decreasing and increasing energy are shown in orange and blue, respectively. Double excited states are highlighted in purple.....31

Figure 10: Comparison of the PES of the excited states of  $\text{Fe}(\text{CO})_5$  for a) CASPT2 and b) TDDFT for interpolated geometries between the start and end geometries of one SSAIMS/TDDFT run. The interpolation was done in internal coordinates and for a run that ended in the dissociation of an equatorial carbonyl ligand, as visualized by the insets in a), which show the start and end geometry of PES. On the x-axis, the change in the coordinative bond length of the Fe to the dissociating carbonyl ligand is marked even though the other internal coordinates are also changing. CASPT2 calculations included eight states. For the TDDFT calculation, the twenty lowest lying excited singlet states and the ground state are shown. The radius of the filled circles along the curves scales with the oscillator strength of the respective state. For the ground state, filled circles have been added to highlight the raster of computations along the PES. TDDFT curves were calculated with TeraChem. CASPT2 curves were calculated with Molcas version 8.0. Groups of states with similar behavior are highlighted with colored background. MC

states with decreasing and increasing energy are shown in orange and blue, respectively. Double excited states are highlighted in purple.....	32
Figure 11: Left: HOMO-1, HOMO, LUMO and LUMO+1 of NiTMP calculated with $\omega$ PBE, $\omega=0.2 \text{ a}_B^{-1}$ plotted with an isovalue of $0.02 \text{ electrons}/\text{\AA}^3$ . These orbitals correspond to the Gouterman orbitals. Right: Experimental(124) and calculated absorption spectra of NiTMP for different conformers. Q-band region of calculated spectra is enlarged by a factor of 40. All calculations were computed using ECPs(99) and the associated basis set lanl2dz(100, 101) and the $\omega$ PBE density functional employing an $\omega$ of $0.2 \text{ a}_B^{-1}$ .....	36
Figure 12: Charge difference densities of NiTMP transitions. Orange and blue regions mark electron depletions and accumulation, respectively. Isovalue: $2.0 \cdot 10^{-5} \text{ electrons}/\text{\AA}^3$ .....	37
Figure 13: Electronic energies (reference is the ground state of the planar conformer) of the seven lowest lying excited singlet states at the critical points of the potential energy surface (PES) of NiTMP. Dotted lines connect the energies of the states between different critical points. The ground state conformers are marked with arrows symbolizing the excitation into the LC states. Energetic minima (Min) of the excited states are highlighted by a broadened line for the respective state, whereas minimum energy conical intersections (MECI) are enclosed in black rectangles. Thick dot-dashed lines mark possible pathways. Dashed lines mark a break in the PES due to a new conformer. Critical points of interest for a pathway starting from the planar (ruffled) [both] conformer[s] have a red (blue) [purple] background.....	39
Figure 14: a) Population change of the singlet states during the dynamics averaged over 20 SSAIMS runs and a fit of the population decay. This includes the following grouping based on the ordering at the ground state conformer: $S_6$ and $S_7$ were grouped to $LC_{1,2}$ states and the $S_3$ and $S_4$ states are grouped as $MC_{2,3}$ states. b) Population change of states characterized based on energetic considerations as detailed in the main text. ....	42
Figure 15: The decay mechanism is visualized including the lifetimes, as obtained by the non-sequential fit including the $MC_1$ population. ....	44
Figure 16: Comparison of the population change of the higher excited states for the dynamics starting from the ruffled and planar conformer. These have been averaged over 20 and 5 SSAIMS runs for the planar and ruffled conformer, respectively. Here the	

population changes of the states $S_4$ , $S_5$ and $S_6$ are displayed, as well as the changes for the $LC_{1,2}$ , $LMCT_2$ and $MC_{2,3}$ states in correspondence to Figure 14 b). .....	45
Figure 17: Calculated XANES spectra for the $1s \rightarrow 4p_z$ energy region of the singlet states of interest. The spectra were calculated using Ahlrich's all-electron double zeta basis set(65) with polarization functions and were shifted by 67.2 eV in order to fit the experiment. The peak positions of the LMCT state were taken the literature.(12) .....	47
Figure 18: Experimental(115) and calculated absorption spectra of Ni-DEPE. Theoretical stick spectra are broadened with a Gaussian function with a width of 0.2 and shifted by 0.42 eV. ....	49
Figure 19: Electronic energies (reference is the ground-state of the planar conformer) of the six (nine) lowest lying excited singlet states at the energetic minima of the excited states (ground state) of NiDEPE. Dotted lines connect the energies of the states between different stationary points. The ground state minimum is marked with an arrow symbolizing the excitation into the $LC_1$ state. Energetic minima (Min) of the excited states are highlighted by a broadened line for the respective state.....	50
Figure 20: Population change of the first five singlet states, which include the first LC state, the $LMCT_2$ state and the MC states during the dynamics averaged over 20 AIMS runs and a fit of the population decay. $S_4$ and $S_5$ have been combined to LC (+MC) and $S_2$ and $S_3$ have been combined to the $MC_1$ ( $d_{z^2} \rightarrow d_{x^2-y^2}$ ). Decay time for the combined $S_4$ , $S_5$ and $S_6$ is 207 fs and for $S_2$ and $S_3$ it is 506 fs. The inset shows the molecule NiDEPE. ....	51
Figure 21: Change of the oscillator strength of the state with the highest population during the first 25 fs of the dynamics averaged over all runs. Inset shows an image of the whole dynamics. The fit formula and the parameters are given in the inset. ....	52
Figure 22: Population change of all 19 singlet excited states during the first a) 400 and b) 35 fs of the SSAIMS-dynamics averaged over all TBFs. ....	72
Figure 23: Population change of singlet excited states a) $S_{13}$ to $S_{15}$ and b) $S_{10}$ to $S_{12}$ during the first 400 fs of the SSAIMS-dynamics averaged over all TBFs.....	72
Figure 24: Population change of singlet excited states a) $S_7$ to $S_9$ and b) $S_4$ to $S_6$ during the first 400 fs of the SSAIMS-dynamics averaged over all TBFs.....	72

## List of Tables

Table 1: Lifetimes $\tau$ as obtained by a fit of the nonadiabatic dynamics results for AIMS and FSSH and the average number of nonadiabatic events, number of spawns and hops for AIMS and FSSH, respectively. The underlying TDDFT calculations were done with the same parameters as given in the caption of Figure 2.....	15
Table 2: Comparison of the accuracy and computational cost of different ESMs. ....	20
Table 3: Electronic excitations for the planar NiTMP conformer. ....	36
Table 4: Optimized geometric parameters ( $\text{\AA}$ and deg) for the three ground state conformers, the excited states of interest and minimum energy conical intersections (MECI).....	38
Table 5: Fit of the population of states including or not including the $MC_1$ state. ....	43
Table 6: Electronic excitations at the Franck-Condon point.....	49

## List of Abbreviations

### *General Abbreviations*

AIMS	<i>Ab-initio</i> multiple spawning
CAS	Complete active space
CCSD	Coupled-cluster singles-and-doubles
CI	Conical intersection
CISD	Configuration interaction singles and doubles
DFT	Density functional theory
DSSC	Dye sensitized solar cell
ESM	Electronic structure method
FMS	Full multiple spawning
FSSH	Fewest switches surface hopping
Full CI	Full configuration interaction
FWHM	Full width half maximum



HF	Hartree-Fock approximation
HOMO	Highest occupied molecular orbital
IFG	Independent first generation approximation
LDA	Local density approximation
LC	Ligand-centered
LMCT	Ligand-to-metal charge-transfer
LUMO	Lowest unoccupied molecular orbital
GAS	Generalized active space
GGA	Generalized gradient approximation
GPU	Graphics processing units
MC	Metal-centered
MCSCF	Multi-configuration self-consistent field
MCTDH	Multi-configurational time-dependent Hartree
MLCT	Metal-to-ligand charge-transfer
NACME	Nonadiabatic coupling matrix elements
NiDEPE	Nickel-methyl-3-devinyl-pyropheophorbide-a
NiTMP	Nickel-tetramesityl-porphyrin
NiTPP	Nickel-tetraphenyl-porphyrin
PES	Potential energy surface
PT2	Perturbation theory second order
RAS	Restricted active space
SA	state-averaged
SCF	Self-consistent field
SE	Schrödinger equation
SH	Surface hopping
SS	Stochastic selection
TBF	Trajectory basis function
TD	Time-dependent

**Formula symbols**

$\alpha$	Width of Gaussian basis function
$\bar{\gamma}$	Time-dependent phase of Gaussian basis function
$\varepsilon_i$	Electronic energies
$v_{xc}[\rho]$	Exchange-correlation potential
$\xi$	Density-density response function
$\rho_0$	One particle probability density of the ground state
$\Phi_{HF}$	Hartree-Fock wave function
$\varphi_i$	Electronic wave function of the noninteracting system/One-electron wave functions
$\phi_i$	Electronic wave function
$\Psi$	Molecular wave function
$\Xi_j^I$	Multidimensional Gaussian basis functions with frozen width
$\chi_i$	Nuclear wave function
$\Omega$	Matrix of Casida equations
$\omega_{kl}$	Electronic excitation energies
$\hat{H}$	Hamiltonian operator
$\hat{H}_{el}$	Electronic Hamiltonian operator
$\hat{T}_i$	Excitation operator
$\hat{T}_{nuc}$	Kinetic energy operator of the nuclei
$\hat{T}_{el}$	Kinetic energy operator of the nuclei
$\hat{V}_{nuc-el}$	Nuclear-electronic attraction operator
$\hat{V}_{nuc-nuc}$	Nuclear-nuclear repulsion operator
$\hat{V}_{el-el}$	Electronic-electronic repulsion operator
$A$	Configuration interaction expansion coefficients of MCSCF

---

$B$	Wave function expansion coefficients
$b_i$	occupation number
$C$	Complex amplitudes
$c$	coefficients of the configuration interaction expansion
$\mathbf{D}_{ij}$	First order nonadiabatic coupling
$d_{ij}^\alpha$	Nonadiabatic coupling matrix elements (NACME)
$\mathbf{F}_{kl}$	Eigenvectors of Casida Equations
$G_{ij}$	Second order nonadiabatic coupling
$h$	Hopping probability
$\hbar$	reduced Planck's constant
$K_{ij,kl}$	Casida coupling matrix
$M_\alpha$	Mass of the $\alpha^{th}$ nuclei
$m_e$	Mass of one electron
$N$	Number of nuclei
$n$	Number of electrons
$\overline{\mathbf{P}}_j^I$	Momenta of Gaussian basis function
$q_e$	Elementary charge
$\mathbf{R}_\alpha$	Coordinates of the $\alpha^{th}$ nuclei
$\overline{\mathbf{R}}_j^I$	Position of Gaussian basis function
$\mathbf{r}_i$	Coordinates of the $i^{th}$ electron
$\mathbf{S}_{II}$	Overlap matrix
$\dot{\mathbf{S}}_{II}$	Time derivative of the overlap matrix
$Z_\alpha$	Charge of the $\alpha^{th}$ nuclei



## **Selbstständigkeitserklärung**

Ich erkläre, dass ich die vorliegende Arbeit selbständig und unter Verwendung der angegebenen Hilfsmittel, persönlichen Mitteilungen und Quellen angefertigt habe.

Jena, 29. Juni 2018

Julia Preiß